2020

Reaction profiling of extracellular protein phosphorylation through a microfluidic reactor coupled with Raman Spectroscopy

Abigail Casey
Virginia Commonwealth University

Reaction profiling of extracellular protein phosphorylation through a microfluidic reactor
coupled with Raman Spectroscopy

A Dissertation
Presented to
The Academic Faculty

By
Abigail Hyacinth Marie Casey

In Partial Fulfillment
Of the Requirements for the Degree
Doctor of Philosophy in the
Department of Chemical and Life Science Engineering

Virginia Commonwealth University
May 2020

Table of Contents

Table of Tables

Table of Figures

Abstract

Diseases and disorders in the human body are considered abnormalities of proper cellular function. Understanding the signal transduction mechanisms that cause these abnormalities is crucial to developing earlier detection methods, better treatment options and effective cures. While current diagnostic procedures are powerful tools in diagnosing diseases, they are ineffective in informing physicians on the real-time behavior of the signal transduction mechanisms associated with diseases and disorders. Currently, disease progression is monitored over time through routine patient visits and testing by one or more of the above techniques. By developing an approach that can monitor structural and conformational changes of proteins during biochemical reactions we can provide insight towards signal transduction mechanisms. This study successfully monitored the phosphorylation of Casein through catalysis of PKA and phosphate donation from adenosine triphosphate (ATP) in a 3D printed microfluidic device that was integrated with confocal Raman spectroscopy. The development of an adaptive PCA algorithm identified variance between the PO_x vibrational modes at 1090 cm^{-1}, 1329 cm^{-1}, 1411 cm^{-1}, 1506 cm^{-1} and 1558 cm^{-1} present in ATP. The protein phosphorylation reaction was monitored in real-time by detecting the change of the PO_x vibrational mode at 1556 cm^{-1} that appears in ATP during the reaction progression. This research also enables future use on numerous other biochemical reactions utilizing Raman spectroscopy. Additionally, this work enables translation of this research to analyze biochemical reactions intracellularly.

Acknowledgements

I would like to thank my fiancé, Bryon, for all the motivation and patience over the past 6 years while pursuing my graduate studies. I would like to thank my research advisor, Dr. Gregory Triplett, for the opportunity to pursue this research. I would also like to acknowledge my dissertation committee members for their support, guidance, and mentorship. I would like to thank all the undergraduate students, support staff, and fellow group members that I have had the pleasure of working with. This work would not have come to realization without all of you. Lastly, I would like to thank my friends and family who have supported me through my studies over the years.

Chapter 1: Problem Statement

1.1 Health and Disease in the Body

Diseases and disorders in the human body are considered abnormalities of proper cellular function [1]. In order to treat diseases and disorders, researchers must fully understand what causes them and the mechanisms by which they attack the body. Understanding the signal transduction mechanisms that cause these abnormalities is crucial to developing earlier detection methods, better treatment options and effective cures. Diseases fall under a number of different categories: infectious diseases, degenerative diseases, nutritional disorders, metabolic disorders, immune disorders, neoplasm (new growth), and psychiatric disorders. These categories encompass abnormal processes that occur such as microorganisms infecting the host body, the breakdown of tissue systems, dietary lack or excess of substances, deficiencies processing substances, deficiencies related to the immune system, unwarranted cell growth, or disorders in the cognitive function of the brain or nervous system. The common thread between each of these processes is that they occur at the cellular level of the body. Cells are the fundamental unit of all things living, meaning they are the simplest structures that exhibit independent signs on life. Various types of cells make up every tissue system in the human body. These systems are controlled by biochemical reactions occurring either within the cells or from cell to cell. This is referred to as signal transduction or cellular communication. Studies have linked irregularities in these highly regulated mechanisms to diseases such as cardiovascular disease [2], cancer [3], Alzheimer's [4], and diabetes [5]. Cardiovascular disease was the leading cause of death in the United States in 2017 accounting for 24.1% of deaths and cancer was the second leading cause accounting for 22.7% of deaths [6].

1.2 Signal Transduction Mechanisms

Signal transduction is the process by which cells communicate through molecular signaling. Multicellular organisms regulate cellular functions by communicating through molecular signals. There are three steps to cellular communication described in figure 1. It begins with the cell membrane receiving a signal from the outside environment, which activates a transfer of a molecular signal. The majority of these transfers occur between proteins. When a protein receives a new signal, the cell responds by performing a specific function or passing this information to the next cell by sending a signal and restarting the signal transduction process.
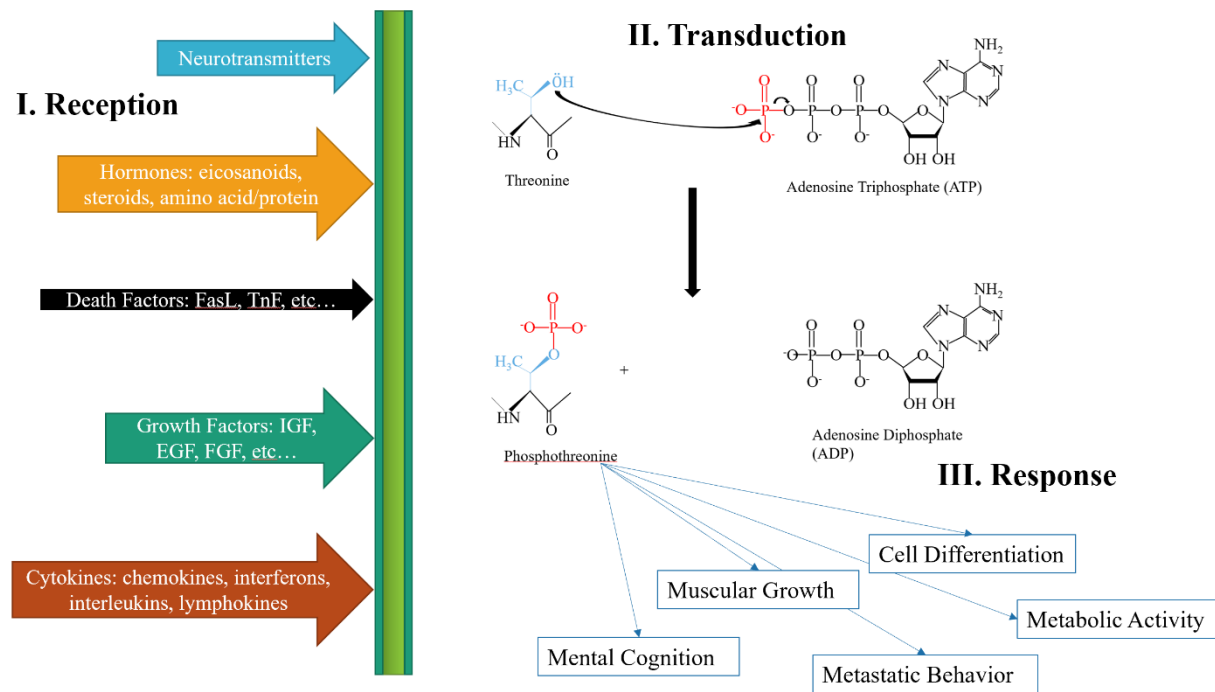
Figure 1 – Cellular communication pathway: Reception, Transduction, Response

1.2.1 Cellular Reception

Reception can occur through direct cell contact or by the release of molecules that bind to receptors on the outside of cells or pass through the membrane of the cell. This triggers a response

within the cell associated with enzymatic activity. This enzymatic activity is referred to as the transduction phase of the process involving proteins. Proteins are fundamentally polymeric chains of amino acids. There are 22 proteinogenic amino acids present in eukaryotic and prokaryotic cells, each defined by their functional group. Twenty of these amino acids are directly encoded into the deoxyribonucleic acid and ribonucleic acid sequences in genetic code. Nine of these amino acids are referred to as 'essential amino acids' due to the bodies inability to synthesize them [7]; therefore, these essential amino acids must be obtained through diet. The functional groups of amino acids within proteins are the active sites or domains for biochemical processes of post translation modifications.

1.2.2 Cellular Transduction

Post translation modifications (PTM) of proteins are responsible for cellular functions such as cell growth, muscular growth, metabolic activity, mental cognition, and cell differentiation. Protein regulation may be organized by distinguishing the enzymatic role of an individual protein into three categories: readers, writers and erasers. Many proteins act as catalyst in PTMs and add a molecular message to an active domain of another protein acting as 'writers' and are known as kinases and transferases. Eraser proteins remove these molecular messages and are known as phosphatases and deacetylases. Proteins that 'read', do so by recognizing the changes made by writers and erasers, initiating a sequential event to another protein or to another domain on the same protein. The targets of readers, writers and erasers are generally short amino acid chains within a protein and are referred to as motifs. PTMs of proteins are highly regulated to the extent that only specific kinases can catalyze an event to a specific substrate protein, and the reversible process can only be achieved by a specific phosphorylase. Furthermore, kinases and

phosphorylases may only write and erase after being activated themselves, which may involve preliminary writing or erasing or may only be achieved when specific molecules are present in the cell. For example, protein kinase C (PKC) can only catalyze a substrate protein when it has been activated by receiving a molecular message in three different domains [8]. Once PKC is activated, it may then serve as a catalyst for further phosphorylation events on substrate proteins in the cell. Protein Kinase A is another example where it is only activated in the presence of adenosine 3′,5′-cyclic monophosphate (cAMP) and may then phosphorylate a number of different substrate proteins. Previous studies have reported PKA activity and dependent processes are linked to such diseases and Huntington's disease [9], Tau-driven cognitive dysfunction [10], and Parkinson's disease [11]. The diagnosis of these diseases to isolate the responsible signal transduction mechanism is critical.

1.2.3 Cellular Response

The final step in signal transduction is the cell's response to the post translational modification that occurred in the previous step. This response, may be the cell performing a specific function or pass the molecular signal on to a neighboring cell. Cells can perform numerous functions including gene activation, metabolic activity, differentiation, muscular growth, and mental cognition.

1.3 Current Medical Diagnostic Procedures

Once a disease is suspected, an individual may seek diagnosis from a physician. Current diagnostic procedures start with patient reported symptoms and visible signs of symptoms. The physician may then order radiology or imaging as well as lab tests to be performed in order to fully diagnosis the disease. Examples for clinical diagnostic procedures are illustrated in figure 2.

a. CT Scan
-Emission of X-rays
~0.5-1mm

b. MRI
-Strong magnetic fields
~1-2mm

c. Ultrasound
-Strong magnetic fields
~0.5mm @ 3Hz
~0.3mm @ 5Hz

d. Labwork
-must be done on
extracted samples
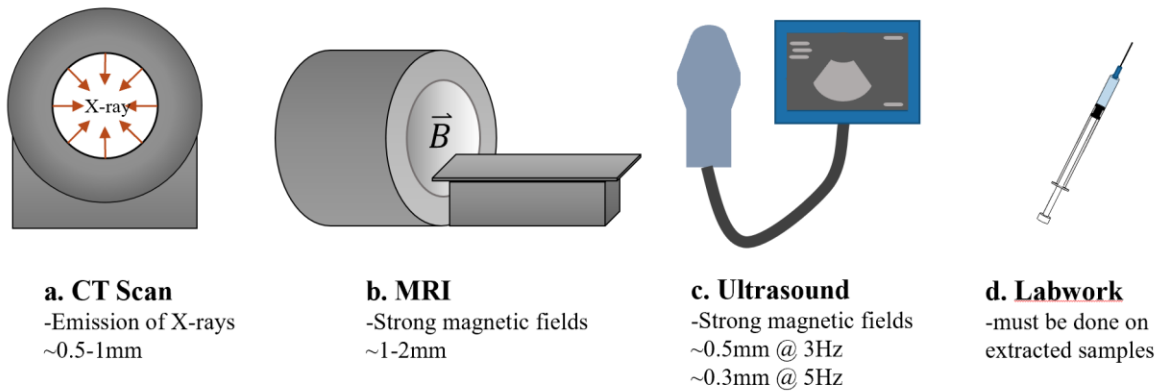
Figure 2 – Clinical diagnostic procedures

1.3.1 Patient laboratory testing

Labwork relies on extraction of samples from a patient and subsequent analysis that may involve microscopic/macroscopic examination, automated analyzers (i.e. mass spectrometer), molecular diagnostics (i.e. immunoassays) or cultures. These techniques rely heavily on chemistry, microbiology, hematology and molecular pathology. Samples may include urine, blood, saliva, feces, sputum or the biopsy of tissue. Clinical laboratory diagnosis is limited to the detectability of these techniques as well as the accessibility to the type of bodily fluid or sample needed [7].

1.3.2 Radiological methods

Current imaging methods may include ultrasounds, computerized tomography (CT) scan, magnetic resonance imaging (MRI) and positron emission tomography (PET). Ultrasounds send and receive sounds waves that can produce an image for therapeutic procedures and diagnosis. This method is effective for imaging soft tissue such as muscles, tendons, and fetuses in pregnant women. It is also widely used to guide interventional procedures such as biopsies, fluid drainage and anesthetic needle placement [12]. Ultrasounds are relativity inexpensive, and increasingly

accessibility to patients. However, drawbacks include difficulty imaging bone tissue, low resolution and limited depth penetration. A CT scan uses X-ray emission in line with a detector that rotates around the patient, commonly used to detect infarctions, hemorrhaging and bone trauma. While CT has several advantages over traditional 2D X-ray scans such as superimposition elimination [13] and higher resolution [14], it also poses a risk to patients by exposure to radiation [13]. It is estimated that current CT usage may be responsible for 1.5 – 2.0% of all cancers in the United States [13]. The typical radiation dose from a CT scan can be 100 to 1000 times greater than traditional 2D X-ray [14] making it unsuitable for pregnant patients and children. Full body CT scans are also inadvisable due to radiation exposure [15]. When a full body scan is necessary, radiologists turn to magnetic resonance imaging. MRI's produce magnetic fields that align the proton spins of the water molecules to produce images that can be analyzed for diagnosis. This method is the preferred method for the detection of abnormalities in the central nervous system including dementia, cerebrovascular disease, Alzheimer's and epilepsy as well as the detection of preoperative cancers. While MRI is considered a safe technique, it is generally more expensive, time-consuming and may cause claustrophobia in some patients [16]. Due to the operating conditions of an MRI, patients with implants, cardiac pacemakers, or shrapnel are ineligible to receive this type of imaging [16]. Positron emission tomography (PET) scan utilizes a radioactive tracking dye that may be inhaled, injected or swallowed by the patient. During the scan the radioactive dye emits positrons that combine with electrons to produce gamma rays. These gamma rays are detected by the instrument around the patient and used to produce a 3D image of the tracer concentrations within the body. One of the major disadvantages to this diagnostic procedure is the cost of operation [17] as well as the limitations of the availability and use of the radioisotopes used in the tracking dyes.

1.4 Challenges

While these techniques are powerful tools in diagnosing diseases, they are not effective in informing doctors and physicians on the real-time behavior of the signal transduction mechanisms associated with diseases and disorders. Currently, disease progression is monitored over time through routine patient visits and testing by one or more of the above techniques. Tumor growth may be monitored through an MRI image over the course of months [16]. Treatment efficacy may be monitored through labwork performed at the beginning, duration and end of treatment by comparing key biomarkers at each interval. Yet, there is no clinical technique that can monitor the reaction in real-time as it's occurring within a patient.

The purpose of this work is to profile reaction concentrations of extracellular protein phosphorylation both spatially and temporally. Our goal is to combine microfluidic reactor technology with confocal Raman spectroscopy to investigate biochemical reactions such as protein phosphorylation in real-time. Raman spectroscopy will provide accurate chemical "fingerprint" analysis of our reaction at different points along the reactor path. By developing an approach that can monitor structural and conformational changes of proteins during biochemical reactions we can provide insight towards signal transduction mechanisms. Protein phosphorylation is one of the most prevalent signal transduction mechanisms that occurs within cells. This research is crucial to the development of a diagnostic instrument that would be used clinically. A diagnostic instrument that can monitor disease related signal transduction mechanism in real-time in a patient would aid in prognosis and treatment efficacy. For example, Alzheimer's is reported to be related to the accumulation of abnormal tau and beta-amyloid proteins. If a diagnostic instrument was able to monitor the accumulation rate of these proteins, then a better prognosis of the patient's individual

decline would be possible, thus giving the patient and family a better timeframe. This type of diagnostic instrument could also monitor the accumulation rates during clinical trials of treatment options to determine efficacy of the treatments without waiting for lab results or long testing windows.

1.5 Outline for this dissertation

This dissertation focuses on monitoring a protein phosphorylation reaction in real-time by combining several reliable technologies: microfluidic reactors, Raman spectroscopy and principal component analysis. Chapter 2 summarizes the research to date on protein phosphorylation and associated detection methods, microfluidic reactor technology, Raman spectroscopy and the application of statistical methods applied to spectral data. Chapter 3 describes the analytical approached developed to extract salient features in branched chain amino acids. Chapter 4 describes the microfluidic reactor design, fabrication and preliminary solution results on the integration of the microfluidic reactor with Raman spectroscopy. The combination of the microfluidic reactor, with Raman spectroscopy and the adaptive principal component analysis to monitor a protein phosphorylation reaction is described in chapter 5. The summary and conclusions are discussed in Chapter 6 with the recommendations for future work in chapter 7.

Chapter 2: Background and Literature Review

This chapter describes the specific biochemical reaction, protein phosphorylation, by detailing the reaction steps of the kinase, ATP and substrate protein. A brief history of the discovery of protein phosphorylation and a detailed section on the current methods for detection of protein phosphorylation. This section will highlight each technique's method and drawbacks. The next section with describe microfluidic reactor technology and specific examples of microfluidic reactors applied to biochemical reactions. Background explanation on reactor design equations is included in this section, as these equations will be used in later chapters to determine reactor dimensions. Concluding the chapter is an introduction to Raman spectroscopy and the analytical technique that is applied to the spectral data.

2.1 Protein Phosphorylation

One of the most common molecular groups to be passed from protein to protein is a phosphate group. Signal transduction in which a protein receives a phosphate group is referred to as protein phosphorylation. Conversely, if a protein gives up its phosphate group, it is called protein dephosphorylation. Protein phosphorylation follows an enzymatic reaction mechanism, where the enzyme or kinase facilitates the transfer of the phosphate group from adenosine triphosphate (ATP) to the substrate protein. Literature has shown the reaction to progress as follows:

$$K + ATP \leftrightarrow K \cdot ATP \tag{1}$$

$$K \cdot ATP + P \leftrightarrow K \cdot ATP \cdot P \tag{2}$$

$$K \cdot ATP \cdot P \rightarrow K \cdot ADP \cdot PP \tag{3}$$

$$K \cdot ADP \cdot PP \rightarrow K \cdot ADP + PP \tag{4}$$

$$K \cdot ADP \leftrightarrow K + ADP \tag{5}$$

where K is the kinase, ATP is adenosine triphosphate, P is the protein substrate, ADP is adenosine diphosphate, and PP is the phosphorylated substrate protein. It is understood that the kinase first binds to the ATP in a hydroponic pocket through hydrogen bonds and van der Waals forces [18]. This binary complex then binds to the substrate protein forming a tertiary complex [7]. During this phase of the reaction, it is speculated that the kinase 'prepares' the substrate protein to receive the phosphate group and facilitates the transfer [19]. The 'preparation' involves the unfolding and folding of the substrate protein to reveal the target amino acid for the phosphate group [20]. Once the phosphate group has been transferred, illustrated in Figure 3, the substrate protein disassociates from the kinase and ADP binary complex goes on to perform a specific function within the cell. The kinase and ADP then disassociate from each other completing the reaction [7].
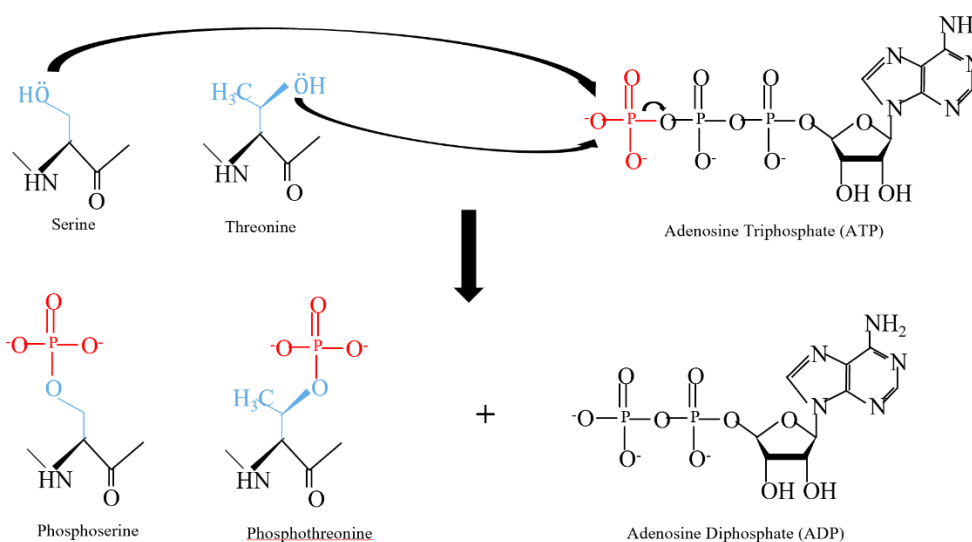
Figure 3 – Chemical reaction depiction of phosphate transfer from adenosine triphosphate during phosphorylation of L-serine and L-threonine.

The first phospho-group detected on a protein was reported in 1906 by P. A. Levene and C. L. Alsberg on vitellin. This report referred to the composition of vitellin having up to 10% phosphorus in the final precipitate [21]. Nearly 30 years later, Levene was able to identify the phospho-group was bonded to the serine residue in vitellinic acid. At this time Levene, et al were able to isolate

serinephosphoric acid, report its structure and determine that only one residue of serine was phosphorylated [22]. The function of the phosphor-group on the amino acid was still unknown. For the next several years, efforts were focused on determining other proteins that contained a phospho-group and the development of new methods for isolation and purification. One of the most influential purification methods was developed by Gerty and Carl Cori on phosphorylase enzyme from muscle tissue of rabbits [23] [24] [25]. These experiments detailed their purification of this early phosphorylase through extraction from rabbit subjects and were able to characterize the phosphorylase by its abundance in the extracted protein, molecular weight and diffusion coefficient [23]. Further purification work revealed that there was an active phosphorylase *a* and deactive phosphorylase *b* by measuring the difference when in the presence of adenylic acid [24]. While this work detailed that two forms of this phosphorylase existed, it did not explain how they differed or the mechanism by which it was activated or deactivated [25].

In 1955 Fischer and Krebs reported that the phosphorylase *b* form was more prevalent in resting muscle than the phosphorylase *a* form [26] and that two different enzymes catalyze the reaction between the two forms [27]. They were able to determine that one enzyme catalyzes the reaction from phosphorylase *b* to phosphorylase *a* and the other enzyme catalyzes the reverse reaction from *a* to *b* [19]. They also determined that this activation/deactivation cycle was influenced by the presence of Mg^{2+} and Ca^{2+} ions [20]. Up until this discovery by Fischer, the understanding of phosphorylated proteins was that they existed and could be isolated and purified, but their only function was for nutritional value in the feeding of mammalian young [28]. In further work, Fischer was able to determine that muscle contraction directly correlated with the phosphorylation of the inactive phosphorylase enzyme, and he determined that there was a cascade reaction of an enzyme activating an enzyme [28].

2.1.1 Protein phosphorylation detection methods

Current research enables the performance of intracellular and extracellular protein phosphorylation through the use of benchtop chemistry experiments paired with a number of different detection methods. Each experiment follows the same basic steps: sample collection and preparation, reaction, purification, enrichment, and characterization. Figure 4 displays a flow diagram of these processes. In the 1970's, several methods for electrophoresis were applied to protein purification [29] [30]. In the 1980's, early work to isolate and identify phosphorylated proteins from cells was done using isoelectric focusing. One technique used a liquid cooled system with a voltage gradient the electrophoretic chamber to separate the phosphorylated proteins from eight different species of fowl to compare the phosphorylation of each [31]. Another technique used a high-performance liquid chromatography (HPLC) column with an octadecylsilane column with a buffer gradient [32] to compare the phosphorylated state of proteins. Furthering this work, a technique for tagging the proteins in the electrophoresis membrane was developed by Towbin et al. [33]. This is now commonly known as Western Blot. First receiving this name from the work done by Burnette et al. [34], this enabled researchers to recover a greater amount of the protein products [35]. Sodium Dodecyl Sulfate (SDS) Polyacrylamide gel electrophoresis (PAGE) was applied to protein detection from 1-100 kDa in 1987 [36] and improved a year later by using Coomassie Blue as a tracking dye [37].
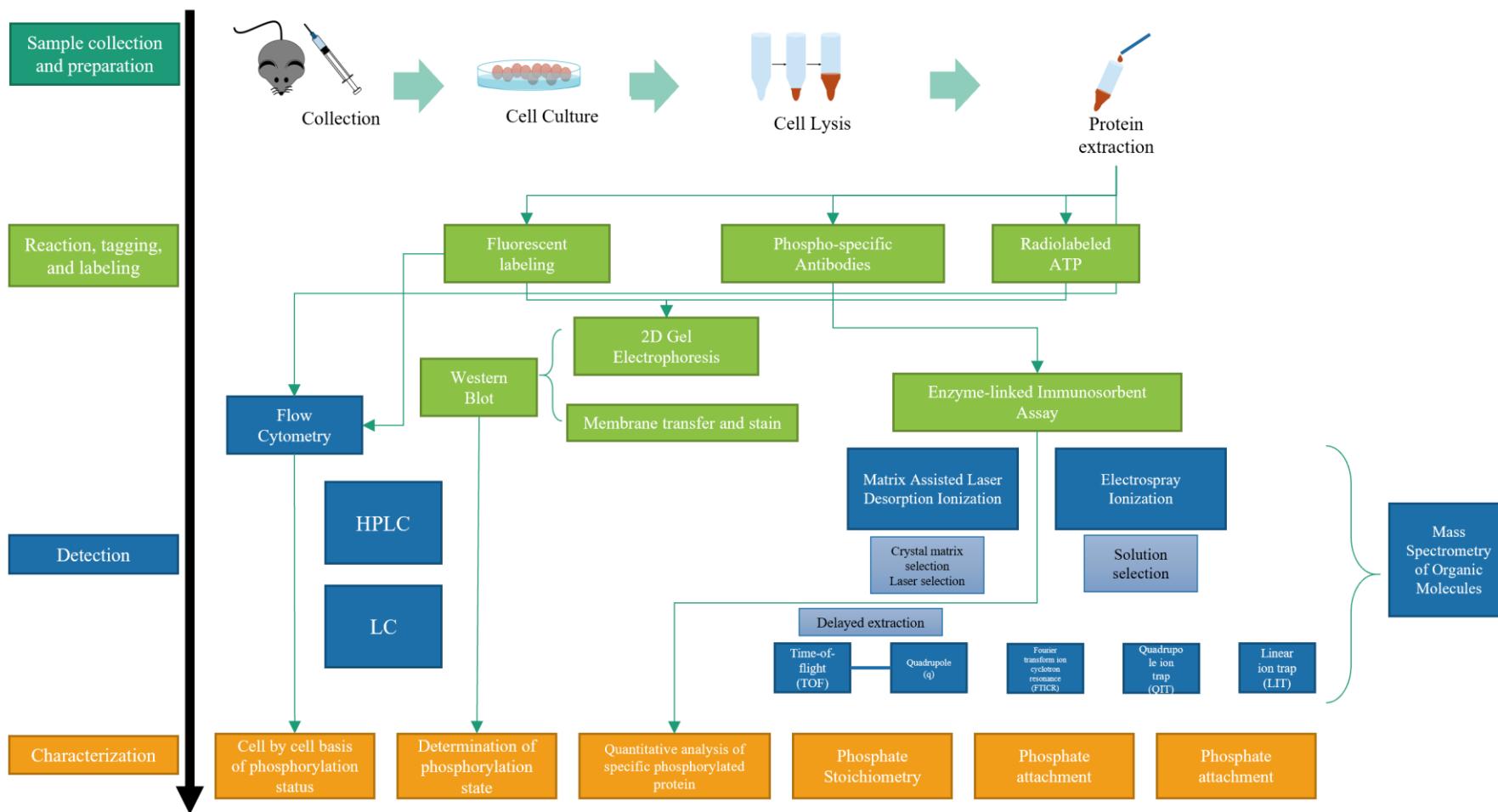
Figure 4 – Flow diagram of current protein phosphorylation procedures starting at sample prep through characterization techniques.

Protein phosphorylation research became highly investigated in the early 90s. Initial detection research at this time was done using radiolabeled ATP in the reaction [38] [39]. This resulted in the phosphorylated proteins being tagged by a radioactive ^{32}P enabling subsequent detection by two-dimensional gel electrophoresis or high-performance liquid chromatography [40]. These early traditional techniques required large amounts of phosphorylated proteins and radiolabel ATP for the detection methods to be reliable. The necessary dose of radiolabeled ATP for these experiments was high enough to be hazardous to the researchers [41], a major drawback to its use. These experiments enabled researchers to determine the site at where the radiolabeled phosphate group attaches, yet still resulted in relatively low yield of phosphorylated products [39].

Detection of organic molecules through mass spectrometry (MS) emerged in the 80s when the enabling technologies of electrospray ionization (ESI) [42] [43] and matrix-assisted laser desorption ionization (MALDI) [44] [45] [46] debuted. During ESI a solution of either positive or negative analyte is continuously sprayed from a charged needle illustrated in Figure 5. The plume from the needle is directed into the mass analyzer of the MS. During MALDI, sputtering of a solid sample by laser bombardment produces ions of the analyte that are sent to the mass analyzer of the MS illustrated in Figure 6. It wasn't until the 90s that MS was applied to protein phosphorylation research. One of the first works to identify enzymatic dephosphorylation of tyrosine peptides employed a micro capillary reactor coupled directly to an electrophoresis column and a liquid chromatography column independently then directly to an on-line ESI-MS [41]. The same research team concluded that MS coupled with this type of enzyme reactor is a viable approach for the determination of phosphorylation sites and suggested that kinase specific reactors needed to be developed to advance the field. Over the next 20 years several phosphospecific

antibodies and fluorescent labels were employed to enhance the detection and characterization of serine, threonine, and tyrosine phosphorylation events through ESI and MALDI MS.
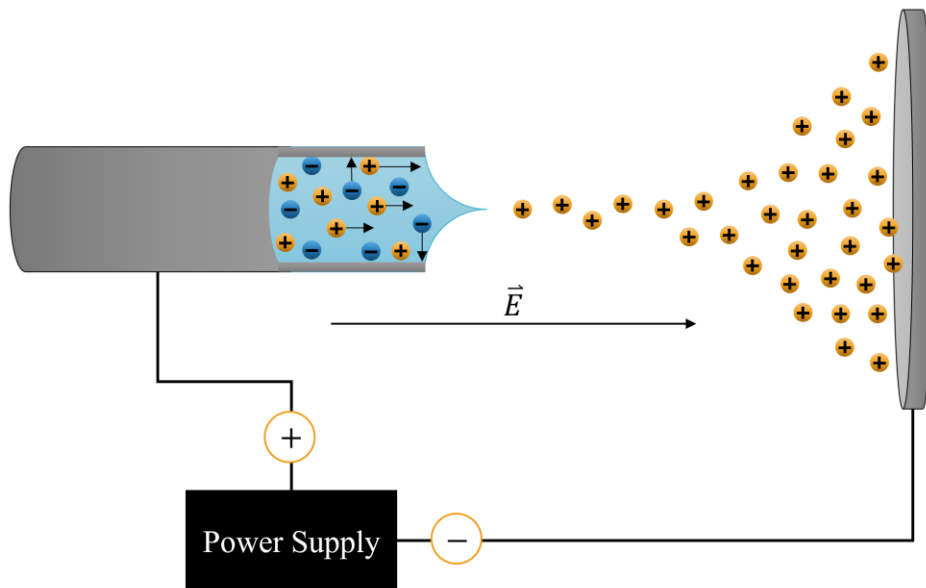
Figure 5 – Electrospray Ionization
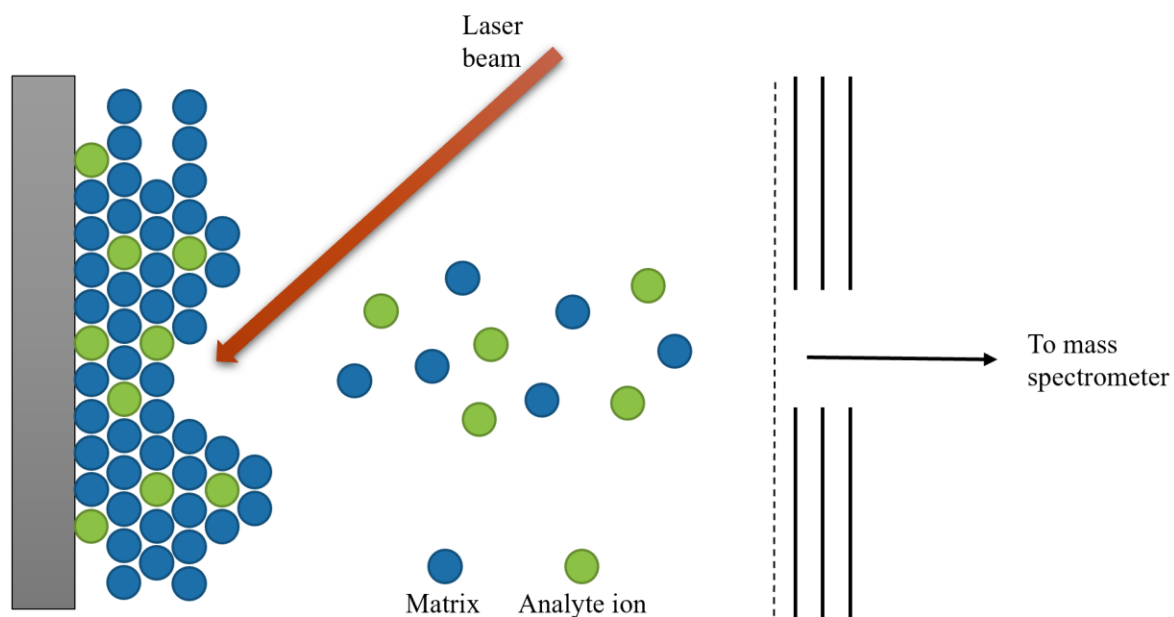
Figure 6 – Matrix-assisted Laser desorption ionization

2.2 Microfluidic Reactors

Microfluidic reactors date back to 1940 when they were first described as thin layer apparatuses for electrophoretic separations [47]. These original microreactors were capillary tubes with inner diameters on the order of microns used for various chromatography experiments [48]. Microfluidic reactors have gained recognition for use with chemical analysis and sensing in the early 1990s as a way to eliminate time consuming analytical chemistry methods. Since their reemergence microreactors have been improved and applied to numerous different reactions in a variety of applications [49].

The main uses for microreactors have been in research and academia; however, they have gained some attention in industry over the past 30 years. Primary uses include obtaining the chemical information of reactors [50], synthesis for industrial applications [51], and safer operating conditions [52], as well as green chemistry applications [53]. Microreactors have also been shown to have advantages over traditional benchtop laboratory chemistry such as having a smaller footprint [54], using less reagent [55], higher space-time yields [56], and a decrease in residence time and selectivity [57]. Microreactors have found an important role in the synthesis and monitoring of an expansive list of reactions. These reactions fall into several different categories including, but not limited to, aromatic chemistry, biochemistry, carbonyl chemistry, electrochemistry, and catalysis [49]. Among the biochemical reactions that have been reported in microreactors are the biosynthetic process of transesterification of soybean oil [58], the optimization of glycosylation [59], the synthesis of oligosaccharides [60], the purification of nucleic acids [61], protein digestion [62], and the enzymatic synthesis of β-glucosylglycerol [63].

2.2.1 Microfluidic Devices on Biochemical Applications

Several research teams have used microfluidic reactors to look at varying DNA reactions in microfluidic reactors. In 1996, two articles from Peter Wildings research group published work on the polymerase chain reaction (PCR) for DNA [64] [65]. Shoffner et al. determined the surfaces that will enable PCR. Their focus was on silicon and treated silicon effects on the reaction in a microfluidic device in order to perform PCR. They found that uniform deposition of the surface treatments was ideal for repeatable PCR which were best achieved with SiO2 and Si3N4 [64]. Cheng et al. also investigated PCR systems by comparing conventional PCR with PCR performed in silicon chips and plastic tubing. Using different reaction mixtures, they were able to demonstrate effective isolation of both red and white blood cells subsequently performed PCR. [65].

Moser et el. developed a biosensor to detect glutamic pyruvic transaminase (GPT) and glutamic oxaloacetic transaminase (GOT), which are indicators for liver disease and liver damage respectively. The system utilized a microfluidic reactor with a fixed reactor volume of 70 μL, reactor length of 170 mm and a reaction time of 4.5 minutes. The device consisted of an inlet, a reaction section with electrodes which were the sensors for their reaction. They report using no enzyme during this reaction, less reagent and high resolution in their results [66]. Hadd et al. used a microfabricated channel network to compare Michaelis-Menton constants of β-galactosidase enzymatic reactions with traditional reactor constants. They paired their microfabricated device with laser-induced fluorescence for detection of the hydrolysis product during the reaction to derive the Michaelis-Menton constants by using electrokinetic-induced fluid control. They were able to determine the inhibition of β-galactosidase by using three different mixtures of phenylethyl β-D-thiogalactoside by measuring the hydrolosis product concentration along the reactor path [67].

There are numerous applications of microfluidic devices that focus on protein digestion, separation and identification processes. Many of these are paired with electrophoresis [68] [69], chromatography, electrospray ionization - mass spectrometry (ESI-MS) [70] [71] methods. Bousse et al. developed a microfluidic device that is capable of automating the steps for protein sizing assays including separation, staining, de-staining, and detection. The microfluidic device consisted of microwells connected by microchannels between each of the steps involved. The chips were fabricated from soda lime glass that was wet-etched with photolithography. Detection was performed using an epifluorescent bioanalyzer. By integrating multiple operations on the same chip, this assay significantly decreased the overall time spent by 4 magnitudes over conventional SDS-PAGE techniques [69].

Xu et al. used a microfluidic device fabricated by laser machining a polycarbonate chip. They demonstrated lower flowrates and enhanced sensitivity ESI-MS of oligonucleotide before and after dialysis. They also successfully performed rapid de-salting of DNA and protein samples prior to ESI-MS, without a protein charge-state envelope [70]. Work by Jiang et al. in 2001 involved the miniaturization of hollow fiber dialysis for affinity capture, concentration, and separation. The products from these hollow fibers were sent directly for analysis by electrospray ionization. In this work the authors scale down the concept using two microfluidic devices fabricated from copolyester and poly(dimethylsiloxane) (PDMS) using imprinting and capillary molding techniques. With these microdialysis devices, the team was able to efficiently fractionate and cleanup complex biological samples prior to ESI-MS analysis. Specifically, this effort demonstrated rapid and sensitive analysis of alfatoxin B1, antibody, and aflatoxins. This resulted in higher sensitivity measurements with the ESI-MS. They reported achieving a significant reduction in dead volume, sample consumption and sample loss [71].

2.2.2 Microfluidic Reactor Design Equations

Microfluidic reactor design and fabrication can vary in structure and in materials used. Complicated designs include passive mixers, hydrodynamic focusing geometries [72], continuous-flow mixing regimes, high surface-to-volume ratios, high thermal transfer efficiencies, and segmented flow regimes. Microfluidic reactors follow the same standard chemical engineering reactor design principles derived from mole balances of a particular system or reactor type. Generally speaking, reactors, fall into two main reactor types: batch and continuous. Under batch conditions, there are no inlet or outlet streams of reagents or products while the reaction progresses. Batch reactions are commonly used for development purposes, small-scale operations and reactions that cannot performed in a continuous reactor. The general mole balance equation for a reactor is given by the following equation:

$$F_{i0} - F_i + G_i = \frac{dN_i}{dt} \tag{6}$$

where F_{i0} is the molar flow rate (moles/time) of species i into the system, F_i is the molar flow rate (moles/time) of species i out of the system, G_i is the generation (moles/time) of species i within the system, and $\frac{dN_i}{dt}$ is the rate of accumulation (moles/time) of species i within the system. For a reactor operating at steady-state, the accumulation is zero. The generation of species, i, is a function of the reactor volume and the reaction rate law of species i as follows:

$$G_i = \int_0^V r_i dV \tag{7}$$

where V is the volume of the reactor, r_i is the rate of formation (mole/time*volume) of species i. Substituting into equation (7) above we arrive at:

$$F_{i0} - F_i + \int_0^V r_i dV = \frac{dN_i}{dt} \tag{8}$$

For a batch reactor there is no inlet or outlet flow therefore $F_{i0} = F_i = 0$. Applying this and integrating, we arrive at:

$$\frac{dN_i}{dt} = r_i V \qquad (9)$$

Rearranging and substituting in a first order reaction rate law,

$$\frac{1}{V}\frac{dN_i}{dt} = -kC_i \qquad (10)$$

Substituting $N_i = C_i V$,

$$\frac{dC_i}{dt} = -kC_i \qquad (11)$$

Integrating,

$$-\int_{C_{io}}^{C_i}\frac{dC_i}{C_i} = \int_0^t k\, dt = k\int_0^1 dt \qquad (12)$$

Applying boundary condition that at $t = 0, C_i = C_{i0}$ so that

$$ln\left(\frac{C_{io}}{C_i}\right) = kt \qquad (13)$$

Rearranging so that $C_i(C_{i0})$

$$C_i = C_{i0}e^{-kt} \qquad (14)$$

We know

$$C_j = C_{i0} - C_i = C_{i0}e^{-kt} \qquad (15)$$

Rearranging,

$$ln\left(\frac{C_{io}-C_j}{C_i}\right) = -kt \qquad (16)$$

As the name suggests, continuous reactors operate continuously, with reagents replenished and products removed through inlet and outlet ports respectively. There are two types of continuous

reactors: continuous-stirred tank reactors (CSTR), and tubular reactors. Much like a batch reactor, a CSTR utilizes a tank or vat as the reaction location with inlet and outlet streams in place. In tubular reactors, the reaction progresses as the reagents flow down the reactor path. Tubular reactors may be modeled as cylinders or channels as seen in figure 7.

$$V_{cyl} = \pi r^2 l$$

a. Cylindrical Tubular Reactor

$$V_{ch} = l * h * w$$

b. Channel Tubular Reactor

c. Mole balance on species i in volume ΔV
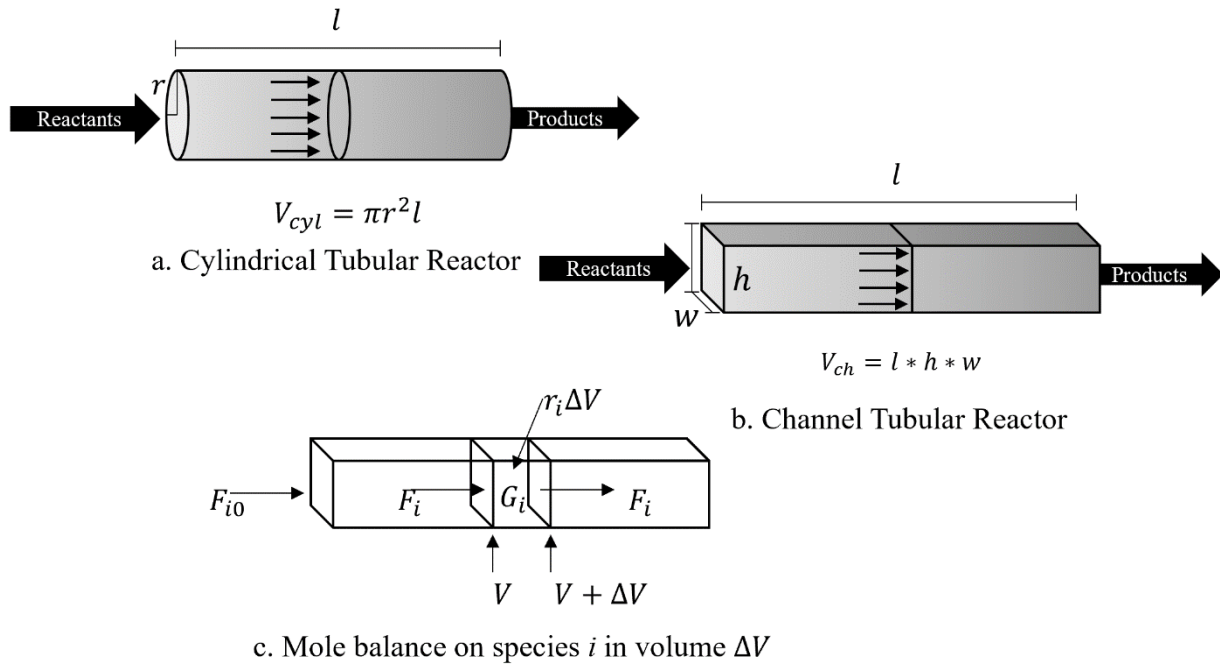
Figure 7 – Tubular reactor types a. cylindrical reactor, b. channel reactor, and c. mole balance on channel reactor.

Beginning with the general mole balance described by equation 3, for a reactor operating at steady-state, the accumulation is zero. The generation of species, I, is a function of the reactor volume and the reaction rate law of species i as follows:

$$G_i = \int_0^V r_i dV \tag{17}$$

where V is the volume of the reactor, r_i is the rate of formation (mole/time*volume) of species, i. Substituting into equation (17) above, we arrive at:

$$F_{i0} - F_A + \int_0^V r_i dV = 0 \tag{18}$$

By dividing equation (18) by ΔV and taking the limit as ΔV approaches zero we obtain the differential form of steady-state mole balance.

$$\frac{dF_i}{dV} = r_i \qquad (19)$$

In order to quantify how far a reaction progresses, we must define an important unitless parameter known as the conversion, X. The conversion of species, i, is defined as the number of moles of i that have been reacted per mole of i fed to the system. For flow systems, the conversion is a function of the reactor volume. The molar rate of species i reacting within the system is $F_{i0}X$. We can use the conversion to relate the exiting molar flow rate to the entering flow rate of species i by:

$$F_{i0} - F_{i0}X = F_i \rightarrow F_i = F_{i0}(1 - X) \qquad (20)$$

Differentiating F_{i0}

$$dF_i = -F_{i0}dX \qquad (21)$$

Substituting into equation (19)

$$F_{i0}\frac{dX}{dV} = -r_i \qquad (22)$$

We can rearrange, integrate and apply the limits of $V = 0$ then $X = 0$ to arrive at the volumetric design equation for a flow reactor:

$$V = F_{i0} \int_{X_{in}}^{X_{out}} \frac{dX}{-r_i} \qquad (23)$$

Such that

$$V = \frac{F_{i0}X}{-r_i} \qquad (24)$$

2.2.3 Microfluidic Reactor Fabrication

Common fabrication techniques include wet chemical etching and bonding techniques [73], micromachining and soft lithography [74], and ion etching [50]. Silicon wafers and glass slides with poly(dimethylsiloxane) (PMDS) or Poly(methyl methacrylate) (PMMA) bonded to them are the most frequently used materials. These materials have their drawbacks with regards to manufacturing and scalability [75]. One of the major hinderances with using on-line Raman spectroscopy of PDMS microfluidic devices is the high spectral response reported from PDMS [76]. Recently, there has been interest for translational, low-cost devices and researchers have increased use of 3D printing microfluidics devices [77]. There have been reports on real-time monitoring that have included microfluidic devices paired with techniques such as ultraviolet/visible spectroscopy [78], Infrared spectroscopy [79], near-infrared spectroscopy, atomic force microscopy [80], electrochemical detection [81], and Raman spectroscopy [82].

2.3 Raman Spectroscopy

Raman spectroscopy has been paired with microfluidic reactors to analyze the selectivity, space time yield, and reaction conversion rate along the reactor path for numerous chemical reactions. Combining Raman spectroscopy with microfluidic devices allows for chemical monitoring and detection of a variety of reactions in real time [83]. Raman spectroscopy has previously been used to study various reactions in microfluidic devices including catalytic CO_2 behavior [84], and two-phase extraction of nitric acid [85]. Raman spectroscopy is advantageous to use on solid and liquid samples because of its inherent differentiation between minute features [86] [87]. Shifts in Raman spectral peaks can relate to strain in these structures (i.e. negative shifts in wavenumber indicate tensile strain and positive shifts in wavenumber indicate compressive

strain). The appearance of strain may also be attributed to thermal heating [88] or pressure [89]. Raman spectroscopy utilizes an excitation laser to interrogate the sample of interest. The excitation laser wavelength interacts with the vibrational modes of the sample resulting in an energy shift from the original wavelength illustrated in figure 8. This shift in energy is collected by the spectrometer and detector to produce a spectral graph which yields molecular modes that may be identified as out of plane vibration (γ), torsion (τ), bending (δ), rocking (r), wagging (ω), and stretching (ν) modes. The energy is supplied to the system from the laser is either transmitted, absorbed, or scattered. The spectral shift received is also a measure of the energy reflected back from the system and can be quantified by the area under the spectral graph with knowledge of the excitation laser wavelength power density received at the sample. It is known that there are energy losses from the laser excitation source to the sample stage.
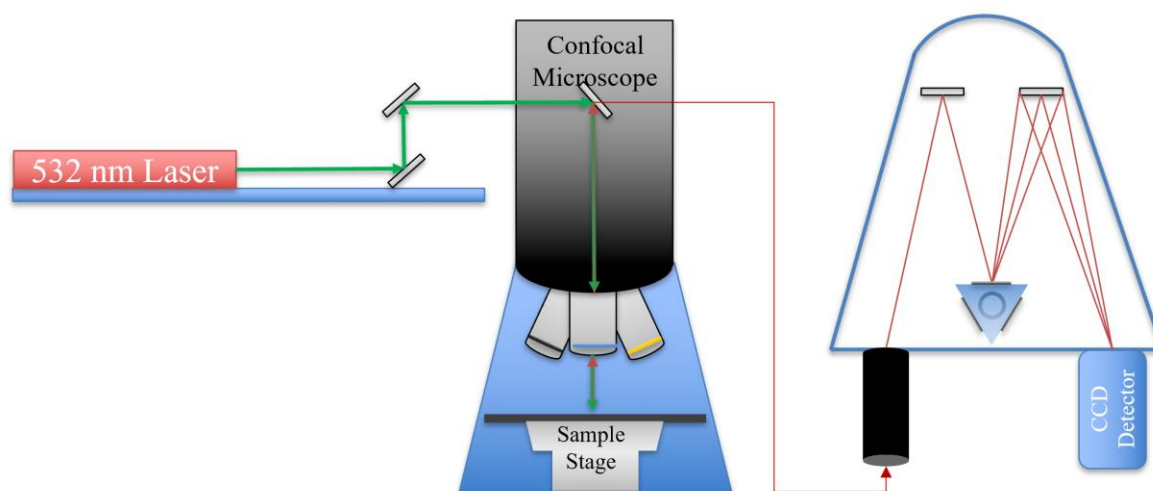
Figure 8 – Raman Spectrometer setup

Several analytical techniques have been employed to extract valuable reactor kinetic information from collected Raman spectra. Principal component analysis (PCA) is a useful mathematical method that can be applied to decipher salient features in the spectral data [90] [91].

PCA compresses multi-dimensional data into principal components (PCs), which represent the primary components of the variance in the signals [92]. This technique can aid in deciphering biochemical reaction mechanisms from Raman spectral data. The following chapter details how standard PCA may be applied to analyze Raman spectra and the development of an adaptive PCA method to identify subtle perturbations in biomolecular structures.

2.4 Materials

Below is a list of the materials and samples used throughout this study:

- L-leucine (powder) from non-animal source, meets European, Japan and United States pharmacological (EP, JP, and USP) testing specifications, suitable for cell culture, 98.5-101.0% assay. CAS: 61-90-5, $C_6H_{13}NO_2$, MW: 131.17 g/mol. Purchased from Sigma Aldrich.

- L-valine (powder) from non-animal source, meets EP, JP, and USP testing specifications, suitable for cell culture, 98.5-101.0% assay. CAS: 72-18-4, $C_5H_{11}NO_2$, MW: 117.15 g/mol. Purchased from Sigma Aldrich.

- L-isoleucine (powder) from non-animal source, meets EP, JP, and USP testing specifications, suitable for cell culture, 98.5-101.0% assay. CAS: 73-32-5, $C_6H_{13}NO_2$, MW: 131.17 g/mol. Purchased from Sigma Aldrich.

- L-serine (powder) from non-animal source, meets EP, JP, and USP testing specifications, suitable for cell culture, 98.5-101.0% assay. CAS: 56-45-1, $C_3H_7NO_3$, MW: 105.09 g/mol. Purchased from Sigma Aldrich.

- L-threonine (powder) from non-animal source, meets EP, JP, and USP testing specifications, suitable for cell culture, 99.-101.0% assay. CAS: 72-19-5, $C_4H_9NO_3$, MW: 119.12 g/mol. Purchased from Sigma Aldrich.

- Protein Kinase A 3′,5′-cyclic-AMP-dependent from bovine heart (lyophilized powder, ≥0.4 units/μg protein) CAS: 9026-43-1, Enzyme Commission (EC): 2.7.1.37. Purchased from Sigma Aldrich.

- Adenosine 3′,5′- cyclic monophosphate (powder), ≥98.5% HPLC. CAS: 60-92-4, EC: 200-492-9, $C_{10}H_{12}N_5O_3P$, MW: 329.21 g/mol. Purchased from Sigma Aldrich.

- Adenosine 5′- diphosphate sodium salt (powder), ≥95% HPLC. CAS: 20398-34-9, $C_{10}H_{15}N_5O_{10}P_2$, MW: 427.2 g/mol. Purchased from Sigma Aldrich.

- Adenosine 5′- triphosphate disodium salt hydrate (powder), ≥99% HPLC. CAS: 34369-07-8, $C_{10}H_{14}N_5Na_2O_{13}P_3$, MW: 551.14 g/mol. Purchased from Sigma Aldrich.

- α-Casein dephosphorylated from bovine milke (lyophilized powder), MDL: MFCD00130477. Purchased from Sigma Aldrich.

- Casein from bovine milk (purified powder). CAS: 9000-71-9, EC: 232-555-1, MDL: MFCD0081481. Purchased from Sigma Aldrich.

Chapter 3: Spectral Data Analysis

This chapter will present a methodology for extracting salient features from structurally similar biomolecules under varying experimental parameters. One of the critical components of this research is the spectral data analysis of accumulated/acquired spectra during protein phosphorylation reactions. Raman spectroscopy as a means of identifying molecular conformation and the experimental variables used to induce salient features is described in this chapter. Understanding the capabilities of the Raman spectroscopy technique and identifying signal noise that may affect analysis are crucial for studying biochemical reactions. Three branched chain amino acids (BCAAs), L-leucine, L-valine, and L-isoleucine were chosen because of their structural similarities and these are presented below. This chapter will introduce branched chain amino acids, their role in the body and the significance on molecular conformation on biochemical reactions. The volume of Raman spectroscopy data gathered during real-time monitoring is tedious to analyze. However, statistical techniques, such as principal component analysis (PCA) have been successful in analyzing spectral data [90] [93]. PCA compresses multi-dimensional data into principal components (PCs), which represent the primary components of the variance in the signals [94]. Previous studies have implemented PCA to time-domain spectroscopy [95] and X-ray absorption spectroscopy [96] to differentiate various polymers. While variance is not always considerable in terms of magnitude, several studies detailed by Smith and Campbell demonstrate that principal components with low variance are significant for contextualizing solutions [97]. In this chapter PCA is described as it is traditionally applied to spectral data and the limitations of what information it can relay. To overcome these limitations, an adaptive PCA method was developed that identifies the salient information of the spectral data. The adaptive PCA method allows Raman spectra to be leveraged for modeling strain conditions in a molecular network. The

adaptive method is executed on the spectral data collected for the three BCAA's listed above as experimental conditions are varied. In addition, blended samples of the BCAA's were created with varying ratios to extract salient features as a result of composition. The collection of Raman spectra will be presented for the individual and blended samples of the branched chain amino acids. Data Analysis using principal component analysis (PCA) is presented by first introducing the fundamental methodology of PCA. Results include standard PCA biplots for the individual amino acids and adaptive PCA for the individual and branched chain amino acids.

3.1 Branched Chain Amino Acids

Amino acids are the essential building blocks of all proteins with 22 proteinogenic amino acids known. Aside from protein synthesis, amino acids play important roles in human health and disease. While the body can synthesize many of the necessary proteinogenic amino acids, there are some amino acids that the body cannot synthesize and therefore, must be obtained through diet [98]. These are referred to as essential amino acids. Branched-chain amino acids (BCAA) including the three chosen in this study (L-leucine, L-valine and L-isoleucine), are considered essential amino acids. Because detection of BCAAs is crucial to diagnosing associated diseases and disorders, monitoring catabolic reactions involved in the degradation of BCAAs in patients would enable early disease detection and improved prognosis monitoring. Unfortunately, a strategy is still lacking with regards to real-time monitoring of the conformational changes and strain states associated with biochemical reactions because these changes are fast and the molecules are small.
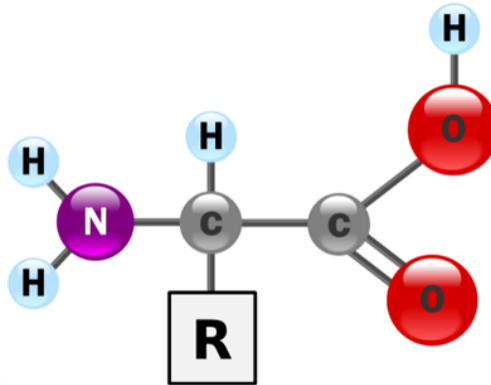
Figure 9 - Basic structure of an amino acid with a functional group, R.

The basic structure of an amino acid contains an amine (NH_2) and carboxyl (-COOH) group in addition to a side chain (R) that is specific to each amino acid. This is illustrated in Figure 9. There are also several metabolic disorders linked to amino acids such as phenylketonuria [99], tyrosinemia [100], homocystinuria [101], non-ketotic hyperglycinemia [102], and maple syrup urine disease [103]. The body relies on amino acid mechanisms for energy production, transamination, signaling pathways, and protein folding [104]. Protein folding, specifically, is the self-organization of amino acid linear chains, dictated by the specific sequence of the amino acids. The folding process begins with the primary structure, the linear amino acid chain, folding into alpha helices or beta sheets. The folding process occurs through the rotation of the peptide backbone to orient according to the amino acid functional groups. Whereas intramolecular hydrogen bonds stabilize these structures creating characteristic hydrophobic and hydrophilic sides to the alpha helices and beta sheets, they subsequently fold further lining up the hydrophobic and hydrophilic sides to form the tertiary structure of proteins. Figure 10 shows the folding process of proteins.
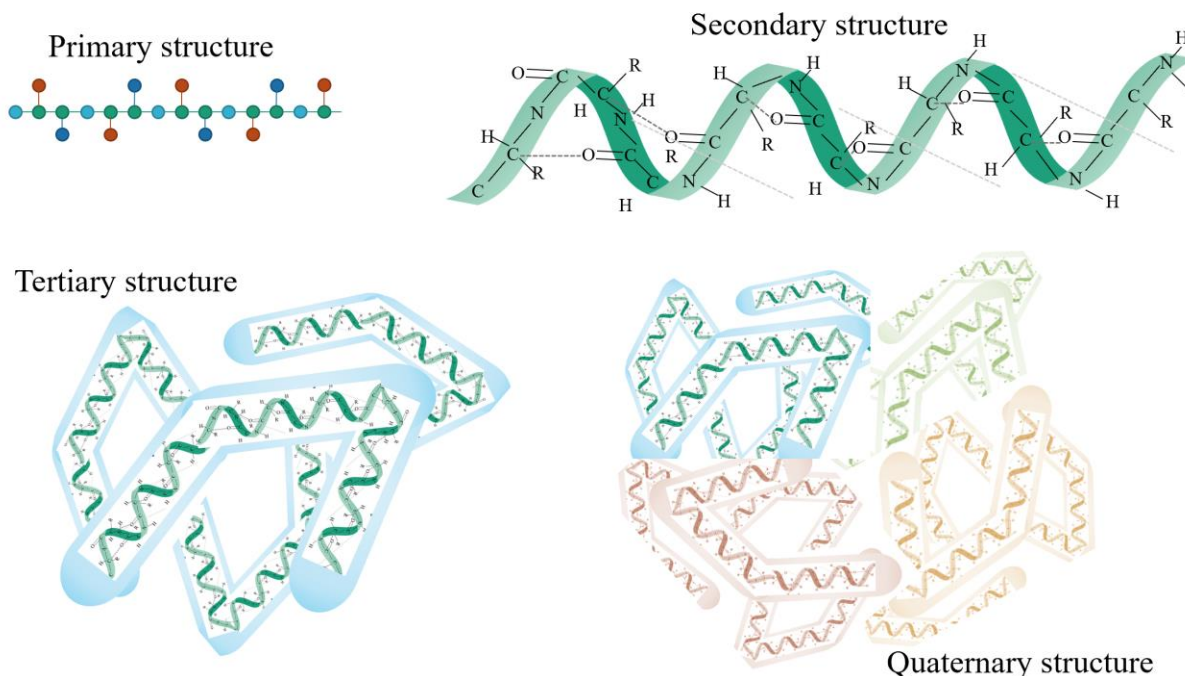
Figure 10 - Protein Folding steps: a) primary structure of linear amino acid chains, b) secondary structure of beta sheets and alpha helices, c) tertiary structure, d) quaternary structure

The conformation of a molecule refers to the structural arrangement of its atoms and may be an indicator that a reaction is occurring or has occurred [105]. Studies have shown that conformation plays an important role in the biological activity of biomolecules [106]. Figure 11 shows a chiral generic amino acid in two conformational states. Chirality is a term used in several branches of science that refers to a mirror image that is not superimposable. The two conformational states of a generic amino acid in are mirror images of each other, but do not line up when the images are placed on top of one another. Since two conformational states can have the same molecular make-up of atoms it is pertinent to select a characterization instrument that can decipher precise molecular fingerprints. Raman spectroscopy is a highly sensitive technique can be used to identify a molecule's conformational state. Shifts in Raman spectra (peaks) can be associated with strain in these structures (i.e. negative shifts in wavenumber indicate tensile strain and positive shifts in

wavenumber indicate compressive strain). The appearance of strain may also signify thermal heating [88] or pressure [89].
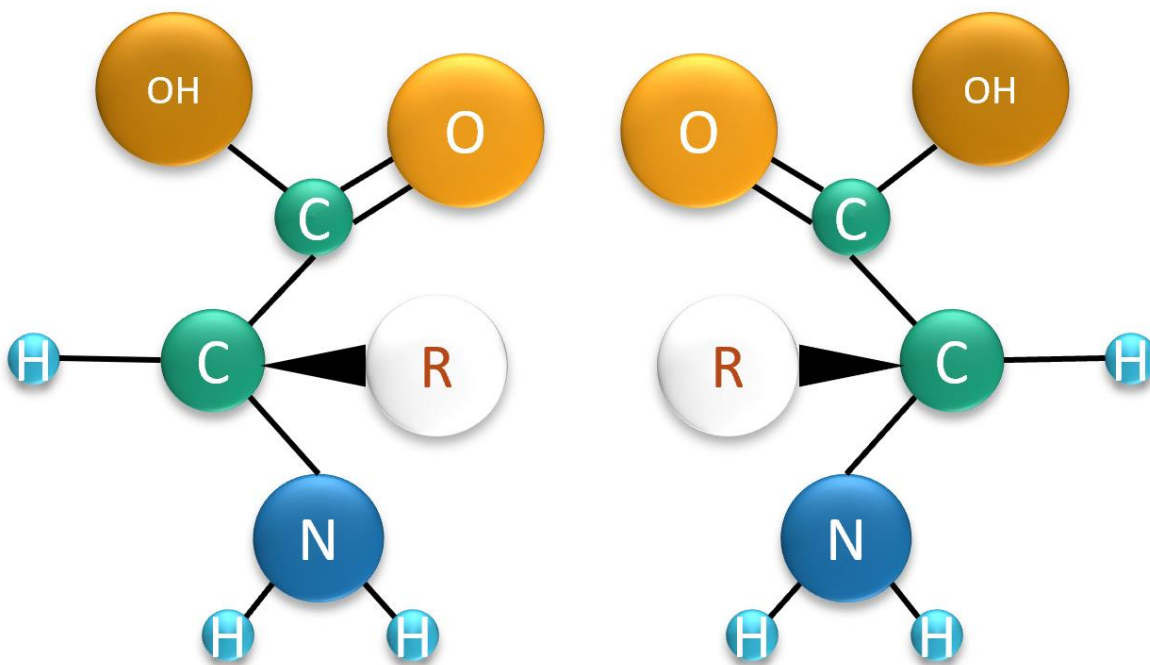
Figure 11 – Chiral molecule (generic amino acid) in its two conformational states.

In this work, application of standard principal component analysis (PCA) and an adaptive PCA is executed on Raman spectral data for these three BCAAs at varying excitation laser power densities and stage temperatures. These techniques have been implemented on individual amino acids and blended amino acids to differentiate individual vibrational modes within complex samples (as a function of phonon scattering and laser power density).

3.2 Data Collection

The individual amino acids (purchased from Sigma Aldrich) satisfy United States Pharmacological standards and are verified to be ≥ 98% by the supplier. The blended samples were created by dissolving the three individual amino acids in four different ratios: 1:1:1, 2:1:1, 1:2:1, and 1:1:2 in distilled water. Samples were then allowed to recrystallize and baked at 50°C to remove moisture. These ratios were chosen so that we may evaluate equal concentrations as well as the naturally occurring ratio of 2:1:1 in the body. We included the 1:2:1 and 1:1:2 ratios to evaluate deficient ratios that may occur in the body. X-ray Diffraction was performed on control samples to verify purity and determine crystal structure.

Raman spectroscopy was collected using a custom Jobin Yvon BX41 Raman microscope equipped with a Horiba iHR550-imaging spectrometer with 1800 gr/mm groove density, a Synapse CCD detector and a 532 nm laser line (1μm spot size) is used to collect spectroscopic data on the BCAAs. The Synapse CCD detector has a spectral resolution of ~0.8 cm^{-1} and the optical path length of the spectrometer is 0.55 m, providing superb quality of spectral imaging. The quantity of spectral data sets is on the order of hundreds of scans. Because the instrument's detector has such high spectral resolution each data spectral acquisition contains over 7000 unique data points over the spectral range scanned. During spectral acquisition, an optical power meter was placed beneath the optically transparent sample stage to collect transmission of the 532 nm laser line through crystalline samples. This set up can be seen in figure 12. Thermal changes were introduced through the use of a controllable micro-stage heater coupled with the Raman spectrometer. The temperature of the stage varied between 22-62°C in 10°C increments. This temperature range was

chosen to cover room temperature and the temperature in vivo. The optical power meter was positioned under the stage heater to collect the optical power transmitted during acquisition.
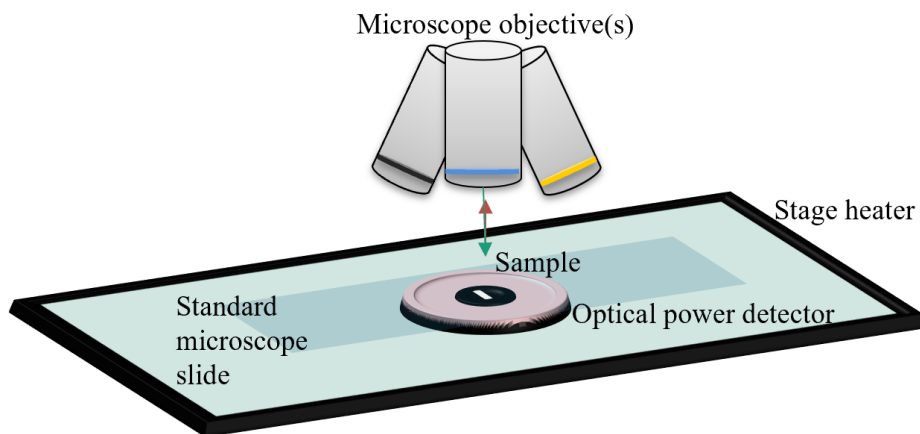
Figure 12 - Raman spectroscopy setup incorporating an optical power meter behind the sample stage and stage heater for addition of thermal energy.

Sample data is provided in Table 1. It shows the laser power settings for the 532 nm excitation laser equipped on the Raman spectrometer, the optical power received at the stage measured by the optical power meter described in figure 12 and the power density received at the stage calculated by the laser beam diameter of 1μm. Table 1 also shows the stage temperatures with the standard deviation based on recorded temperatures during each spectral acquisition over the entirety of this study. As mentioned above, it is important to measure strain states in real time. Simulated strain states in amino acids have been reported in the literature and are characterized by vibrational modes. Figure 13 represents the chemical structures of the three BCAA's used in this chapter with their functional groups highlighted in red and example vibrational modes circled in blue. The strain states are denoted by τ, torsion; δ, bending; r, rocking; w, wagging; γ, out-of-plane

vibration; ν, stretching associated with particular bonds. Data sets are also grouped according to

each parameter while varying the other.

Table 1 – Raman spectroscopy parameters used for the design of experiment.

532 nm Excitation Laser Settings				Stage Temperature Settings	
Label	Power supply setting	Power received at stage	Power density received at stage	Label	Temperature
A.	5 mW	1.9 mW	$6.05 \, x10^4$ W/cm^2	i.	23.6±0.15°C
B.	10 mW	2.1 mW	$6.68 \, x10^4$ W/cm^2	ii.	32.50±0.01°C
C.	15 mW	3.9 mW	$1.25 \, x10^5$ W/cm^2	iii.	42.5±0.01°C
D.	20 mW	4.7 mW	$1.50 \, x10^5$ W/cm^2	iv.	52.5±0.01°C
E.	25 mW	6.6 mW	$2.09 \, x10^5$ W/cm^2	v.	62.5±0.02°C
F.	30 mW	7.2 mW	$2.29 \, x10^5$ W/cm^2		
G.	35 mW	9.2 mW	$2.94 \, x10^5$ W/cm^2		
H.	40 mW	9.9 mW	$3.15 \, x10^5$ W/cm^2		
I.	45 mW	11.9 mW	$3.78 \, x10^5$ W/cm^2		
J.	50 mW	13.2 mW	$4.20 \, x10^5$ W/cm^2		
K.	55 mW	14.5 mW	$4.63 \, x10^5$ W/cm^2		
L.	60 mW	15.9 mW	$5.05 \, x10^5$ W/cm^2		
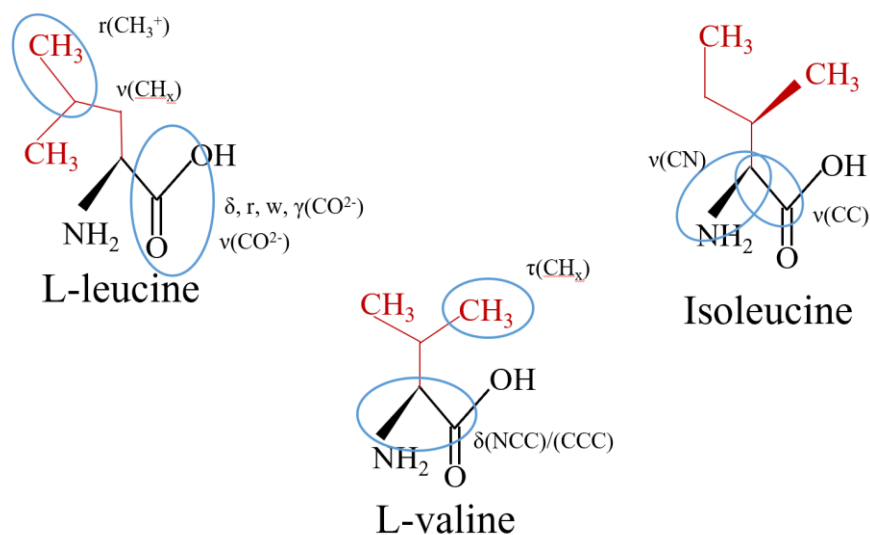
Figure 13 - Chemical structure of L-leucine, L-valine, and L-isoleucine with representative stress-states and vibrational mode assignment wavenumber ranges identified on the chemical structural formula for L-leucine, L-valine and L-isoleucine. τ, torsion; δ, bending; r, rocking; w, wagging; γ, out-of-plane vibration; ν, stretching. Raman spectroscopy setup incorporating an optical power meter behind the sample stage and stage heater for addition of thermal energy.

3.3 Data Analysis

Principal Component Analysis is a multivariant analysis tool that identifies the variance in data sets by reporting the principle coefficients (PC) of the data set. The number of principle coefficients generated by PCA is equal to the number of unique data sets analyzed with the % variance of all PC's summing to 100%. In this chapter, singular value decomposition (SVD) is applied to spectral data where the intensity values create an $(n \times p)$ matrix, where n corresponds to the observations and p corresponds to the variables measured. In this formulation, the Raman wavenumbers are treated as the n observations, and the p variables as the 60 unique spectral scans acquired in the DOE described above. This matrix, X, may be written as

$$X = ULA'$$

where U is the $(n \times r)$ matrix, A is the $(p \times r)$ matrix, L is the $(r \times r)$ diagonal matrix and r is the rank of X. The PC scores, z_{ik} may be calculated using the SVD by

$$z_{ik} = u_{ik} l_k^{1/2}, \qquad i = 1,2,\ldots n, \qquad k = 1,2,\ldots r,$$

The columns of the matrix product

$$Z \cdot A = ULA'A = UL$$

are the PC's of Z. In this chapter both standard and adaptive PCA will be executed on Raman spectroscopic data of BCAAs to extract salient features related to strain during various experimental parameters.

3.3.1 Standard Principal Component Analysis

Standard PCA may be executed across entire spectral acquisition sets, which would provide the PC's that account for the variance across the entire wavenumber range. The number of PC's that are responsible for the variance in the data sets will relay the number of tunable parameters in the data set. If PC1 is less than 100%, this would mean that there is variance in the data set. It would not tell you what accounted for the variance, nor where in the spectral scan the variance occurred significantly. Standard PCA was executed for each of the individual amino acids and the four blends for all 60 scans of their respective DOE.

3.3.2 Adaptive Principal Component Analysis

The adaptive PCA method used in this study is able to highlight principal coefficients that correlate to wavenumber sections in the spectral data by varying n observations in the matrix X. This method identifies where in the spectral data the most variance occurs. As with standard PCA, the adaptive PCA does not relay what the variance is a result of. Verification of the adaptive PCA algorithm was performed by executing on repeated data sets which yielded PC1 = 100%. To ensure instrument effects were not a source of variation, the adaptive PCA was executed on three spectral data sets collected at identical parameters and sample which yielded PC1 = 99.99%. Figure 14 illustrates different methods of applying PCA to spectral data. The top left represents traditional/standard PCA across the entire wavenumber range (in this case 2700-3000 cm^{-1}) and can only relay the variance across the whole range. The top right graph represents PCA applied to a single peak which is acceptable if the structure only has one to two vibrational modes that are easily isolated. The bottom left graph represents PCA applied to sections of wavenumbers successively. This is not ideal as it can cut off the vibrational modes into two sections or miss

vibrational mods. The bottom right graph represents overlapping sections of the wavenumber range. This method is the adaptive PCA method applied in this chapter and was chosen because it allows each peak to be centered by maintain the same sections sizes and stepping the window across the spectral range.
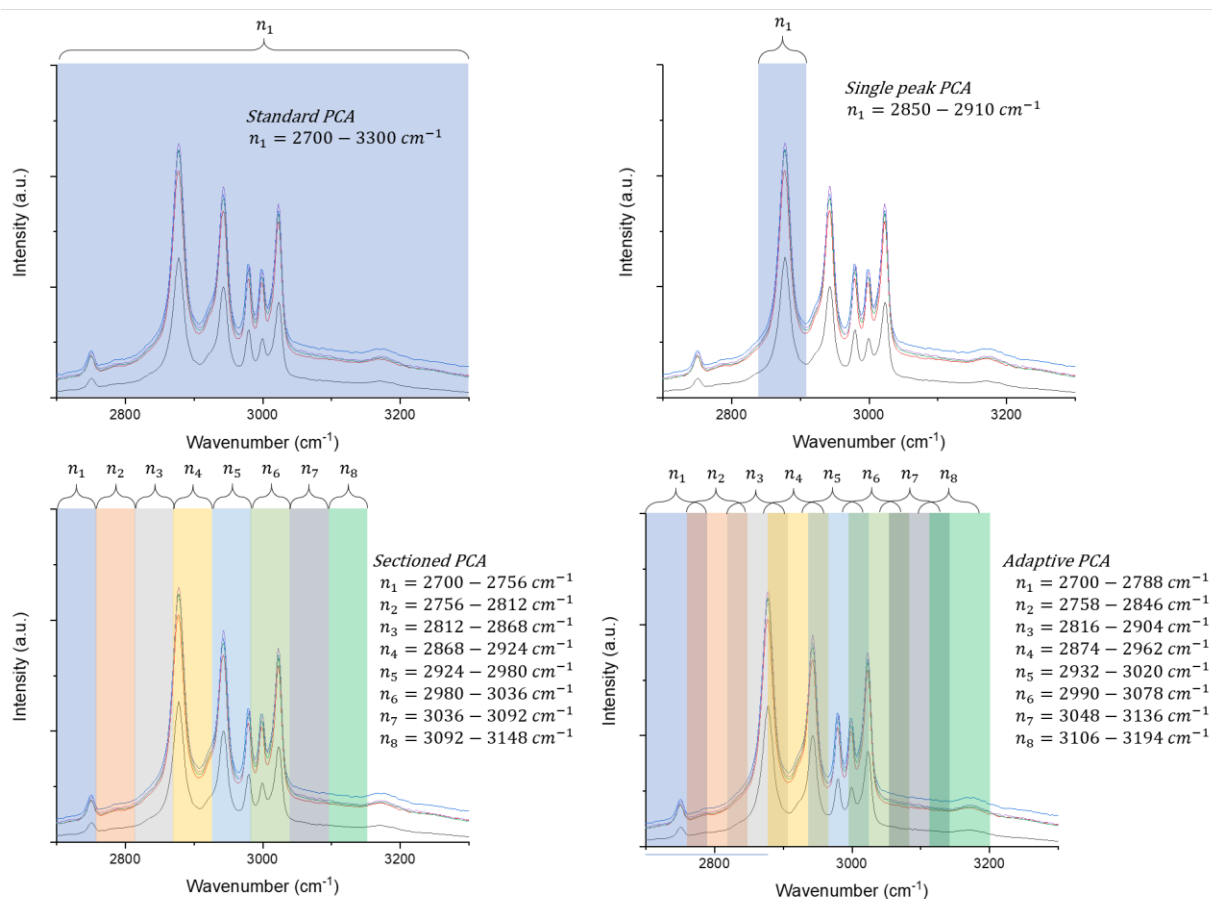
Figure 14 – Principal Component execution methods: (top left) standard PCA, (top right) single peak PCA, (bottom left) sectioned PCA, (bottom right) adaptive PCA.

3.4 X-ray Diffraction Data

X-ray powder diffraction was performed using PANalytical MPD X'Pert Pro with a CuK$_\alpha$ radiation source at 45kV and 40μA. Diffraction patterns were collected from 10-60°, with a step size of 0.0131° and 11.5 s/step on powder samples. The recorded X-ray diffraction patterns for the

individual BCAAs are shown in figure 15. Pattern matching using High Score fitting software showed the patterns were in agreement with the standards accepted by previous literature [107] [108] [109]. X-ray diffraction patterns for the blended BCAA samples are shown in figure 16. Peak shift and broadening, Lower peak intensity, and the formation of new peaks in these diffraction patterns show that there are changes in the unit cell lattice parameters, crystallite sizes and microstrain as well as new phases present during the recrystallization process.
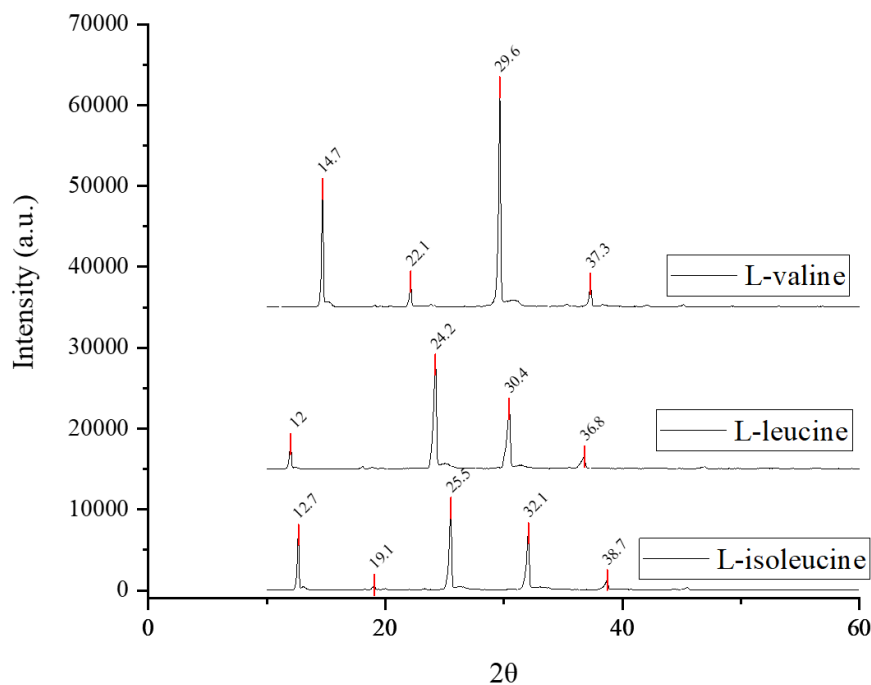
Figure 15 - X-ray diffraction pattern for L-leucine, L-valine and L-isoleucine at room temperature.
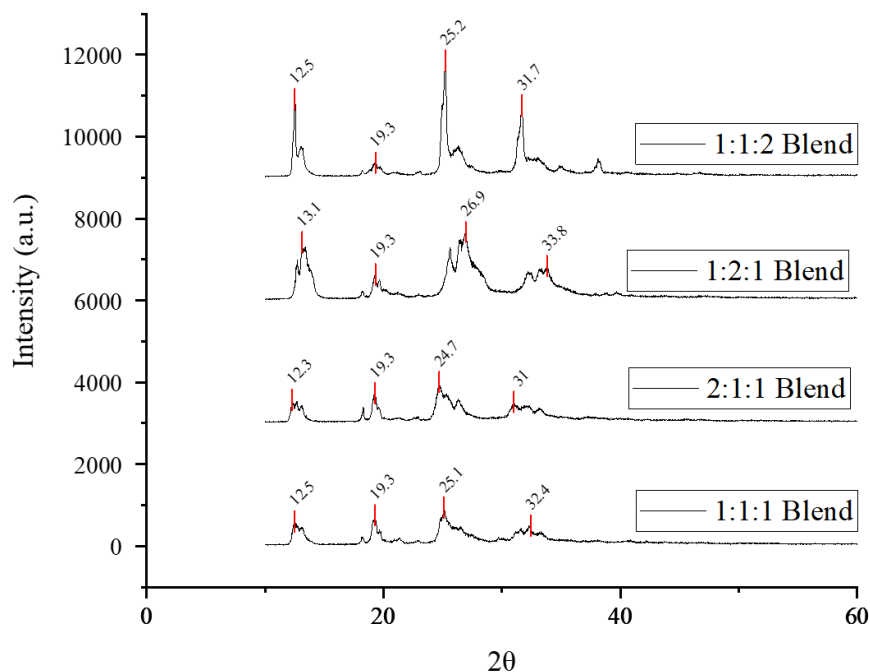
Figure 16 - X-ray diffraction pattern for blended samples of L-leucine, L-valine and L-isoleucine at room temperature in varying rations of 1:1:1, 2:1:1, 1:2:1, and 1:1:2 respectively.

3.5 Raman Spectral Data

3.5.1 Individual Branched Chain Amino Acid Spectra

In order to simulate strain, Raman spectra was collected on each individual branched chain amino acid at five different temperature settings using the microheater and 12 different laser power densities (as described in the methods section). This resulted in 60 unique spectral data sets for each sample. The following figures [17-19] show the Raman spectral data acquired for L-leucine, L-valine and L-isoleucine at 22°C at each laser power setting 5 to 60 mW. The Raman spectral data for L-leucine L-valine, L-isoleucine and the four blends for the remaining temperatures at each laser power setting were also acquired. For each of the individual BCAA and blended samples, the Raman response shows an increase in intensity as the laser power density is increased. This is to be expected, as more energy is supplied from the laser then greater Raman scattering

occurs, resulting in higher intensity received by the spectrometer. The importance of this work is to identify if every vibrational mode present in each sample responds the same to each increase in laser power density and increase in temperature. We are looking for the vibrational modes that are affected more than the others by using PCA to highlight these salient features. It is impossible to look at figures 17-19 and identify which vibrational modes respond greater than the others. Using the adaptive PCA method across the wavenumber range in increments will highlight the vibrational modes with the greatest variance, identify those that are affected by the laser power density and temperature.
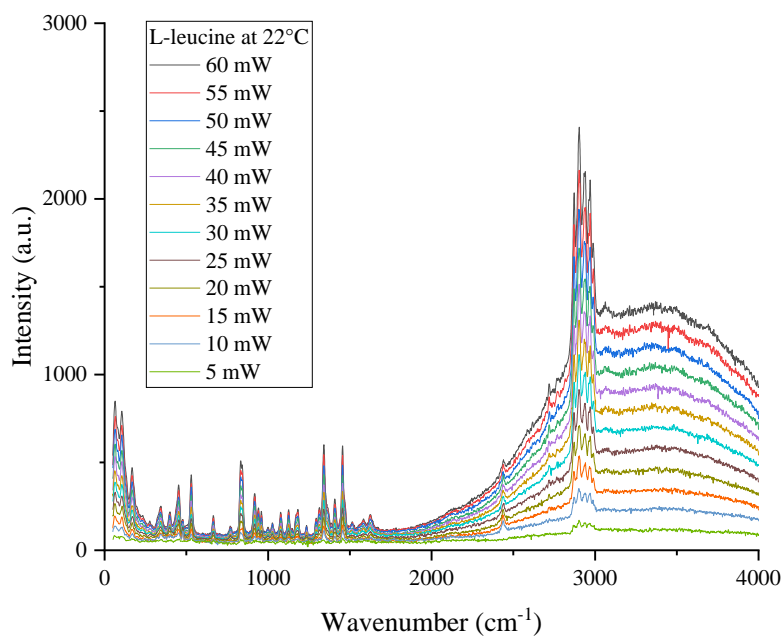
Figure 17 -Raman Spectra of L-leucine at 22°C for laser power settings 5-60 mW
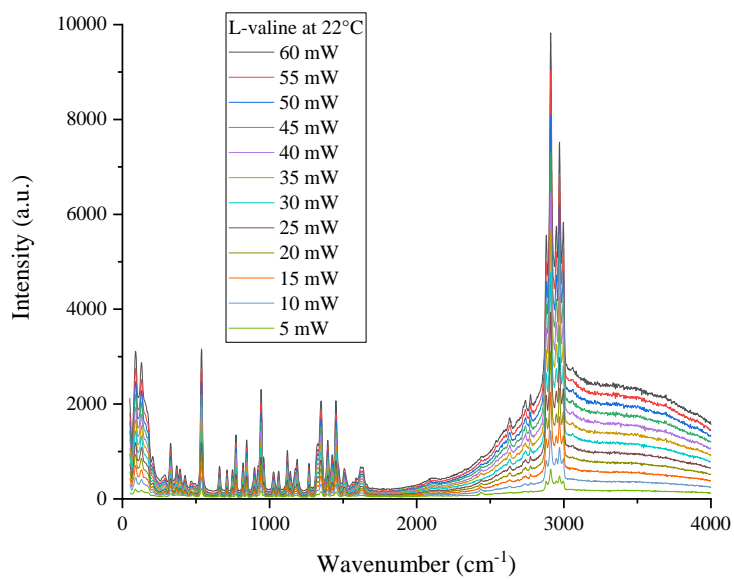
Figure 18 - Raman Spectra of L-valine at 22°C for laser power settings 5-60 mW
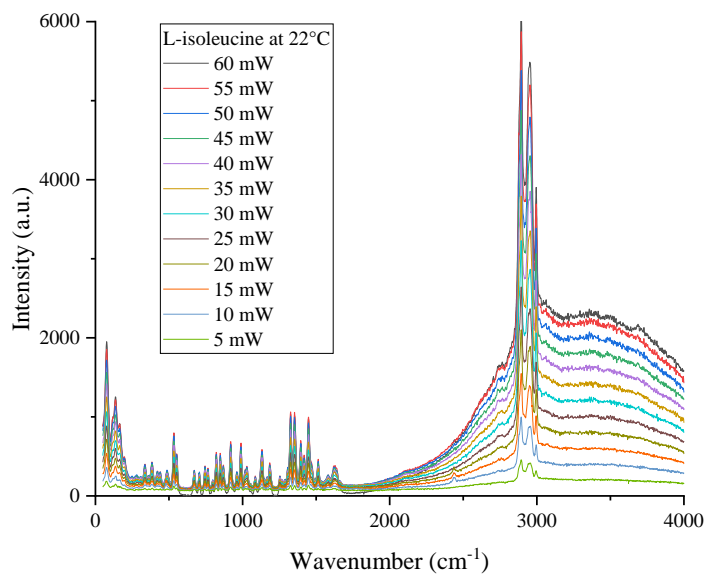
Figure 19 - Raman Spectra of L-isoleucine at 22°C for laser power settings 5-60 mW

3.5.2 Standard PCA Principal Coefficients

This method is the equivalent of method a in figure 14 (top left). The first five principal components (PCs) results are summarized in table 2 for each sample. The blend with the ratio of 1:2:1 resulted in the highest variance due to experimental conditions. The PC's here represent how each sample varies as a response to laser power density and temperature variations. To reiterate this data does not relate which vibrational mode is most affected within each molecule or what the variance is specifically attributed to. This variance is across the wavenumber region of 50-4000 cm^{-1} for all 60 scans. Thus, for L-leucine there is 98.65% similarity between all the scans and 1.28% dissimilarity. This essentially states that, for over 428,000 data points collected on L-leucine, there is 1.28% variance. Finding the wavenumber region where this variance is coming from is the driving motivation behind the adaptive PCA method.

Table 2 – Principal Coefficients from standard PCA execution on individual L-leucine, L-valine, L-isoleucine, and the four blends of ratios at 1:1:1, 2:1:1, 1:2:1, and 1:1:2 respectively.

	L-leucine	L-valine	L-isoleucine	BlendOne	BlendTwo	BlendThree	BlendFour
PC1	98.65%	98.95%	97.76%	99.22%	98.49%	95.61%	99.36%
PC2	1.28%	0.99%	2.19%	0.74%	1.47%	4.32%	0.57%
PC3	0.03%	0.02%	0.02%	0.01%	0.02%	0.02%	0.04%
PC4	0.01%	0.01%	0.01%	0.01%	0.01%	0.01%	0.01%
PC5	0.00%	0.01%	0.01%	0.00%	0.00%	0.01%	0.00%

3.5.3 Standard PCA Biplots for Individual Branched Chain Amino Acids

Standard PCA biplots were created for each amino acid relating the vibrational modes (n, observations), and the experimental parameters (p, variables). As with method b in figure 14 (top right), a section of the wavenumber region was chosen to cover the area with the most vibrational

modes present to try and isolate the variance source. The biplots were created using OriginPro standard PCA execution across wavenumber regions of 50-1700 cm^{-1}. The axis values are auto calculated to relate magnitude of the loadings to the score values. Figure 20 displays the biplot for L-leucine's vibrational modes reported. The standard PCA for L-leucine resulted in PC1 accounting for 91.48% in the wavenumber range of 50-1700 cm^{-1}. Interpreting this, the biplot loadings show that all the variables contribute the to the PC1 component by aligning closest to the x-axis. The vibrational mode observations can be seen in the scores, as the peaks rise they align in the same direction as the loadings. This suggests the variation is in the peaks and not the baseline. Figure 21 displays the biplot for L-valine's vibrational modes reported. The standard PCA for L-valine wavenumber range 50-1700 cm^{-1} resulted in PC1 accounting for 97.79%. The loadings show that the variables contribute to PC1 as well, but with a greater magnitude than that of L-leucine. The observations for L-valine show that the baseline is further left of the y-axis, suggesting they have less dependence on the loadings. Meaning the variables have less effect on L-valine's observations. Figure 22 displays the biplot for L-isoleucine's vibrational modes reported. The standard PCA for L-isoleucine resulted in PC1 accounting for 92.35% in the wavenumber range 50-1700 cm^{-1}. The loadings show that the variables contribute to PC1, compared to the others. The loadings contribute to a greater magnitude than L-leucine but less than the loadings of L-valine. This coincides with the overall percent of each PC1. The observation scores for L-isoleucine also show the baseline is further left of the y-axis than that of L-leucine, but not as far left than that of L-valine.
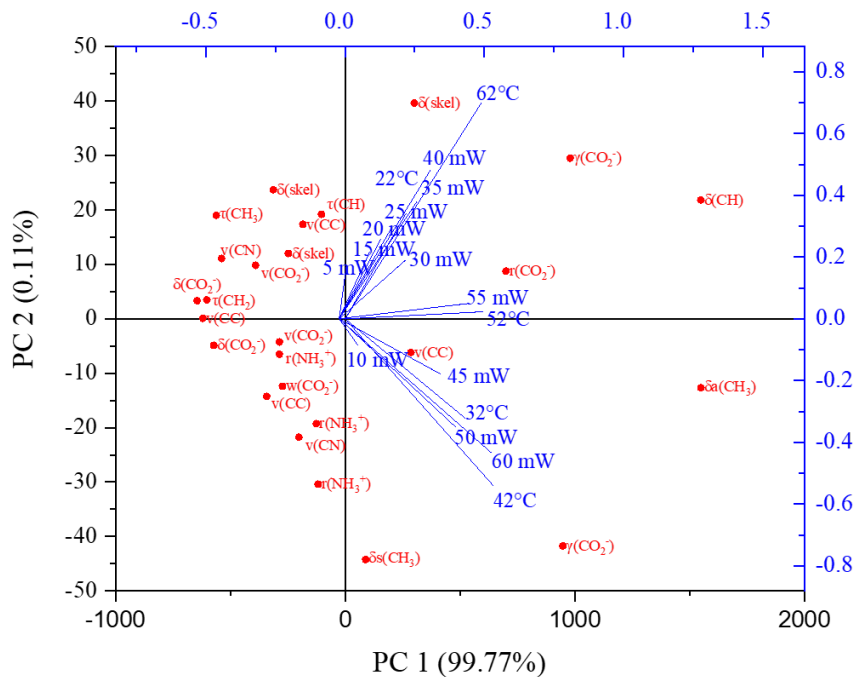
Figure 20 - L-leucine biplot for the scores of vibrational mode observations and the loadings of the 60 experimental variables across 50-1700 cm^{-1}
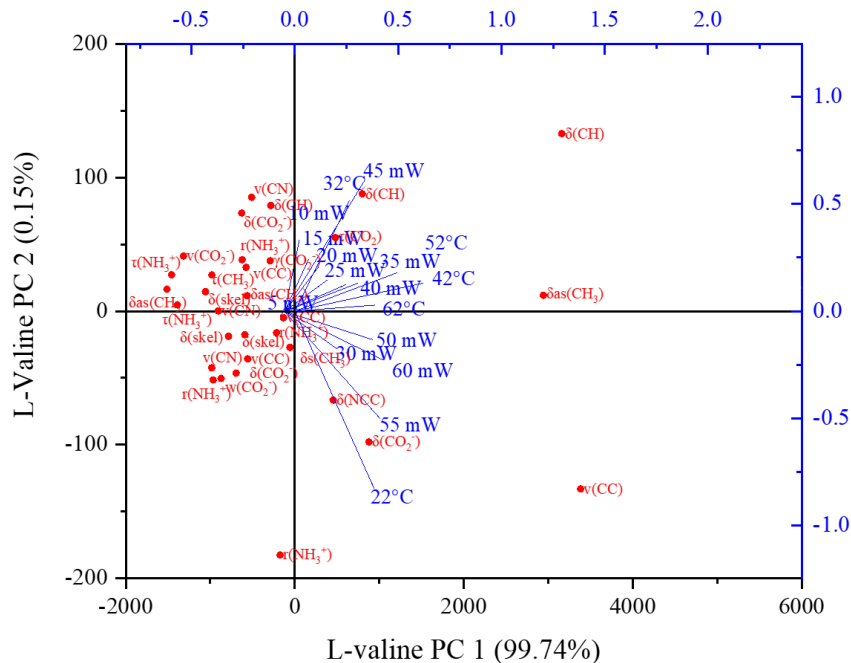
Figure 21 - L-valine biplot for the scores of vibrational mode observations and the loadings of the 60 experimental variables.

Figure 22 - L-isoleucine biplot for the scores of vibrational mode observations and the loadings of the 60 experimental variables.

3.5.4 Adaptive PCA for Individual Branched Chain Amino Acids

Adaptive PCA was executed for each amino acid where n oberservations is varied and $p = 60$ from the DOE described above. The first PC for each adaptive execution is plotted against its corresponding wavenumber (cm^{-1}) range and presented in a graph with the Raman spectra for identification of variance in vibrational modes. PC1 valleys are identified for each amino acid and matched to corresponding vibrational modes that appear in these regions as reported from previous studies. This adaptive PCA method was also executed for each blend and presented with a similar graph. Additionally, the peaks that appeared in the Raman spectra of the blends were matched to the vibrational mode assignments of the individual amino acids to determine wavenumber shifts as a function of composition.

Figure 23 - Adaptive PCA for individual amino acids: L-leucine, L-valine and L-isoleucine for all temperature values and all excitation laser power density shown by the dotted lines representing the PC1 values for each amino acid following the righthand y-axis as percent variance within the sample. Also shown is the correlating Raman spectra for each amino acid for all temperature values and all excitation laser power density.

Figure 23 displays a single Raman plot for each amino acid which was acquired by averaging the 60 scans over 50-1700 cm^{-1} since literature reports the majority of peaks appear in this region. These averaged Raman spectra are shown in conjunction with data from the adaptive PCA method that was executed across the entire DOE for each. The vibrational modes for each amino acid were identified using literature values [107] [108] [109]. In figure 23, L-leucine has five PC1 value valleys that present variance associated with vibrational modes at 589 cm^{-1} (73%), 725 cm^{-1} (75%)

, 1026 cm^{-1} (93%), 1250 cm^{-1} (94%), 1529 cm^{-1} (93%) which are associated with the $\omega(CO_2^-)$, $\delta(CO_2^-)$, $\nu(CC)$, $\tau(CH_2)$, and $\nu(CO_2^-)$ bonds that appear near these wavenumbers. L-valine has three PC1 valleys at 485 cm^{-1} (88%), 1155 cm^{-1} (96%), 1498 cm^{-1} (97%) that are associated with the $\tau(CH_3)$, $r(NH_3^+)$, and $\nu(CO_2^-)$ bonds that appear in these wavenumber regions. L-isoleucine has five PC1 valleys at 270 cm^{-1} (75%), 623 cm^{-1} (86%), 1226 cm^{-1} (97%), 1498 cm^{-1} (97%), and 16219 cm^{-1} (97%) that are associated with the $\tau(CH)$, $\omega(CO_2^-)$, $\tau(CH_2)$, $\nu(CO_2^-)$ and $\nu(CH_3)$ bonds that appear in these wavenumber regions.

3.4.5.1 Cross reference with Peak Analysis

Peak analyzation was executed for the vibrational modes assigned in each amino acid for all 60 scans using OriginPro batch peak analyzer. Resulting in the peak centers and heights being reported for all spectral scans. To analyze the peak shifts of the vibrational modes we have taken the two DOE points of the lowest and highest settings, which are 22°C, 5mW and 62°C, 60mW. The peak shifts will be presented from lowest setting to highest setting. An increase in wavenumber would indicate a compressive strain and a decrease in wavenumber would indicate a tensile strain. The greatest peak shifts for L-leucine were compression of $\delta(CO_2^-)$ 750.9-773.3 cm^{-1}, compression of $\nu(CC)$ 988.6-1012.4 cm^{-1} and tension of $\tau(CH_2)$ 1246.8-1217.1 cm^{-1}. The greatest peak shifts for L-valine were tension of $\tau(CH_3)$ 479.3-464.1cm^{-1}, and compression of $\nu(CO_2^-)$ 1555.9-1569.5 cm^{-1}. The greatest peak shifts for L-isoleucine were tension of $\tau(CH)$ with a range of 205.6-188.3 cm^{-1}, compression of $\tau(CH_2)$ 1234.5-1260.9 cm^{-1} and tension of $\nu(CH_3)$ 1639.7-1606.2 cm^{-1}. The PC valleys found in figure 23 and detailed above are center points of 100 cm^{-1} ranges used in the adaptive PCA. These ranges overlap with the shifts identified using the peak analyzation. The

values for all three amino acid peak shifts correlate directly with the PC1 valleys found using the adaptive PCA method.

3.5.5 Adaptive PCA for Blended Branched Chain Amino Acids

Raman spectra was collected on four unique blends of L-leucine, L-valine and L-isoleucine: 1:1:1, 2:1:1, 1:2:1, and 1:1:2 respectively. As with the individual samples, spectral data was collected at each of the five stage temperature settings and twelve laser power density settings. Figure 24 displays a single Raman plot for each amino acid blend acquired by averaging the 60 scans from the complete DOE for 50-1700 cm^{-1}. These averaged Raman data sets are shown in conjunction with data from the adaptive PCA method that was executed across the entire DOE for each. In figure 24, there are numerous peaks for each blend, most appearing in all the blends. PC1 (%) valleys are identified at 270 cm^{-1} for 1:1:1 (92%) and 1:2:1 (88%) which is $\tau(CH_3)$ in L-leucine, at 378 cm^{-1} for 1:1:1 (91%), 1:2:1 (83%), and 1:1:2 (94%) which is $\delta(CC)$ of L-isoleucine, at 485 cm$_{-1}$ for 2:1:1 (91%) and 1:1:2 (95%) which is $r(CO_2^-)$ of L-isoleucine, at 725 cm^{-1} for 1:1:1 (96%), 2:1:1 (95%), 1:2:1 (89%), 1:1:2 (97%) which is $\delta(CO_2^-)$, several between 927-1058 cm^{-1} from all four blends, at 1343 cm$_{-1}$ for 1:2:1 (93%) which is $\delta(CH)$ of L-valine, and at 1589 cm^{-1} or 1:1:1 (90%), 1:2:1 (88%), 1:1:2 (96%) which is $\nu(CO_2^-)$ of L-isoleucine.
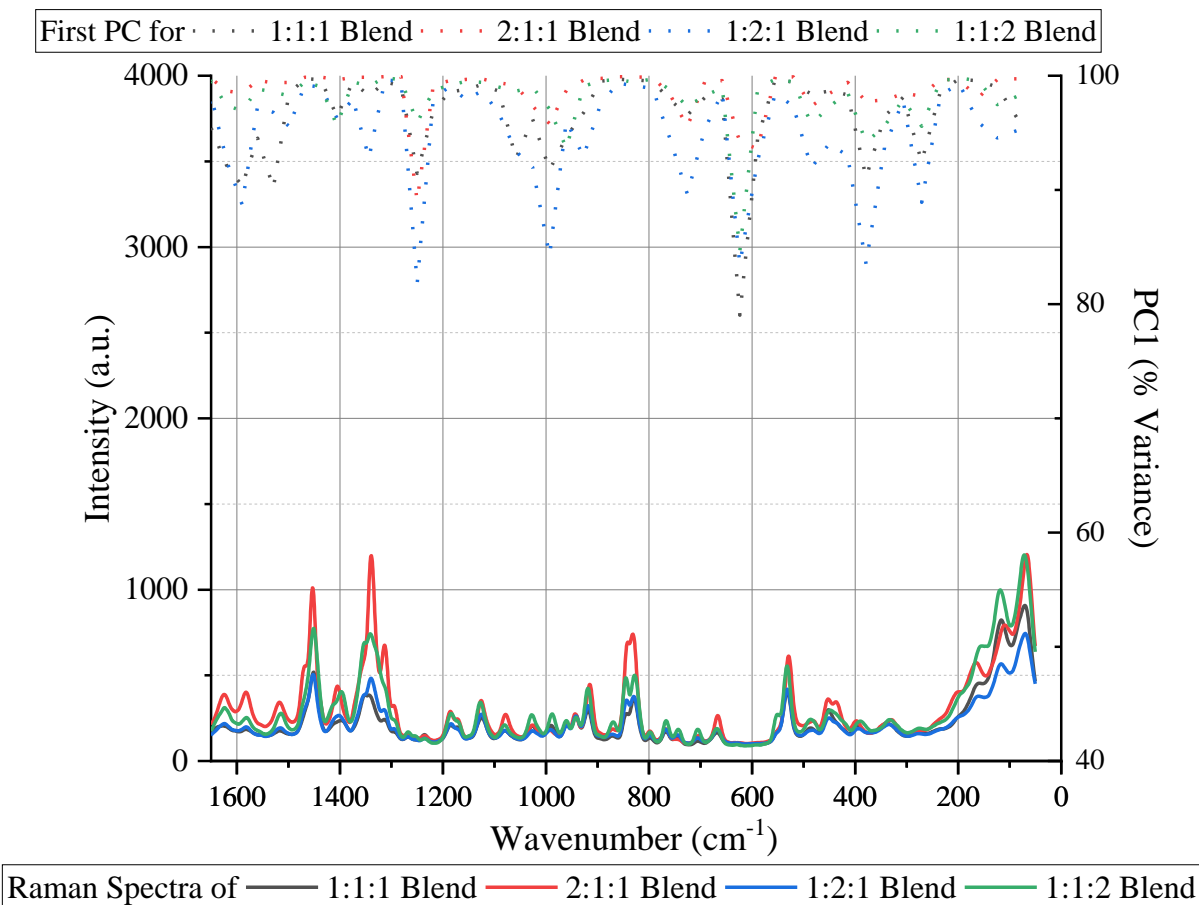
Figure 24 - Adaptive PCA for blended amino acid samples for all temperature values and all excitation laser power density shown by the dotted lines representing the PC1 values for each amino acid blend following the righthand y-axis as percent variance within the sample.

3.6 Energy Shift

The energy shift away from the original vibrational modes were calculated in order to analyze the strain induced in the blended samples due to compositional variations. The energy shift away from the excitation wavelength can be calculated using:

$$E = \frac{h \times c}{\lambda (nm)} \tag{25}$$

where h is Planks constant $= 4.135 \times 10^{-15}(eV \cdot s)$, and c is the speed of light $= 299{,}792 \times 10^{17}(nm/s)$, and $\lambda(nm)$ is the wavelength converted in the previous equation. Since the blended samples are comprised of varying concentrations of the individual amino acids then the peaks that appear in the Raman spectra of the blends can be matched with the assigned vibrational modes of the individual amino acids. Wavenumber shifts were determined and red shift (tensile) and blue shift (compressive) for each blend have been identified. The greatest tensile strain for the 1:1:1 blend is identified as $\nu(CH_2)$ of L-leucine at 2933.19 cm^{-1} and the greatest compressive strain of the 1:1:1 blend is $w(CO_2^-)$ of L-leucine at 664.23 cm^{-1}. The greatest tensile strain for the 2:1:1 blend is identified as $\delta(NCC)$ of L-isoleucine at 337.26 cm^{-1} and the greatest compressive strain for the 2:1:1 blend is $\delta_s(CH_3)$ of L-isoleucine at 1395.92 cm^{-1}. The greatest tensile strain for the 1:2:1 blend is identified as $\nu(CC)$ of L-leucine at 995.511 cm^{-1}, and the greatest compressive strain of the 1:2:1 blend is $\nu(CC)$ of L-valine at 1062.21 cm^{-1}. The greatest tensile strain for the 1:1:2 blend is identified as an unassigned peak from L-valine at 2774.03 cm^{-1} and $w(CO_2^-)$ of L-leucine at 664.23 cm^{-1}. Peaks that are not strained are identified in each blend as well. In the 1:1:1 blend these peaks are at 745.024 cm^{-1}, 1026.47 cm^{-1} and 1353.51 cm^{-1} which are $\delta(CO_2^-)$ of L-isoleucine, $\nu(CN)$ of L-leucine, and $\delta_s(CH_3)$ of L-isoleucine respectively. In the 2:1:1 blend these peaks are at 452.383 cm^{-1}, 749.626 cm^{-1}, and 841.704 cm^{-1} which are $\delta(CCC)$ of L-leucine, $w(CO_2^-)$ of L-valine, and $\gamma(CO_2^-)$ of L-leucine respectively. In the 1:2:1 blend these peaks are at 484.782, 1125.48 and 1294.03 cm^{-1} which are the $r(CO_2^-)$ of L-isoleucine, $r(NH_3^+)$ of L-leucine, and an unassigned mode in L-leucine respectively. In the 1:1:2 blend these peaks are at 845.01 cm^{-1}, 869.399 cm^{-1}, 1340.81 cm^{-1}, 1450.77 cm^{-1}, 1514.07 cm^{-1}, and 1624.44 cm^{-1} which are an unassigned mode in L-valine, $\nu(CC)$ of L-isoleucine, $\delta(CH)$ of L-leucine, $\delta_{as}(CH_3)$ of L-valine, an unassigned mode in L-leucine, and $\nu(CO_2^-)$ of L-leucine respectively.

3.7 Application of adaptive PCA to Monitoring Protein Phosphorylation

Chemical reaction monitoring using Raman spectroscopy has been achieved through periodic acquisition of data by measuring flowrates and/or the concentration of a rate limiting reagent, reactions can be analyzed as they proceed over time [110]. These techniques show promise in the detection of biomolecular reactions such as signal transduction mechanisms when there is a specific reaction indicator. We are interested in monitoring the ATP transition to ADP as a reaction indicator. Detection of ATP concentrations during the protein phosphorylation will be the indicating species in this research to monitor the reaction in real-time. Previous studies have shown it is difficult to decipher between ATP and ADP Raman spectra due to the high similarity of the vibrational modes from the two molecules [111] [112]. Utilizing the adaptive PCA described in this chapter we are able to apply this to Raman spectra of solid ATP and ADP samples to identify which vibrational modes result in the most variance between the two molecules.

Raman spectra was collected for ATP and ADP at room temperature and twelve different laser power densities ranging from 5-60 mW in 5 mW increments over the wavenumber range of 50-4000cm^{-1}. Figure 25 displays a single Raman spectral plot for ATP and ADP, which was acquired by averaging the scans for the wavenumber range of 50-1600 cm^{-1}. The phosphate bonds that are involved in the protein phosphorylation reaction appear in the 1000-1600 cm^{-1} wavenumber region. The adaptive PCA method identifies principal coefficients (PCs) for varying n observations in the $(n \times p)$ matrix. These PCs are plotted in conjunction with the averaged Raman spectra to correlate the variance with the wavenumber region
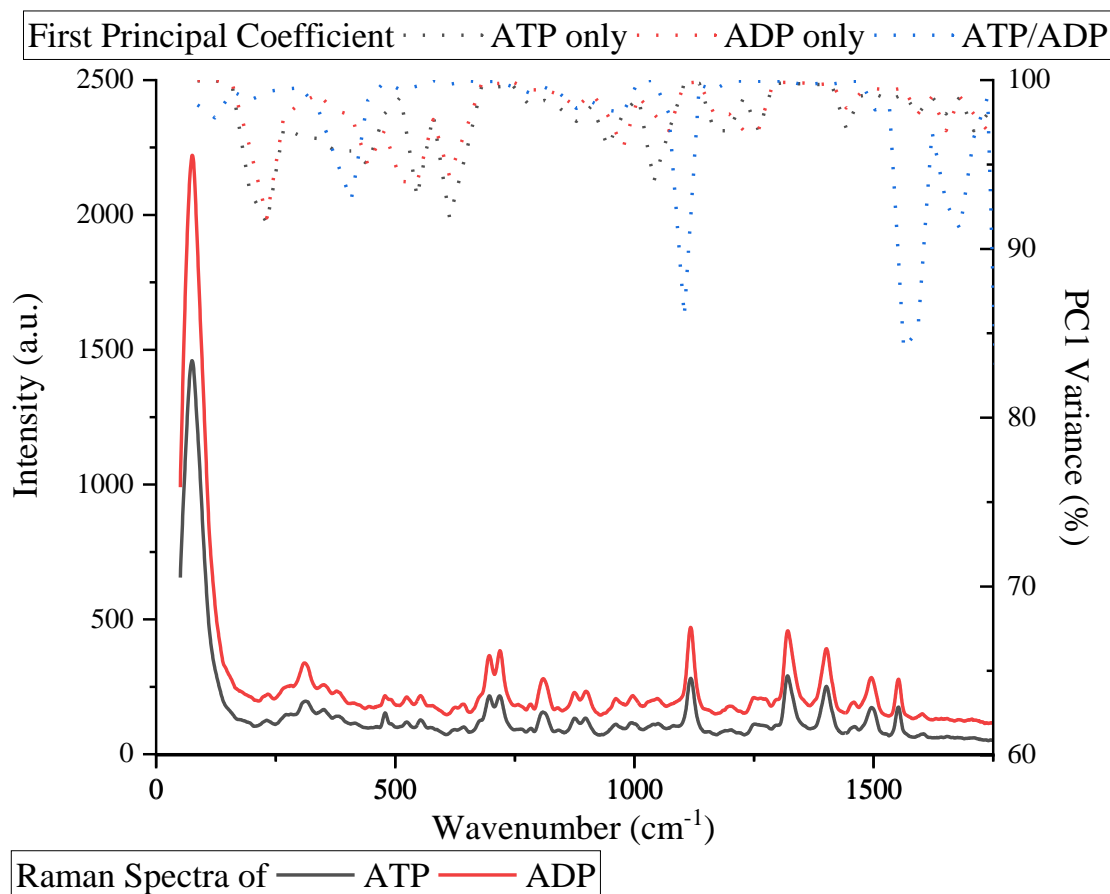
Figure 25 - Adaptive PCA for adenosine triphosphate and adenosine diphosphate shown by the dotted lines representing the PC1 values for each amino acid following the righthand y-axis as percent variance within the spectras. Also shown is the correlating Raman spectra for each averaged over the 12 laser power density settings collected at room temperature.

The PC1 valleys identified by the adaptive PCA method show that the peak at 1113 cm^{-1} (86%) and the peak at 1557 cm^{-1} (84%) are responsible for the most variance between ATP and ADP. To verify that this is due to the difference between the molecules, the adaptive PCA method was applied to the individual spectral data collected for ATP and ADP, which resulted in 99% and 98% PC1 values in these regions respectively. The PC1 valleys that appear between 100-700 cm^{-1} are believed to be a result of the background from instrumental effects that appear in this region.

3.8 Summary

In summary, the adaptive PCA method applied throughout this chapter identified the vibrational modes of three individual branched chain amino acids and blends comprised of varying rations of the three. This method was capable of extracting salient features in the Raman spectra as a results of varying laser power density, temperature and composition. The ability to extract these features of three structurally similar biomolecules encourages features extraction from ATP and ADP solutions. The application of this method to ATP and ADP samples shows promise that monitoring the concentration changes during the protein phosphorylation is achievable.

Chapter 4 – Microfluidic Reactor Design and Fabrication

This chapter will focus on the design and fabrication of the microfluidic reactors that will be used to monitor the protein phosphorylation reaction. One critical element of the reactor design criteria is the reactor compatibility with the confocal Raman spectrometer. Subsequently this will dictate the material, dimensions and assembly of the reactor. This chapter will present current fabrication techniques and preliminary data for material selection, the specific features of the Raman spectrometer that influence the reactor design and assembly. Solution tests were performed on the reactor and are also included in this chapter. These results are Raman spectra of adenosine triphosphate at varying molar concentrations in both static and fluid conditions.

4.1 Current Fabrication Techniques

Microfabrication techniques have evolved over the last 20 years to adapt for automation and control, lower costs, and high throughput of microfluidic devices. Photolithography and micromachining techniques emerged in the early 90s as one of the more popular techniques to fabricate microfluidic devices [113]. Photolithography techniques are traditional semiconductor processes used to etch precise patterns in metal or oxide substrates using a photomask transferred by UV irradiation through a photoresist layer over the substrate material to be etched [114]. As an example of this technology applied to biochemical reactions, Wilding et al. used this technique to create 40 - 80μm deep microchambers to perform polymerase chain reaction on rectangular silicon chips with Pyrex caps [115]. Another research team, Schena et al. created a microarray by etching glass to investigate gene expression [116]. Photolithography was used for years on numerous applications but continuing research was limited due to the complexity of the etching process and lengthy fabrication time. Photolithography requires the use of cleanroom facilities and several

types of equipment requiring days to weeks for complete fabrication. These drawbacks led researchers to begin using polymers for fabrication of microfluidic devices in the late 90's [117]. Duffy et al. used poly(dimethysiloxane) (PDMS) to create a network of microfluidic channels with widths < 20 μm in less than 24hr total fabrication time [117]. Furthermore, researchers used PDMS etching, referred to as soft lithography, to create microfluidic devices for biology and biochemistry [118]. These applications include separation systems for DNA fragments [119], biochemical assays [120], and cell cycle and growth systems [121]. The use of soft lithography has enabled researchers to pair microfluidics with online measurements using ultraviolet/visible spectroscopy [78], infrared spectroscopy [79], atomic force microscopy [80], electrochemical detection [81], and Raman spectroscopy probes [82]. Substantial research efforts, reviewed in chapter 2, have shown that microfluidic devices are suitable to facilitate biochemical reaction monitoring. Based on the research to date, a microfluidic reactor that is compatible with our confocal Raman spectrometer was designed.

4.2 Raman Spectroscopy Features

Raman spectroscopy is a characterization technique that relies on the inelastic scattering of photons to determine vibrational modes of molecules. The vibrational modes of molecules provide detailed information on chemical structure, conformation, phase and morphology and crystallinity. Several features of Raman spectroscopy make it optimal for use with biological applications detailed in the next few sections.

4.2.1 Nondestructive and non-contact

Raman is considered a nondestructive interrogation technique making it ideal for use with biochemical applications since it does not alter the sample during acquisition. In addition to being non-destructive, it is also a non-contact technique, meaning it does not come in contact or interfere with the sample under interrogation. These two features combined, allow Raman spectroscopy to analyze chemical reactions within a vessel without perturbing the reaction. This leads to Raman spectroscopy being an ideal instrument to perform *in situ* analysis. Specifically, for this research, Raman allows for real-time monitoring of a biochemical reaction in a microfluidic device without the need to be fully integrated into the microfluidic device structure. It also allows for this research to be advanced towards intracellular interrogation of biochemical reactions. This is crucial, as the results from this work on extracellular protein phosphorylation can be directly implemented to develop intracellular protein phosphorylation detection.

4.2.2 No Interference from Water

In addition, Raman spectroscopy is advantageous to use in biological applications due to the lack of interference by water during spectral acquisition. Water molecules have permanent dipole moments that do not contribute to Raman scattering. Since biochemical reactions occur in aqueous solutions this makes Raman a valuable technique to use for this research.

4.2.3 3D Spatial Resolution

Confocal Raman spectroscopy can provide full spatial resolution in three dimensions. The collection volume can be changed along the surface of the sample in the x-axis, y-axis as well as the z-axis of a sample. Meaning confocal Raman can interrogate below the surface, changing the

collection volume of sample. This is useful for analysis of layered samples such as polymer laminates, thin samples on a substrate such as cells on a microscope slide, or samples held within optically transparent containers, such as liquids in a glass vial. For this research, the ability to focus the collection volume below a glass container wall without interference on the sample solution is essential.

4.2.4 Acquisition Speed

Raman spectroscopy data collection speed is an additional aspect supporting this research. Raman spectroscopy is a very fast technique, requiring seconds to collect high quality spectral data. Since biochemical reactions occur quickly, the acquisition speed of Raman spectroscopy allows us to collect spectra at a rate that allows for the capture of these reactions in real-time. The software with our specific instrument also allows for setup of rapid repeated spectral acquisition.

4.2.5 Spectral Data on Aq. Solution

As a starting point, Raman spectroscopy was performed on liquid samples placed on a glass slide in open air. The following figure 26 shows the Raman spectra for solid L-serine, water and a 0.1 M aq. L-serine solution that was acquired in open air on a glass slide surface. The solutions are not contained in a vial, so that there is no medium (other than air) between the samples and the objective. The collection parameters were set at a laser setting of $6.68 \times 10^4 \ W/cm^2$, 10 second acquisition time, confocal hole setting at 500 μm, through the 10x objective.
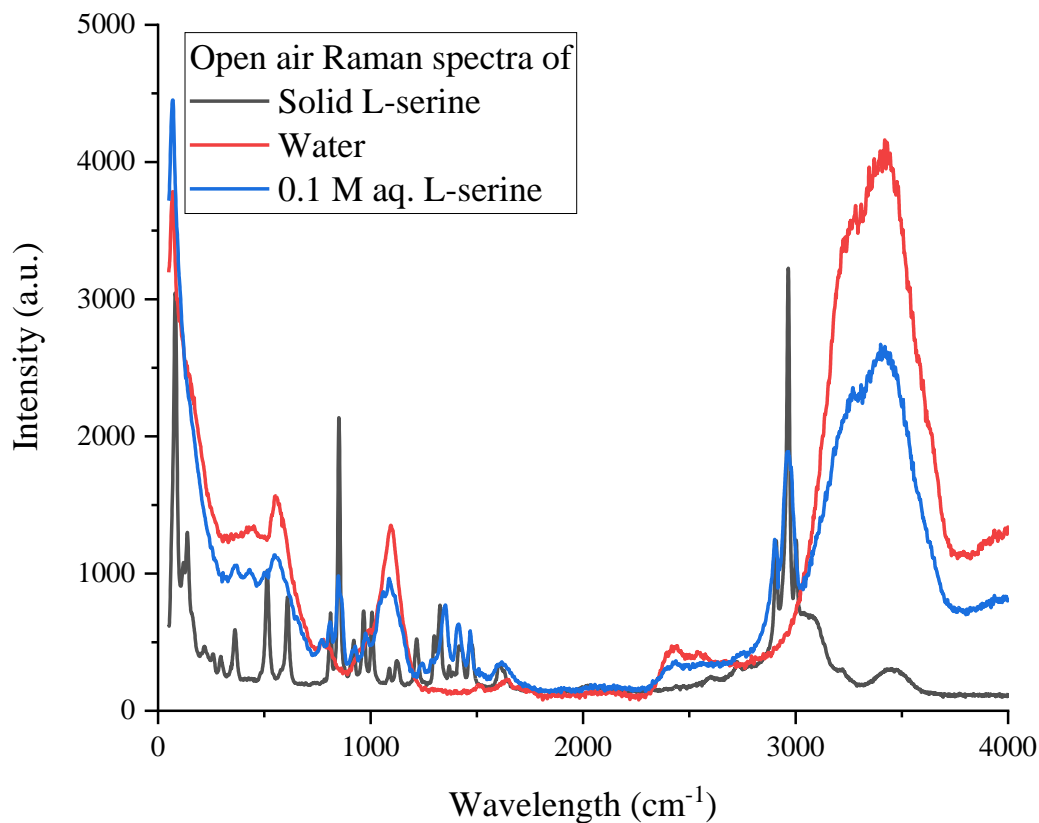
Figure 26 -Raman spectra of solid L-serine, water and a 0.1 M aq, L-serine solution collected in open air environment.

The vibrational modes that can be identified from the aq. L-serine solution are the lattice vibrations below 200 cm^{-1}, ν(CC) at 851 cm^{-1}, δ(CH) at1356 cm^{-1}, 1419 cm^{-1}, and 1471 cm^{-1} and ν(CH$_x$) at 2903 cm^{-1} and 2969 cm^{-1}. Not all of the peaks appear for a few reasons. First, the crystallography of the solid sample contributes to long range order resulting in vibrational modes for all the bonds present in solid L-serine. Second, the molecule count for a pure solid sample within the laser collection area (1 µm) is greater than the molecule count present in a 0.1 M solution within the same collection area. The peaks that contribute to the spectra of water are decreased in the aq.

solution spectra for the same reason, less water molecules are present in the 0.1 M solution than the pure water sample.

4.3 Prefabricated PDMS Microfluidic Device

Since research in the field of microfluidics have shown success with PDMS microfluidics, we decided to design and purchase prefabricated devices from uFluidix. The reactor was designed to have a channel width of 300 μm, depth of 30 μm and a length of 47 mm. These dimensions were based on literature values of common microfluidic devices, while maintaining a width/depth ration of 10 dictated by the manufacturer. The reported values for the reaction rate of PKA phosphorylation of Casein, $k = 0.400 \ s^{-1}$, was also used to calculate the reactor length with the dimensions of the width and length set and a flowrate of 0.05 ml/min. Figure 27 illustrates the design of the prefabricated microfluidic device purchased. This device was intentionally designed to fit on a standard glass slide that would fit on the sample stage of the Raman spectrometer. Typically, when analyzing liquid samples, the 10x objective on the microscope of the Raman is used. This allows for a large stand-off distance between the sample solution and the physical end of the objective lens. Figure 28 shows how the Raman microscope can interrogate the PDMS microfluidic device (not to scale).

(Top View)

PDMS Length is 5 cm

Channel
Dimensions:
300μm Width,
30μm Depth
47 mm Length

PDMS width
is 2 cm

Ports are punched to fit 0.03" tubing

Standard Microscope Slide

PDMS Thickness is 3 mm

(Side View)
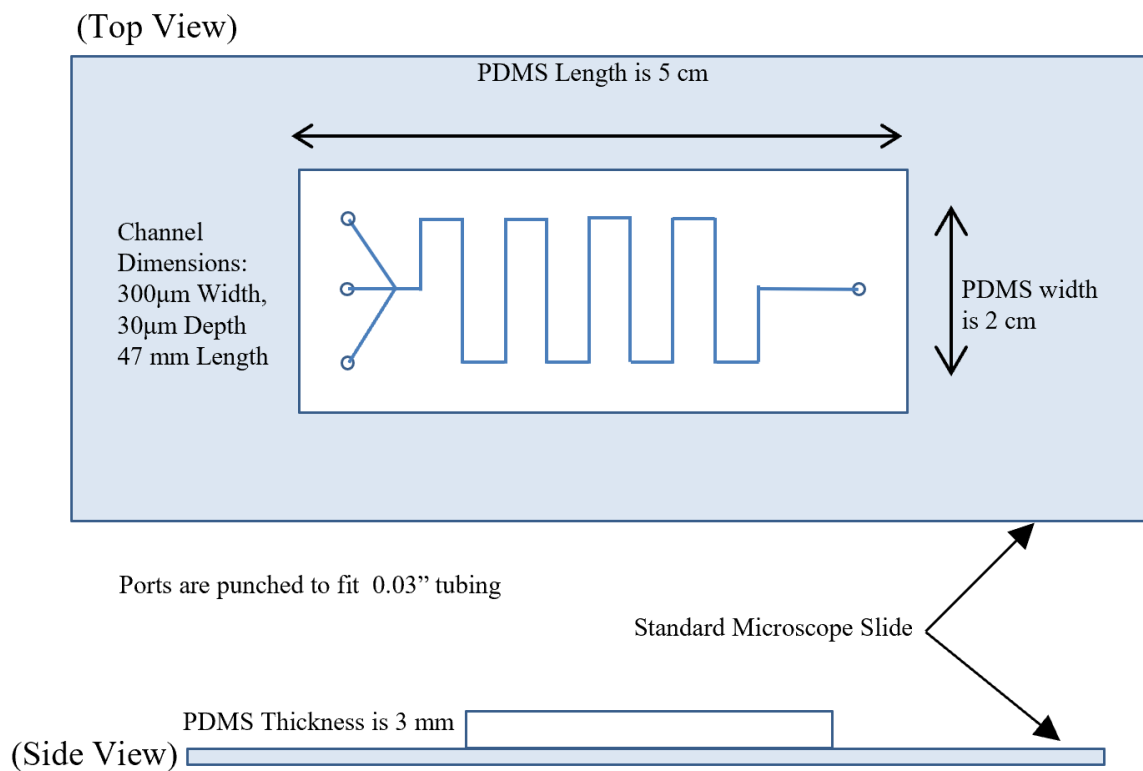
Figure 27 – Prefabricated PDMS microfluidic device design in white, bonded to a standard glass slide in blue.

Confocal
Microscope

Inlet

Outlet

Glass Slide

Channel
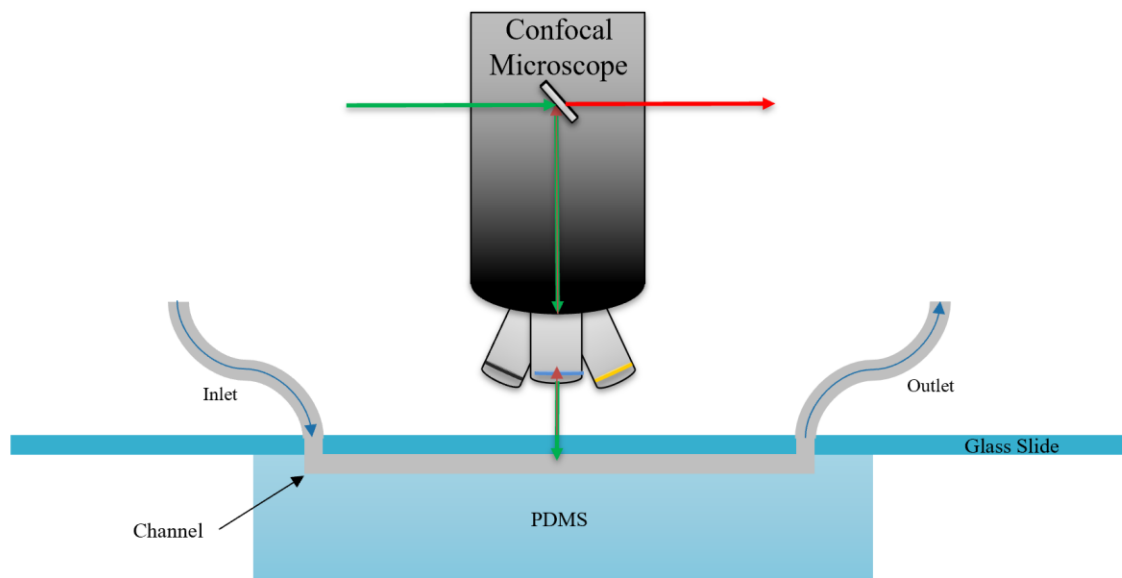
PDMS

Figure 28 – Raman spectroscopy collection set-up on prefabricated PDMS microfluidic device.

4.3.1 Compatibility between Raman spectroscopy and PDMS microfluidic reactor.

Since the microfluidic device for this research must be compatible with the Raman spectrometer, characterization of the PDMS device was performed first. Raman spectra was collected at six different interfaces on the prefabricated device, labeled in figure 29.
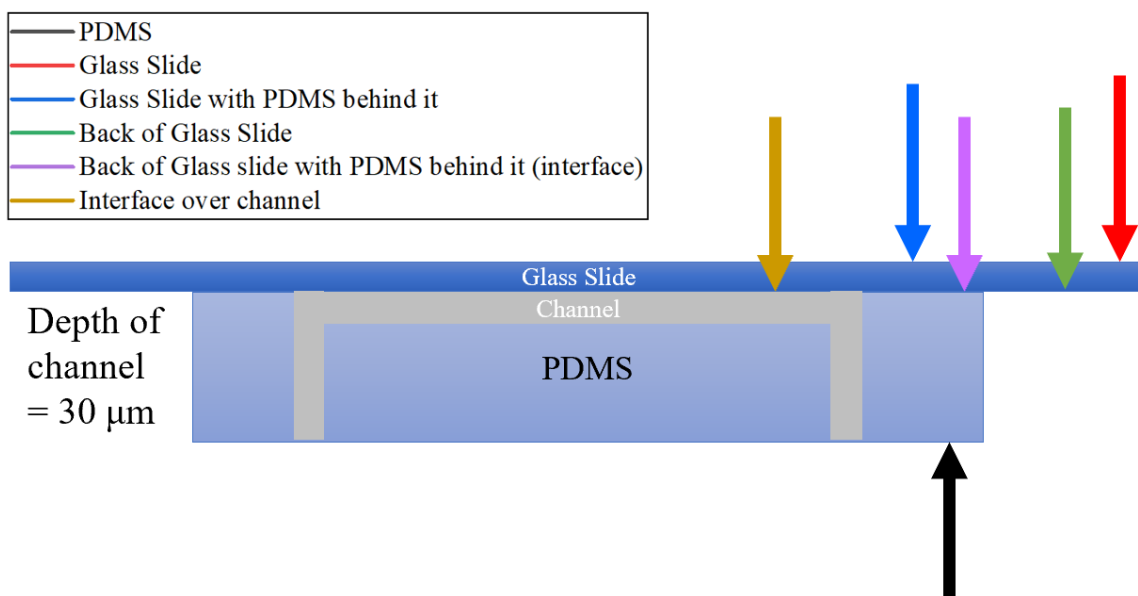
Figure 29 – Raman spectra on six interfaces of a prefabricated PMDS microfluidic channel: (black) PMDS surface, (red) glass slide surface, (blue) glass slide with PDMS behind it, (green) back of glass slide, (purple) back of glass slide with PDMS behind it, (orange) interface over channel.

The Raman spectra for the top surface and bottom surface of the glass slide are shown in figure 30. The color of the spectral data lines correlate with the color of the arrows and legend of figure 29. Both of these show low spectral response from the glass. The bottom surface of the glass slide shows a lower response than the top surface, this may be because the measurement was taken through the thickness of the glass slide, decreasing the response received through the objective into the spectrometer.
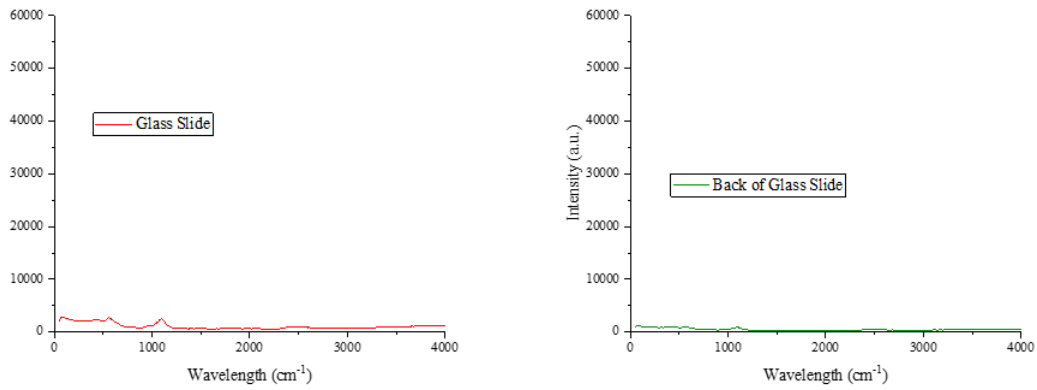
Figure 30 – Raman spectra on the interfaces of a prefabricated PMDS microfluidic channel, (red, left) glass slide surface, (green, right) back of glass slide.
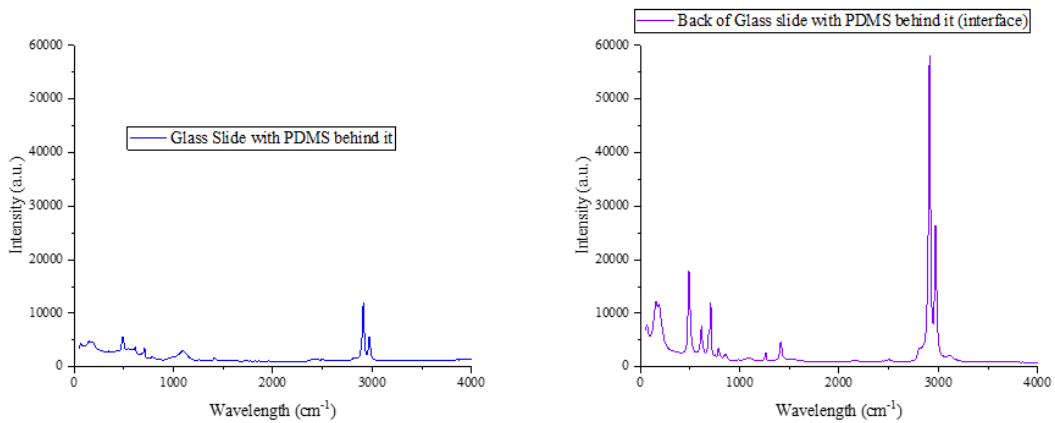
Figure 31 - Raman spectra on six interfaces of a prefabricated PMDS microfluidic channel, (blue, left) glass slide with PDMS behind it, (purple, right) back of glass slide with PDMS behind it.
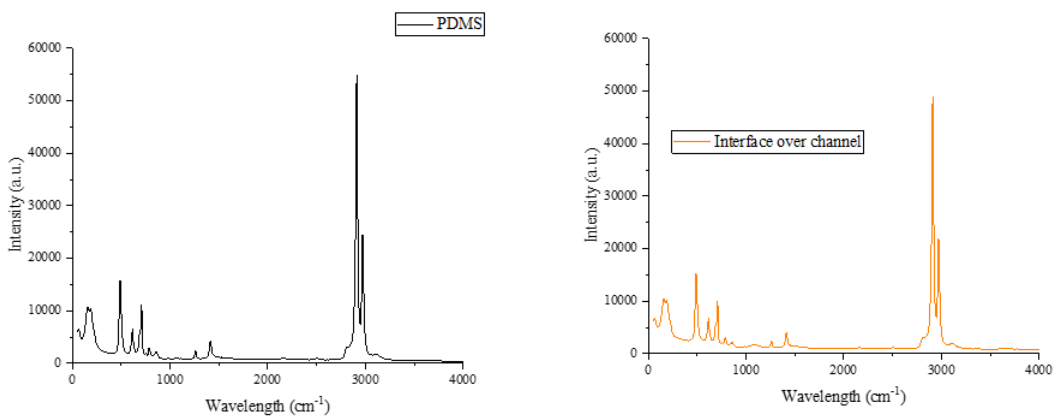
Figure 32 - Raman spectra on six interfaces of a prefabricated PMDS microfluidic channel: (black, left) PMDS surface, (orange, right) interface over channel.

The second set of measurements were taken on the surface of the glass slide that has the PDMS material behind it and the bottom of the glass slide that also has the PDMS material behind it shown in figure 31. The spectra acquired on the top with PDMS behind it shows vibrational modes that appear in PDMS. The spectra acquired on the bottom of the glass slide with PDMS behind it shows a very high response from PDMS. This measurement point is the interface between the glass slide and the PDMS so it makes sense that the PDMS spectral response is higher.

The Raman spectra for the surface of the PDMS is shown on the left of figure 32. This measurement was taken by flipping the device 180° to take the measurement directly on the surface of the PDMS material. The spectral response of the PDMS surface here is lower than the response seen in figure 32 right. The most important surface to acquire Raman spectra on is the back of the glass slide over the channel with the PDMS behind it, shown in figure 32 (right). This will be the collection point to measure Raman spectra of the solutions inside the channel. By looking at the spectra in figure 32 right, it is apparent that the PDMS still has a significant spectral response, even with the depth of the channel behind 30 μm.

The Raman spectra of the prefabricated PMDS microfluidic reactor indicates that the PDMS spectra will mask any potential signal from the reagent solutions inside the channel. The spectra shown in purple yields the highest response from PDMS, even though it's through the glass slide. This indicates the glass slide amplifies the response since the spectra in purple is higher than the spectra on the PDMS surface shown in black. The spectra shown in orange would be the collection location during a reaction, and even with the 30 μm depth of the channel, the PDMS response is still high and would mask the solution spectra. To verify this Raman spectra was collected on water and 0.1 M aq. L-serine solution inside the

channel. These measurements were acquired at the same parameters as the open air solutions. The laser setting of $6.68 \times 10^4\ W/cm^2$, 10 second acquisition time, confocal hole setting at 500 μm, through the 10x objective were used. The collection point on the chamber is shown above in figure 28, with the glass slide the material between the solutions and the objective lens.
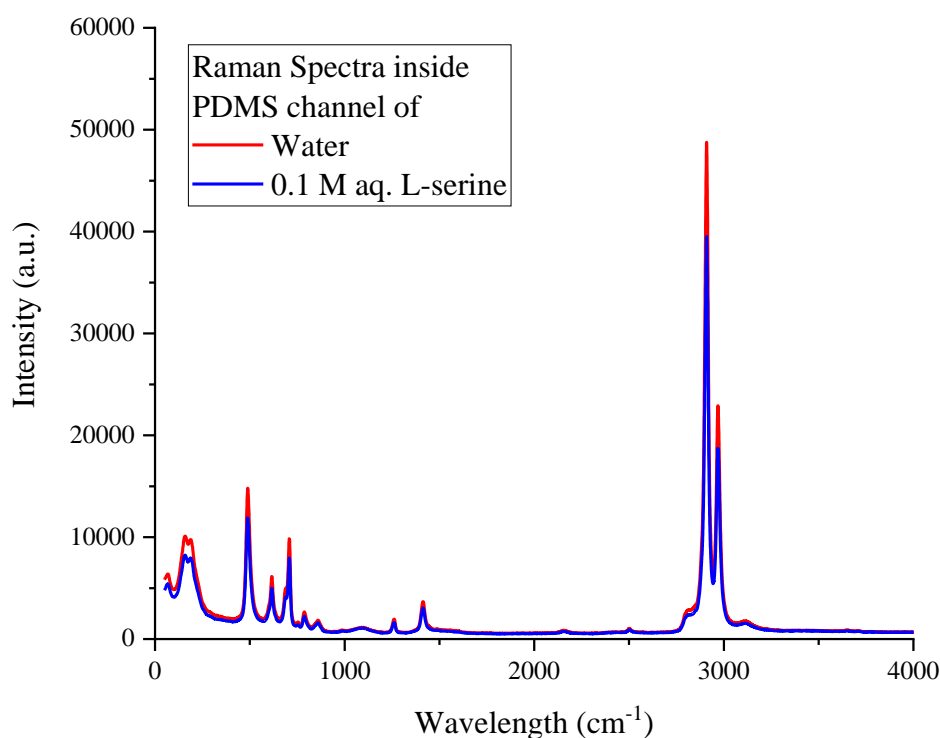
Figure 33 -Raman spectra of water and 0.1 M aq. L-serine solution inside prefabricated PDMS microfluidic device.

The Raman spectra for water and 0.1 M aq. L-serine solution shown in figure 33 appear to show only characteristic peaks of PDMS. The PDMS response completely masks the vibrational modes of both solutions as predicted. Since it was apparent that PDMS would mask all response from the solutions as a backing material we investigated collecting

Raman spectra through the inlet port to see if there is spectral contribution from the side walls of the channel.
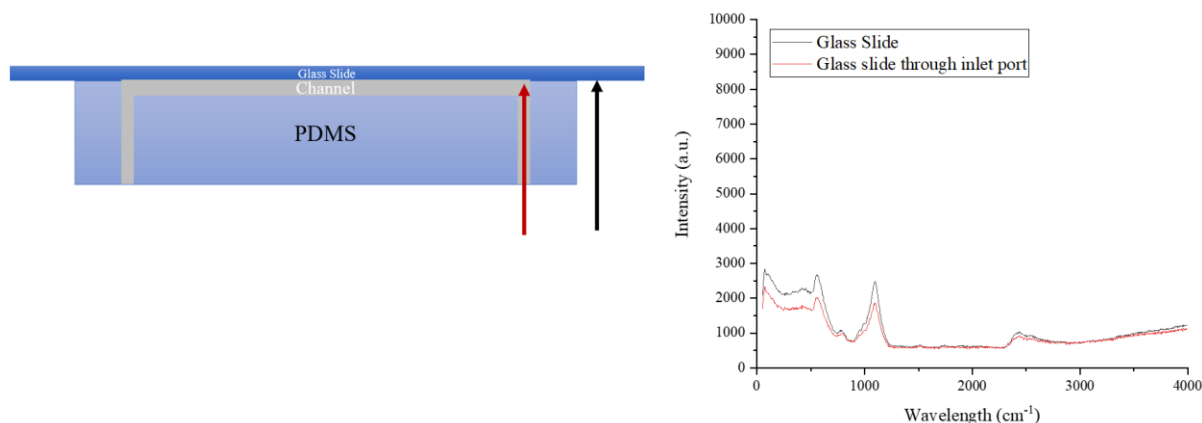
Figure 34 - Raman spectra through an inlet port on the prefabricated PDMS microfluidic channel shown in red compared to the Raman spectra of the glass slide surface shown in black.

 The Raman spectra shown in figure 34 compares the response through the inlet port (red) and the glass slide surface (black). These measurements were taken by focusing on the glass slide with nothing behind it and by focusing through the inlet port to the glass slide surface inside the channel. These two spectra lines indicate that the side walls of the PDMS channel do not contribute to the Raman spectra since they are nearly identical. This allows for the channel walls of the microfluidic device to be fabricated out of any material, theoretically, leading to the use of alternative polymers for the channel side walls as long as the top and bottom of the reactor are optically transparent to the Raman spectrometer. This led to the concept of creating the microfluidic channel side walls and placing them between two glass slides, instead of a single glass slide like the prefabricated PDMS device above.

The initial design concept consisted of a polymer sheet/slide with the channel side walls cut-out or stamped out in the desired pattern. PDMS is still an option for this concept. Although PDMS is an inexpensive material, and the fabrication time is significantly decreased over photolithography of silicon and glass, previous researchers have identified that barriers still exist [122]. In a review paper by Au et al, three drawbacks were identified with PDMS microfluidics: cumbersome user interfaces, related to soft lithography, that lead to leaks in the devices [123], automation that requires highly skilled operators [124], and slow molding time [122]. The fabrication of a PDMS cut-out sheet/slide that is bonded on two sides to glass plates would require extensive time and the use of cleanroom facilities. To overcome this, we turned to 3D printing for the channel side walls.

4.4 3D Printing Microfluidic Devices

The term "3D printing" refers to a process of building a three-dimensional object by successively adding material layer by layer. This process is a subset of additive manufacturing. 3D printing technology emerged in 1974 and use has expanded rapidly. There are several types of 3D printing processes that have been developed. The processes that are applicable to microfluidics include selective laser sintering (SLS), fused deposition modelling (FDM), and photopolymer inkjet printing.

In SLS, the object to be printed is created by a laser beam that heats a thin layer of powder to the desired pattern across the build area. This layer is then covered by a thin layer of the powder and the laser beam repeats the molding of the powder in the designer pattern of the next layer. This process is repeated until the 3D object is complete. The object must be retrieved from the excess powder. SLS is capable of sintering polymer or metal powders.

In order for this process to be applied to microfluidic fabrication, removal of the powder through the channels has become a challenge for researchers. This aspect limits the channel dimensions, since the channels must be flushed after fabrication. Capel et al reported that a diameter of 3 mm was necessary in order for the microfluidic tube to be flushed properly without clogging [125]. Another drawback to this process is the variability in particle size of powder used, which can lead to defects in the object.

Fused deposition modelling is the process of extrusion. A heated thermoplastic is pushed through a die of a desired cross-section to form each layer on the build plate. This technique can utilize a number of different thermoplastics such as acrylonitrile butadiene styrene (ABS), poly(lactic acid) (PLA), polycarbonate, polyamide and polystyrene. The structure of the object is comprised of layers of these materials and differs in strength than that of bulk solid injection molded object. These defects can lead to compressive stress fractures in the object [126]. An alternative method was developed to mitigate this by printing the object in a heated atmosphere, but this feature is an expensive feature. The resolution of FDM printing poses a challenge for researchers that want to print microfluidic devices. Typical nozzle diameters are between 0.3 – 1.0 mm with the stepper motor increments matching the diameter of the specific printer. FDM is only capable of creating a minimum of 300 μm channels.

The 3D printing process with a higher resolution is photopolymer inkjet printing. In this process, a UV light cures a photopolymer in the desired pattern for each layer. Since each layer is cured by a UV light, the diameter of the UV beam dictates the resolution of the printer and can achieve 16 μm layers. The drawback to this aspect is that this process can

require more time to print the object than with SLS and FDM printing. Currently, this process offers a wide range of materials with different indices of refraction, stiffness, strength, and transparency. Given the wide range of materials offered, researchers have been able to 3D print anatomically correct models for orthopaedic [127], intracranial aneurysm [128], and cardiac [129] surgery prep. Researchers have reported using photopolymer inkjet printing for completely enclosed channel widths of 500 μm and were able to flush the channels of any remaining material post-fabrication [130]. For these reasons, photopolymer inkjet printing was chosen to 3D print the polymer sheet with channel sections. The following sections detail each component of the microfluidic device including the 3D printing section, top and bottom slides, assembly process and the integration of tubing for inlet/outlet flow of solutions.

4.5 Microfluidic Reactor Design

The microfluidic reactor described in this chapter is assembled from a 3D printed device that is placed between a cover slip and a standard glass slide with microdrilled holes. The sections below will detail each component

4.5.1 Reactor side walls

The side walls were designed using AutoDesk Inventor and printed using a Stratasys Objet Eden260VS PolyJet printer. This 3D printer uses UV light to cure the proprietary liquid photopolymer in 16 μm layers to print the uploaded design. The support material used by this printer is also soluble in ethanol making it easier to remove the printed part from the

printer stage. The resolution of this printer enables this device to print on the micron scale for these reactors.
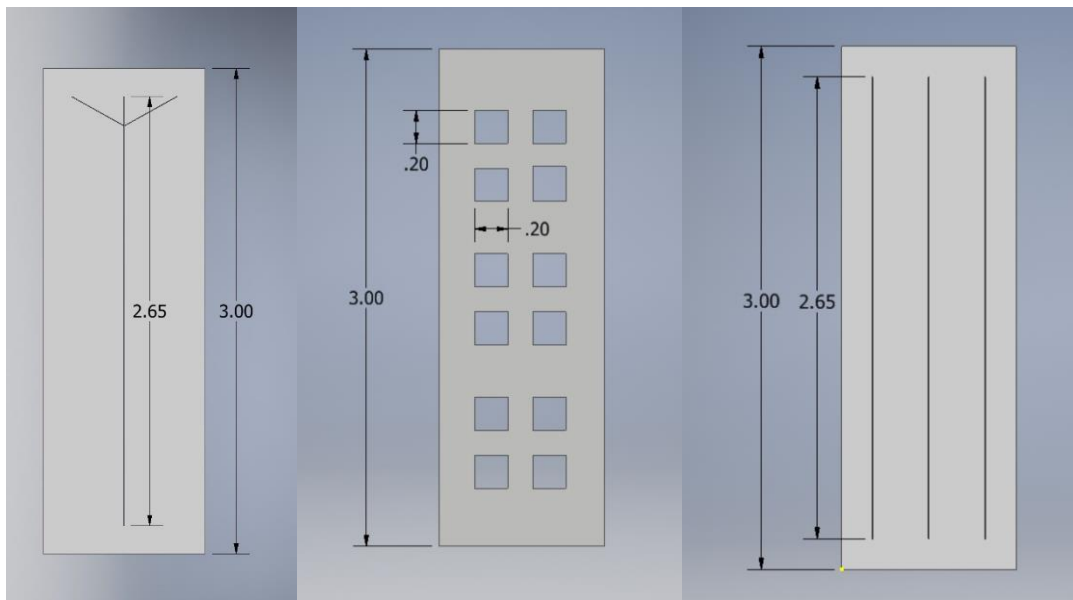
Figure 35 – Microfluidic chamber side wall designs with dimensions in inches.

4.5.2 Reactor top and bottom

The piece of the reactor that is above the collection window of the Raman spectrometer will be referred to as the 'top' and the piece that is below the collection window of the spectrometer will be referred to as the 'bottom'. The top of the reactor is a cover slip that is 75x25x0.08 mm. A cover slip was chosen with a thickness of 0.08 mm to minimize the spectral contribution from the glass. The bottom of the reactor is a standard glass slide with dimensions 75x25x1 mm. A coverslip was not chosen for the bottom because a 1mm thickness was necessary for the inlet tubing to be secured in placed eliminating potential leaking or rupture. The bottom slide was microdrilled to for inlet and outlet ports. Three ports were drilled on one end and a single outlet port was drilled on the opposite end. Each port had a diameter of 0.76 mm and a depth equal to the thickness of the slide or 1 mm.

Figure 36 – Port placement of microdrilled holes in standard glass slide for the 'bottom' of the microfluidic reactor assembly.

4.5.3 Sample loading

The solutions of the reagents are loaded into the reactor through Tygon tubing with an outer diameter of 0.76 mm and inner diameter of 0.25 mm inner diameter. This size Tygon tubing fits over 30g needle. Syringes of 1 ml volume and 4 mm diameter are the solution reservoirs. Figure 37 illustrates the complete assembly of the reactor side walls, top and bottom and syringe attachment using Tygon tubing.
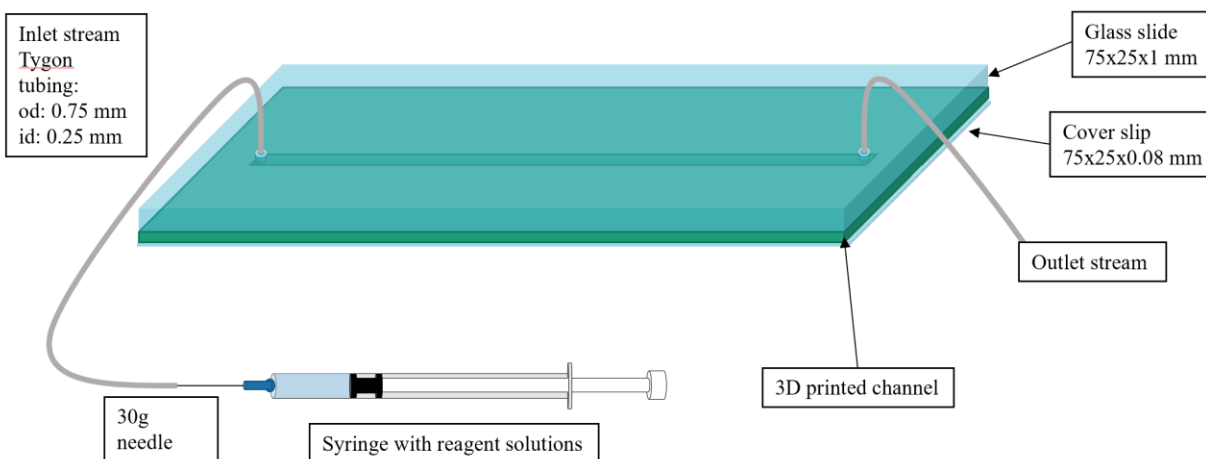
Figure 37 – Experimental setup of 3D printed channel between a microdrilled glass slide and a cover slip, inlet port connected to syringe by Tygon tubing and outlet port to waste.

4.5.4 Flow control

Fluid flow is controlled using a syringe pump. The syringe pump is capable of flow control of 0.001 μL/hr to 147 mL/min. The syringe operates by moving a mechanical bar placed behind the syringe plunger. The speed of the mechanical arm is automatically calculated by the pump based on the syringe diameter, needle size, and volume. These parameters are manually selected by the user.

4.6 Raman spectroscopy of ATP Solutions

Raman spectra was collected on aq. ATP solutions at varying molar concentrations of 0.1 M – 1.0 M at room temperature over the wavenumber range of 50 - 4000 cm^{-1}. The experimental parameters were set to a laser power density of $6.68 \times 10^4 \ W/cm^2$, 10 second acquisition time, the confocal hole setting at 500 μm, through the 10x objective. Figure 38 displays the spectral data. The phosphate bonds that are involved in the protein phosphorylation reaction appear in the 1000-1600 cm^{-1} wavenumber region. The Raman spectra in figure 388 shows an increase in intensity as the molar concentrations of ATP in the solution is increase. This is due to there being more ATP molecules present in the laser beam collection diameter (1 μm). It was pertinent to understand the effects of fluid flow on the Raman spectra in order to account for this under transient conditions. To do this, we loaded the microfluidic chamber with 50 mg/ml of ATP and collected measurements on the static solution. We then initiated fluid flow of the same ATP solution into the reactor at 0.005 ml/min and collected spectra for 15 s. Fluid flow was halted and static measurements were collected. This procedure was repeated for flowrates of 0.010, 0.015, 0.020 and 0.025 ml/min, taking static measurements between each change in flowrate. These results are shown in figure 39. This graph displays the height changes of the phosphate bonds of

ATP that appear in the 1000 - 1600 cm^{-1} range. The height of the peaks is directly related to the

flowrate which is indicative of the addition of energy related to fluid flow. The standard deviation

of the static measurements is < 0.8 cm^{-1}.
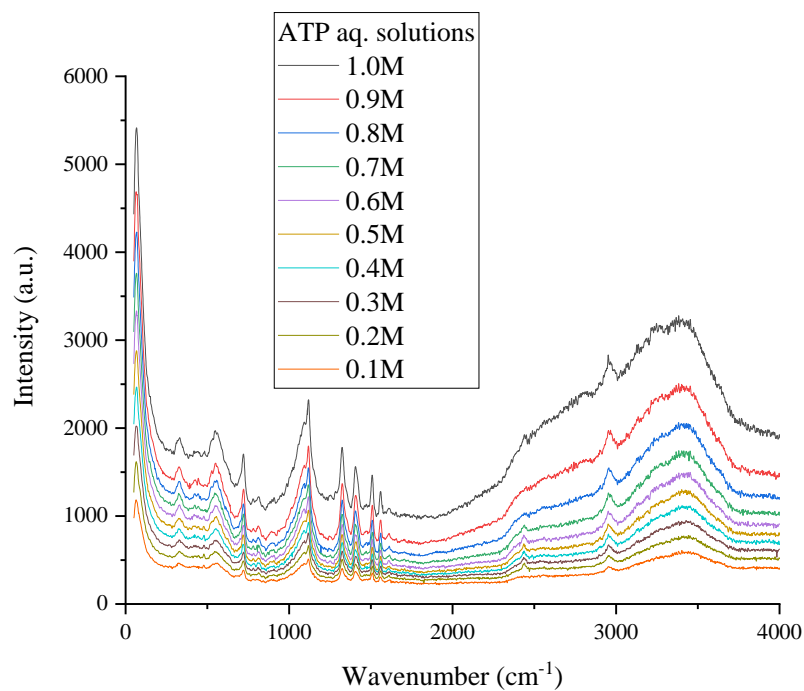
Figure 38 – Raman spectra of aq. ATP solutions at varying molar concentrations of 0.1 M – 1.0 M at room temperature over the wavenumber range of 50 - 4000 cm^{-1}.
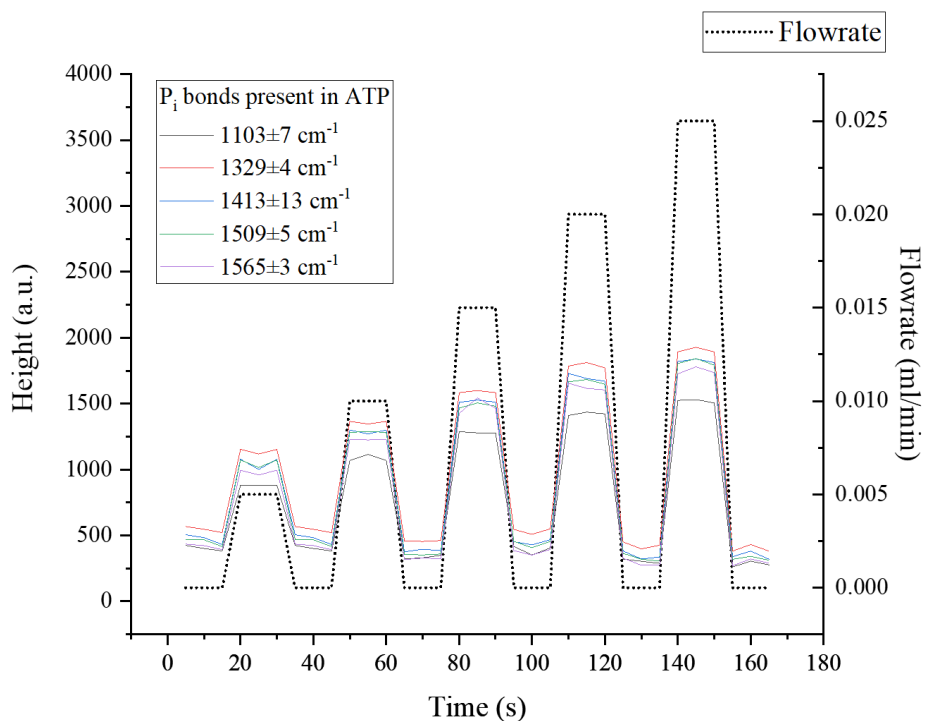
Figure 39 - Raman spectroscopic peak height of the phosphate bonds from ATP that appear between 1000 - 1600 cm^{-1} as a function of flowrate over time.

4.7 Summary

The design and fabrication of a microfluidic reactor by assembling 3D printed side walls between a glass slide with microdrilled holes and a coverslip were successfully integrated with the confocal Raman spectrometer. Cleary, the PO_x vibrational modes associated with the transition from ATP to ADP are detectable and variance through the adaptive PCA method is attained. This reactor design allows for rapid prototyping of numerous side wall designs that can be tailored to specific reactions. In the following chapter, a reactor is designed specifically for the monitoring of the ATP to ADP transition and the protein phosphorylation reaction.

Chapter 5 – ATP Detection

This chapter will describe the process and method of monitoring the phosphorylation of Casein by protein kinase A (PKA) and adenosine triphosphate (ATP). This will include the microfluidic device designed to facilitate this reaction, preliminary results using the device and the reaction results and verification results. Based on the reaction mechanism described in chapter 2, the chemical transition of adenosine triphosphate (ATP) to adenosine diphosphate (ADP) will be the reaction indicating species. The concentration of ATP and ADP will be monitoring during the reaction progression. The microfluidic device in this chapter allows for the monitoring of the reaction progression by detecting the concentration changes on ATP and ADP. The device was designed to mimic the transfer of the phosphate group from ATP to ADP by allowing for mass transfer in the chamber of each molecule. The chamber is designed to be pre-loaded with an ATP solution and have one inlet of an ADP solution and one outlet of the mixture. Raman spectroscopy is performed of the chamber as the ADP enters. In order to identify the spectral shift from ATP to ADP, principal component analysis must be performed on the individual spectral data and the solution data. This data is presented in this chapter and the analysis shows promise towards the detection of the phosphate transfer during the phosphorylation reaction. Concluding this chapter are two data sets of Raman spectra acquired during the phosphorylation reaction. This data aligns with the results acquired in the mass transfer analysis. The reaction products were verified using isoelectric focusing.

5.1 Adenosine Triphosphate

Adenosine triphosphate (ATP), an organic compound present in all living organisms, providing cellular energy often referred to as the "currency" of energy in cells. ATP is connected to numerous

biochemical mechanisms such as metabolic regulation [131], embryo development [132], RNA synthesis [133], and most commonly, protein phosphorylation [134]. Detection of ATP concentrations intracellularly may aid in detecting biochemical reactions linked to health and disease, further, real-time monitoring of biochemical mechanisms will aid in prognosis of diseases. The quantitative detection of ATP and ADP ratios is applicable to our research for the monitoring of protein phosphorylation as well as an indicator of cell necrosis, apoptosis and viability [111].

5.1.1 Detection of Adenosine Triphosphate

Previous studies have shown it is difficult to decipher between ATP and ADP Raman spectra due to the high similarity of the vibrational modes from the two molecules [111] [112]. Structurally, the only difference between the two molecules is the γ-phosphate in ATP shown in figure 40. Researchers began using surface-enhanced Raman scattering to study ATP using silver electrodes [112]. A more recent study used solutions of varying ratios of ATP and ADP dried on Au/cicada wing
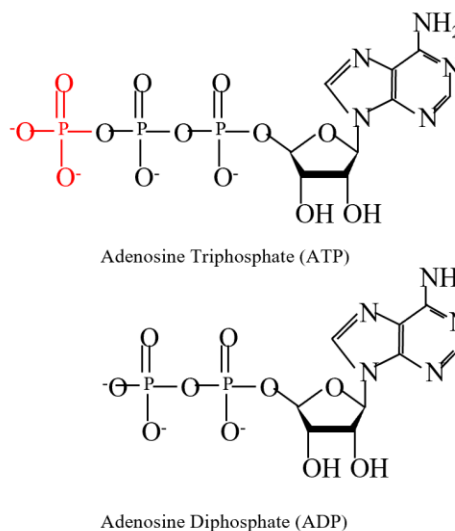
Figure 40 – Chemical structure of adenosine triphosphate and adenosine diphosphate

substrates to determine the difference in vibrational modes, with significant difference reported for the γ-phosphate mode. This study is, however, limited to solid dried samples on the substrates which is not yet translatable to cell detection. Several more studies have used various enhancements such as Au nanostar@Raman label@SiO2 core-shell nanoparticle [135], Au/Al$_2$O$_3$ nanocomposites [136] and SiO2@Au@Ag nanoparticles [137] to detect ATP. The above approaches are focused on changing the environmental the ATP is in to enhance detection instead

of modifying the analysis of data acquired. These studies also only focus on static measurements of varying concentrations on the enhancements and not transient ATP to ADP that you would see during a biochemical reaction.

5.2 Design of ATP Reactor

As described in chapter 2, the reaction progression of this mechanism involves the transfer of a phosphate group from adenosine triphosphate to the substrate protein, resulting in adenosine diphosphate and the phosphorylated substrate protein. In a reaction involving the transfer of a phosphate group from ATP to a substrate protein, the concentration of ATP will decrease during conversion to ADP. To simulate this, a microfluidic chamber with one ADP inlet to a preloaded ATP chamber and one outlet was designed to monitor the concentration changes of both molecules simultaneously. Figure 41 illustrates the 3D printed device and direction of flow during mass balance experiments and reaction experiments. This device is 3D printed and assembled according to the process described in chapter 4.
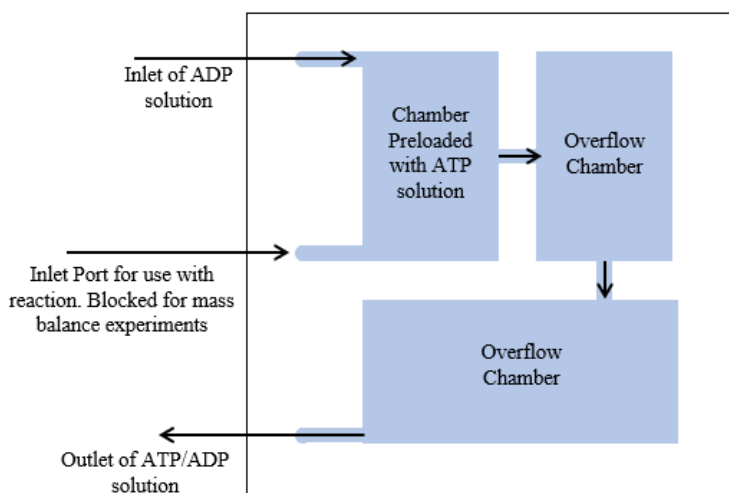
Figure 41 – Microfluidic device used for ATP/ADP concentration monitoring during mass balance experiments and reaction experiments.
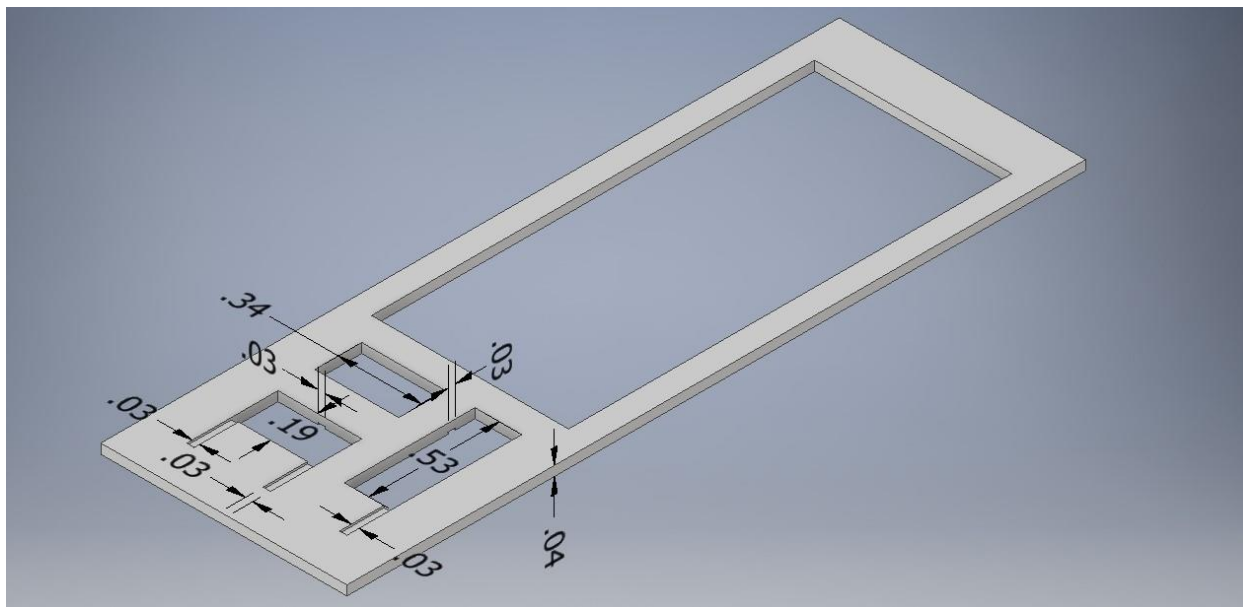
Figure 42 – Autocad Inventor illustration of 3D printable device for the mass transfer and reaction experiments with dimensions in inches.

Initially, this chamber serves as a mass balance to extract spectral changes as a function of solution concentration without the complex biochemical reaction occurring. This was done to simplify the problem of distinguishing between ATP and ADP only. Figure 43 shows the mass balance on the chamber.
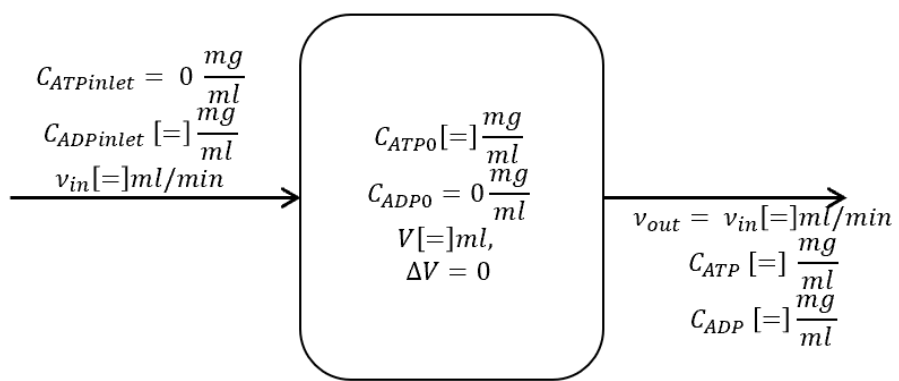
Figure 43 – Mass balance variables of ATP and ADP in the microfluidic chamber.

To derive the mass balance for each species we will refer to ATP as species A and ADP as species B. Both will follow the basic mass balance equation on any species, i, as follows:

$$\frac{di}{dt} = (rate\ in\ of\ i) - (rate\ out\ of\ i) = (C_i v_{in}) - \left(\frac{i(t)}{V} v_{out}\right) \tag{26}$$

where t is time (s), C_i is the concentration of species i (mg/ml) in the inlet stream and v_{in} and v_{out} are the inlet and outlet flowrates (ml/s) , V is the volume of the reactor (ml) and $i(t)$ is the mass of i in the reactor and exit stream (mg). It is assumed that the inlet and outlet flowrates are equal since the volume of the reactor is constant. It is also assumed that the composition of the exit stream is equal to composition of the chamber contents. Since the chamber will be preloaded with a solution of ATP (C_{ATP0}) and there will be no ATP flowing into the chamber then we can substitute $C_i = 0$ and arrive at,

$$\frac{dA}{dt} = 0 - \frac{A(t)v}{V} \tag{27}$$

Rearranging,

$$\frac{1}{A} dA = -\frac{v}{V} dt \tag{28}$$

Integrating,

$$\int \frac{1}{A} dA = \int -\frac{v}{V} dt \tag{29}$$

$$lnA = -\frac{v}{V} t + c \tag{30}$$

Applying boundary conditions $t = 0$ then $A(0) = C_{ATP0}$

$$\ln(C_{ATP0}) = 0 + c \tag{31}$$

Substituting into previous equation,

$$lnA = -\frac{v}{V} t + \ln(C_{ATP0}) \tag{32}$$

Raising to the exponential we arrive at

$$e^{\ln (A)} = e^{-\frac{v}{V}t + \ln(C_{ATP0})} \quad\quad (33)$$

Simplifying to

$$A = C_{ATP0}e^{-\frac{v}{V}t} \quad\quad (34)$$

Finally arriving at,

$$C_{ATP} = C_{ATP0}e^{-t\frac{v}{V}} \quad\quad (35)$$

To solve for the concentration of ADP we can write equation 26 as

$$\frac{dB}{dt} = C_{Bin}v - \frac{B(t)}{V}v \quad\quad (36)$$

Rearranging,

$$\frac{dB}{dt} + \frac{v}{V}B(t) = C_{Bin}v \quad\quad (37)$$

Multiplying by the integrating factor of $e^{t\frac{v}{V}}$, followed by applying the product rule,

$$\frac{dB}{dt}e^{t\frac{v}{V}} + B\left(\frac{e^{t\frac{v}{V}}}{\frac{V}{v}}\right) = C_{Bin}ve^{t\frac{v}{V}} \quad\quad (38)$$

Reducing to,

$$d\left(Be^{t\frac{v}{V}}\right) = C_{Bin}ve^{t\frac{v}{V}}dt \quad\quad (39)$$

Integrating both sides,

$$\int d\left(Be^{t\frac{v}{V}}\right) = \int C_{Bin}ve^{t\frac{v}{V}}dt \quad\quad (40)$$

We arrive at,

$$Be^{t\frac{v}{V}} = C_{Bin}v\left(\frac{V}{v}\right)e^{-t\frac{v}{V}} + c \quad\quad (41)$$

Simplifying,

$$B = C_{Bin}V + ce^{-t\frac{v}{V}} \qquad (42)$$

Applying boundary conditions at $t = 0$ then $B(0) = C_{ADP0} = 0$,

$$0 = C_{Bin}V + ce^{-t\frac{v}{V}} = C_{Bin}V + c \qquad (43)$$

Such that,

$$c = -C_{Bin}V \qquad (44)$$

Substituting back into equation 42 we arrive at

$$B = C_{Bin}V - C_{Bin}Ve^{-t\frac{v}{V}} \qquad (45)$$

Finally arriving at,

$$C_{ADP} = C_{ADPinlet}V - C_{ADPinlet}Ve^{-t\frac{v}{V}} \qquad (46)$$

where C_{ATP0} is the initial concentration of ATP in the chamber (mg/ml), v is the volumetric flowrate (ml/min), V is the volume of the reactor and $C_{ADPinlet}$ is the concentration of ADP in the inlet stream (mg/ml). The concentration of ATP at time, t, in the chamber is dependent on the flowrate of the inlet stream and the initial concentration of ATP charged to the chamber. The concentration of ADP at time, t, is dependent on the flowrate of the inlet stream and concentration of ADP into the reactor. Theoretical concentration profiles for ATP in the reactor are shown in figure 44. The concentration curves shown are for varying flow rates and an initial concentration, $C_{ATP0} = 10 \ mg/ml$. The concentration of ATP decreases faster when the inlet flow rate is increased. The concentration profile of ADP is shown in figure 45 for varying inlet concentrations at $v_{in} = v_{out} = 0.005 \ ml/min$ and $C_{ADP0} = 0 \ mg/ml$ inside the chamber. The concentration of ADP inside the reactor increases in the chamber faster at higher inlet concentrations. The concentration of ADP does not rise above 2 mg/ml during the time frame plotted for an inlet concentration of 50 mg/ml which is the maximum concentration achievable due to the solubility

limit of ADP in water. This is because the outlet flow also contains ADP, therefore the retention

of ADP in the chamber will not be as quick as the dilution of ATP in the chamber.
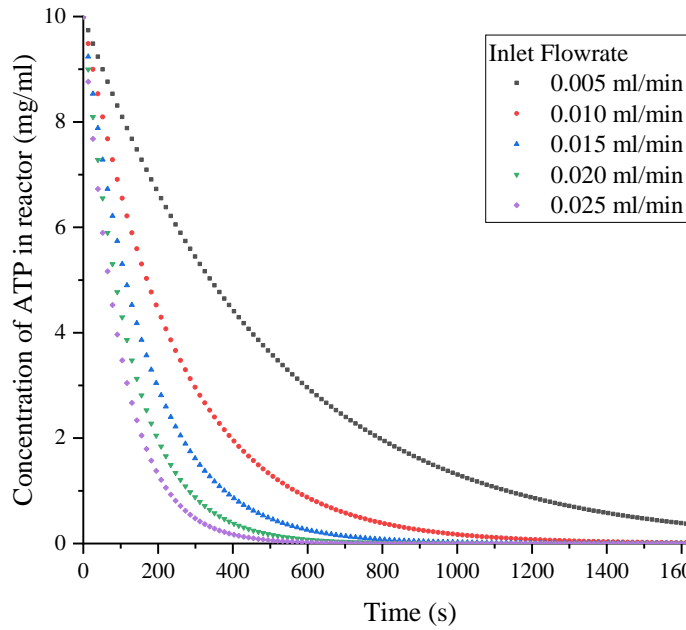
Figure 44 - ATP concentration in the chamber as a function of inlet flowrate according to equation 1.
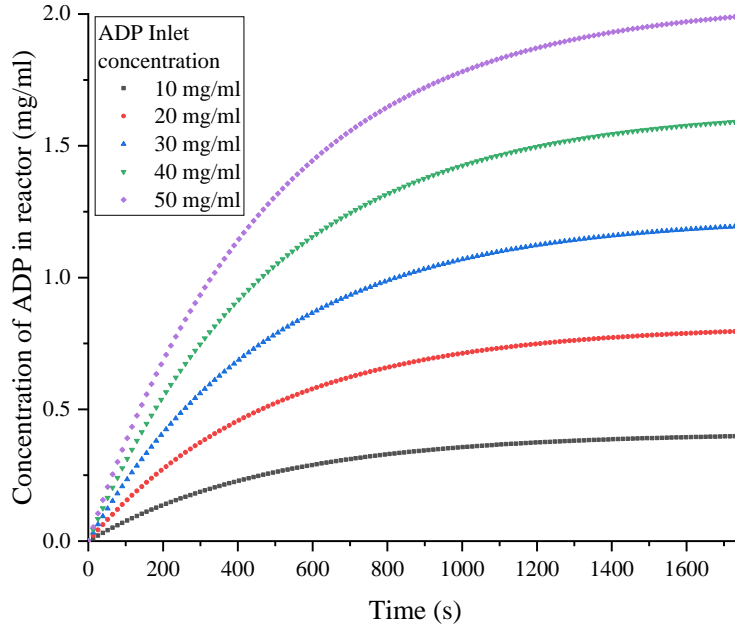
Figure 45 – ADP concentration in the reactor as a function of the inlet concentration of ADP according to equation 2.

5.3 Data Collection and Analysis

For the experiments conducted in this chapter, the Raman spectrometer laser power density was set to $6.05 \, x10^4$ W/cm^2, and a 1s acquisition time. The adaptive principal component analysis described in chapter 3 was executed on the spectral data to extract data deciphering between ATP and ADP in the solutions. Figure 46 represents the complete experimental setup.
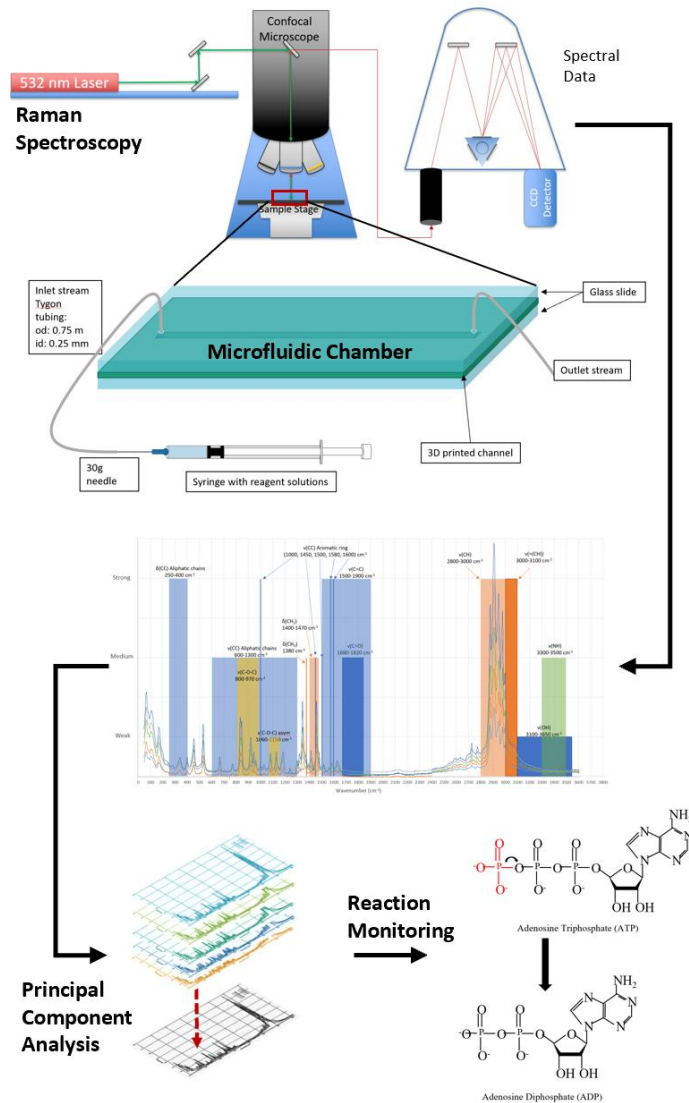
Figure 46 – Complete experimental setup for the monitoring of biochemical reactions in real-time.

5.4 Static solutions

Five solutions of varying ATP and ADP concentrations were mixed using water for cell culture in the following weight % ratios: 50:0, 40:10, 30:20, 20:30, 10:40, respectively. Raman spectra was collected at room temperature over the wavenumber range of 50-4000 cm^{-1} and repeated 3 times. Figure 47 shows the spectral response between 1000-1600 cm^{-1}

since this is the region identified pin chapter 3, that was responsible for the majority of the variance between the two molecules.
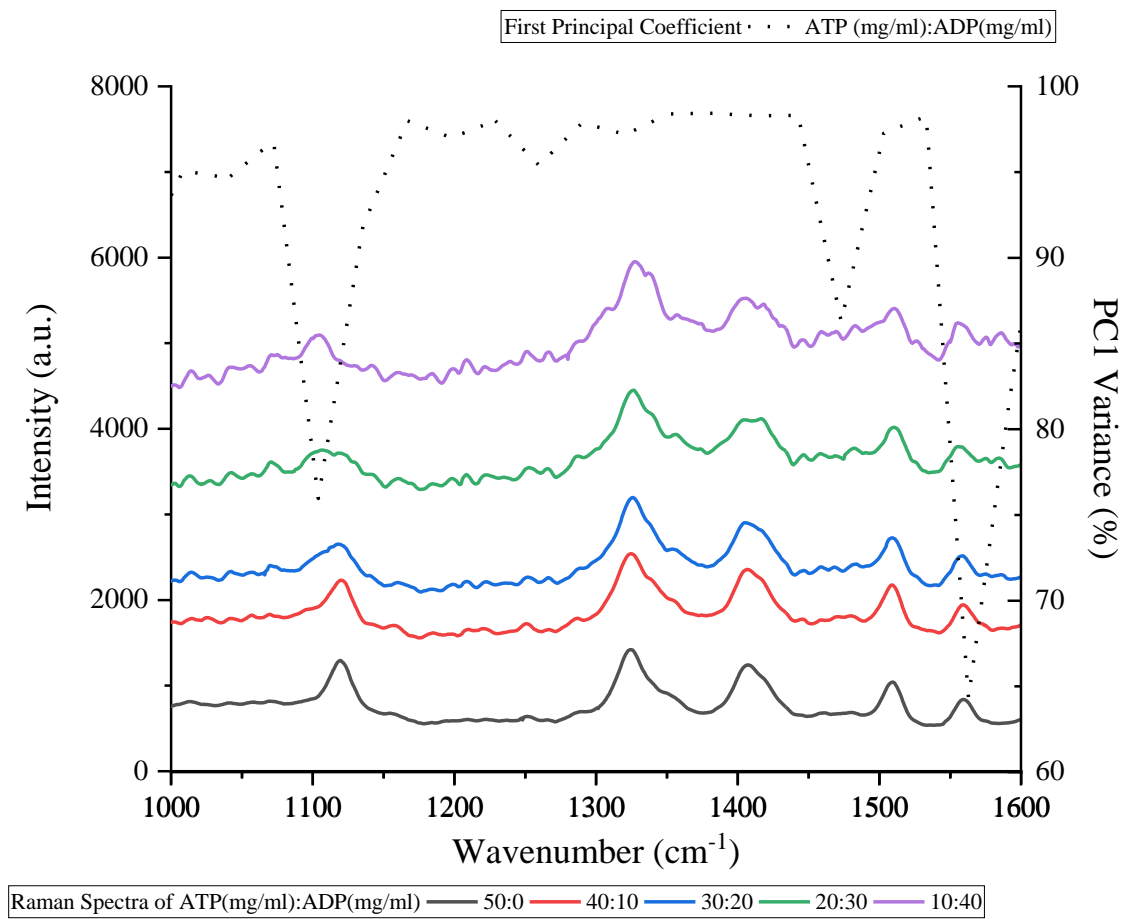
Figure 47 - Raman spectra on static solutions of known varying concentrations of ATP:ADP shown in conjunction with the adaptive PCA identifying the PC1 valleys for the wavenumber range between 1000-1600 cm^{-1} where the PO$_x$ vibrational modes appear.

The PC1 values over this region behave similarly to the solid individual samples, with the same two peaks at 1113 cm^{-1} (76%) and 1557 cm^{-1} (64%) having the most variance. The variance seen between the two molecules in solution was greater than the variance seen between the molecules in solid form. This greater variance is due to the random disorder of the molecules in solution compared to the high crystalline order of the solid molecules.

Peak integration was performed on the peaks in this region using OriginPro. The changes in height followed a linear increase as the concentration of ADP increased.
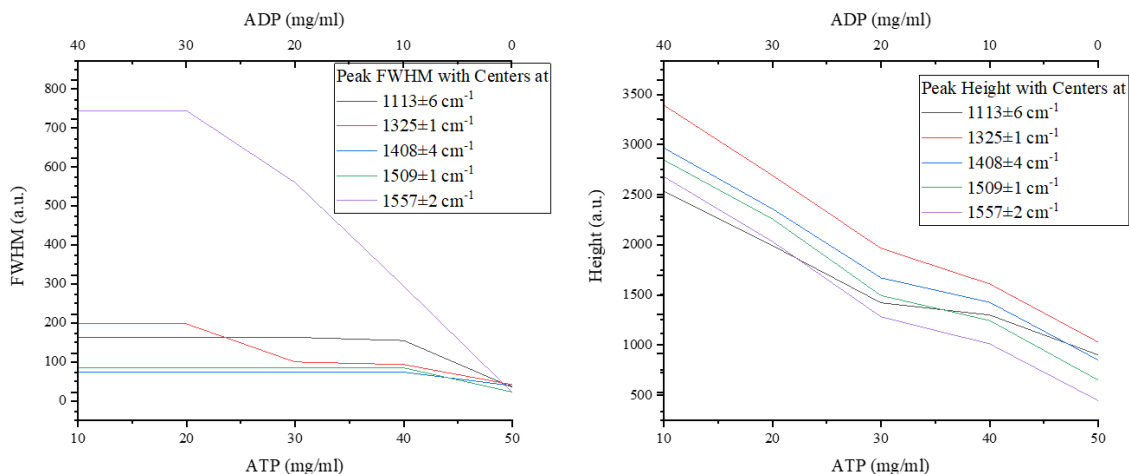
Figure 48 – (left) Full width half max for each peak appearing in the wavenumber region between 1000-1600 cm^{-1} of static solutions of varying ATP:ADP concentrations. (right) Height of each peak appearing in the wavenumber region between 1000-1600 cm^{-1} of static solutions of varying ATP:ADP concentrations.

Figure 48 shows the full width half max (left) and height (right) results from the integration which shows that the behaviour of the peak at 1557 cm^{-1} is dissimilar from the others as the ADP concentration increases. This type of trend from the adaptive PCA shows promising detection of ATP to ADP transition that would occur during a reaction. The changes in height followed a linear decrease as the concentration of ATP increased.

5.5 Transient Solutions

To investigate the effects of fluid flow on the spectral data, we loaded the chamber with 50 mg/ml ATP, collected static measurements, and then initiated fluid flow at 0.005 ml/min of cell culture grade water into the chamber. We collected Raman spectra continuously with scans taking 5s to complete until the ATP phosphate peaks were indistinguishable from the

water baseline in the 1000-1600 cm^{-1} region. At this time, fluid flow was then halted and another static measurement was collected to compare to the original static measurement for this experiment. This is displayed in figure 49.
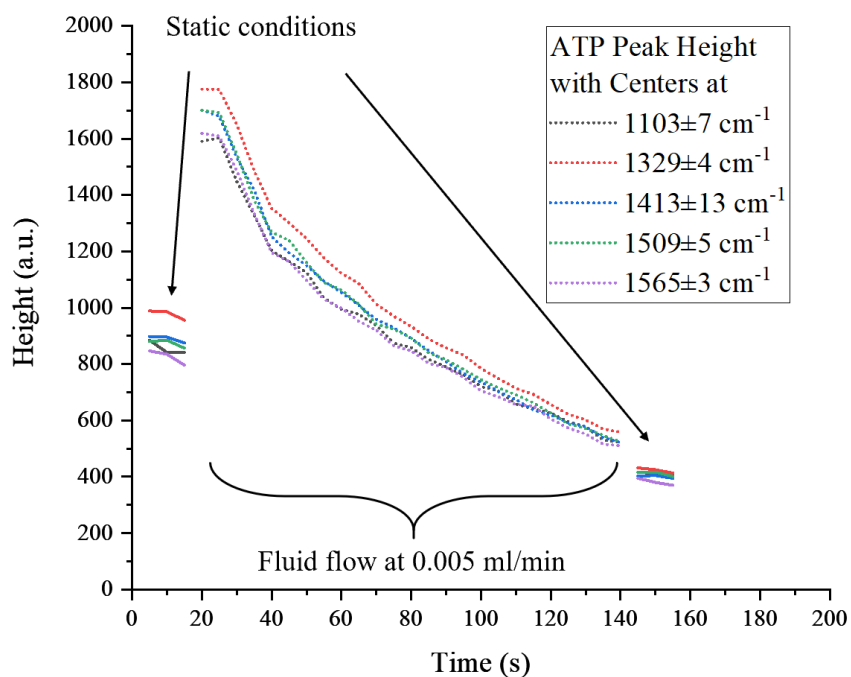
Figure 49 – Raman spectroscopic peak height of the phosphate bonds from ATP that appear between 1000 -1600 cm^{-1} as the concentration of ATP decreases over time. Solid lines represent height measurements acquired during static conditions and dotted lines represent height measurements acquired during fluid flow at a constant rate of 0.005 ml/min.

The intensity of the static measurements can be compared, indicating less ATP is present in the chamber after dilution with water. At initial fluid flow, the increase in intensity due to the addition of energy is recorded, aligning with the results in chapter 4 that related intensity to fluid flow. During fluid flow, the intensity of the ATP peaks decreases with time as the concentration in the chamber decreases.

5.6 Mass Balance Analysis

After investigating the effects of a single fluid flow rate on ATP concentration in our microfluidic chamber, we felt it was necessary to test the effects of multiple fluid flow rates, since the concentration of ATP in the reactor is directly related to the initial concentration and inlet flowrate. We loaded 10 mg/ml ATP solution into the chamber and diluted with an inlet stream of water at varying flowrates to evaluate the changes in the peaks identified using the adaptive PCA method above. We chose to evaluate the height of the phosphate bond that appears at 1565 cm^{-1} since this resulted in the greatest PC1 dip in both solid and solution forms. We plotted this peak height change as a function of time at varying flowrates through the microfluidic chamber. Figure 50 displays this analysis in conjunction with the height of the -OH vibrational mode that appears in water. This was for validation that the overall spectra intensity was not decreasing due to instrumental effects proving the decreases in the phosphate peak height are related to flowrates of water.
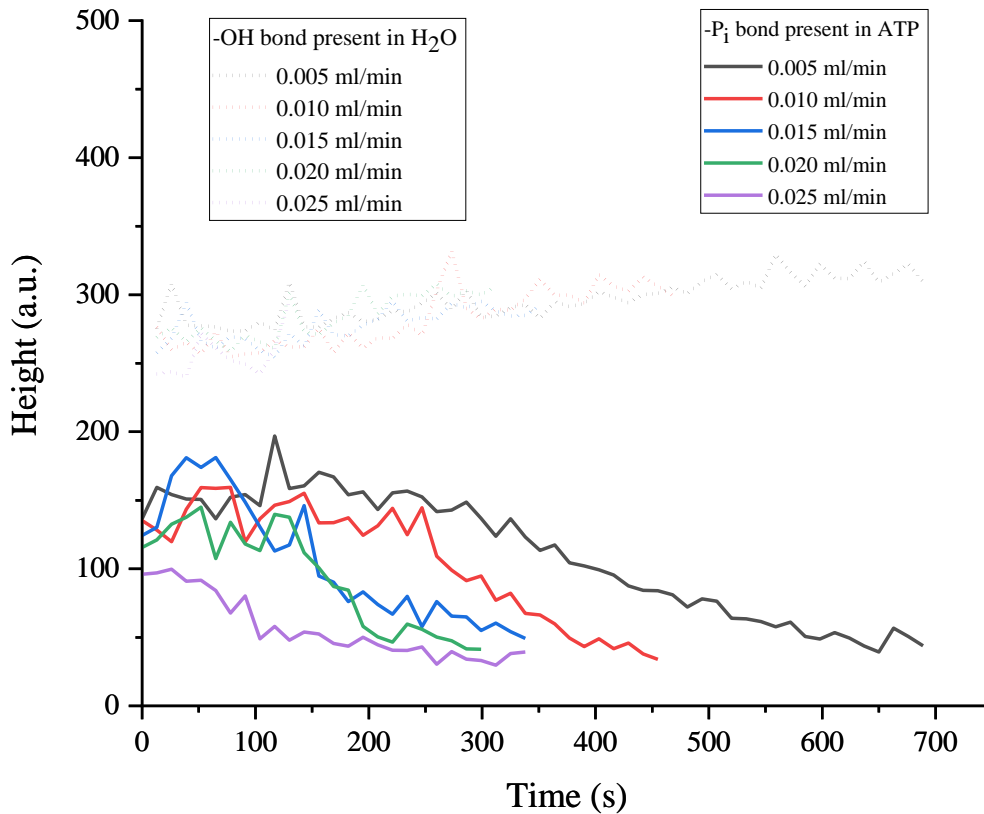
Figure 50 – Raman spectroscopic peak height of the phosphate bonds from ATP (shown by solid lines) and the -OH bonds from water (shown by dotted lines) as the concentration of ATP decreases over time for varying flowrates.

It is also necessary to understand the behaviour of ADP concentration in the chamber to verify the detectability limit of the Raman instrument since the maximum concentration achievable in the chamber is 2 mg/ml according to the mass balance shown in the methods section. To test this, we loaded the chamber with water and initiated fluid flow of varying concentrations of ADP. The fluid flow measurements are recorded and analysed to track the height of the phosphate bonds that appear between 1000-1600 cm^{-1} shown in figure 51. The height of the OH vibrational mode is also shown for verification that the phosphate peaks in ADP are increasing due to the inlet concentration and retention in the chamber. At 56 s the concentration of ADP in the chamber reaches a detectable limit and continues to

increase until 126 s at which point the concentration reaches the maximum achievable concentration.
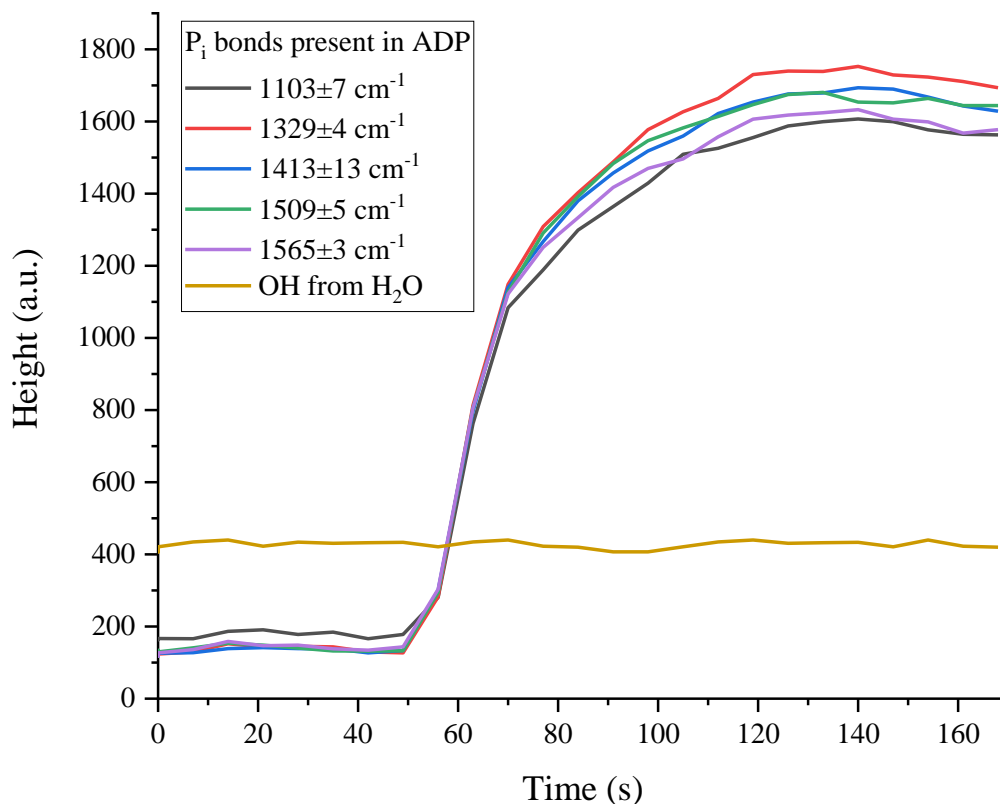
Figure 51 - Raman spectroscopic peak height of the phosphate bonds from ADP that appear between 1000-1600 cm^{-1} and the -OH bond from water as the concentration of ADP increases over time.

Based on these results, we decided to load the chamber with a solution of 10 mg/ml ATP and an inlet concentration of 50 mg/ml ADP at a rate of 0.005 mg/ml. Raman spectra was collected over the wavenumber range of 1000-1600 cm^{-1} continuously with each scan taking 5s to complete. The height of the phosphate bonds in that region are plotted as a function of time in figure 52. The ATP concentration decreases as the ADP concentration increases. At 224 s the detectable limit of ADP is reached and the modes at 1103 cm^{-1}, 1329

cm^{-1}, 1413 cm^{-1} and 1509 cm^{-1} increase until 378 s when the max ADP concentration is reached. The vibrational mode at 1565 cm^{-1} does not increase indicating the concentration in the chamber is transitioning from ATP to ADP. This provides evidence that monitoring the transition form ATP to ADP during the phosphorylation reaction is achievable.
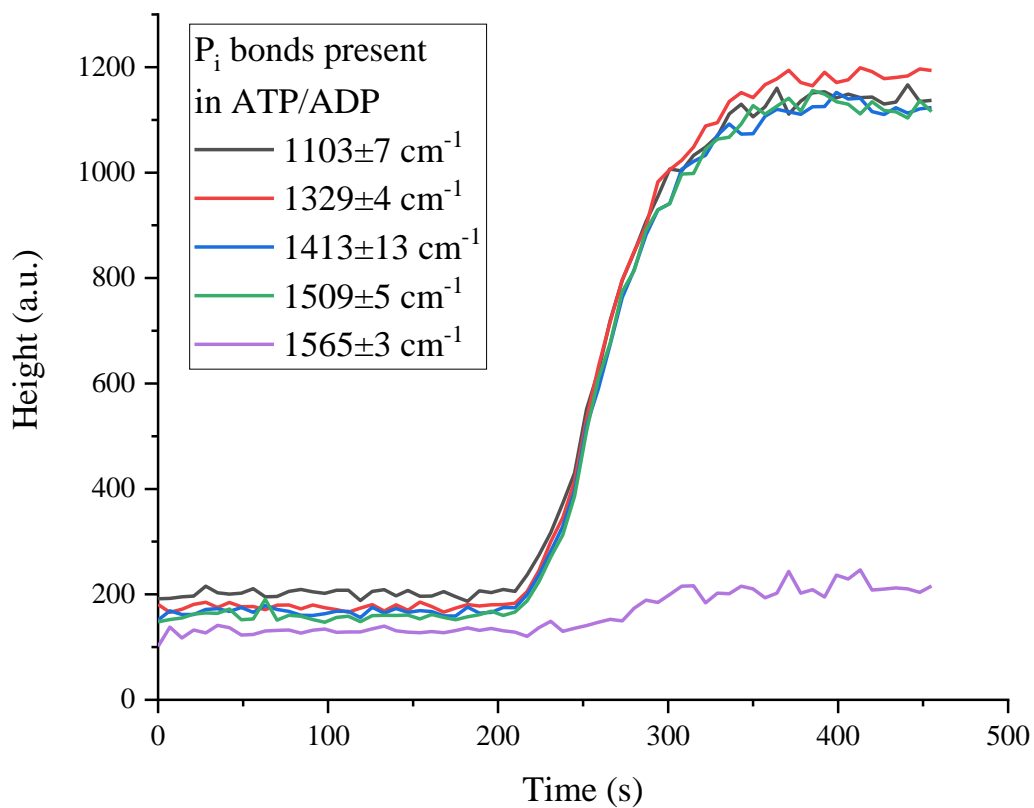
Figure 52 - Raman spectroscopic peak height of the phosphate bonds from ATP/ADP that appear between 1000-1600 cm^{-1} as the concentration of ATP decreases over time from an inlet stream of 10 mg/ml of ADP and an initial concentration of 50 mg/ml of ATP.

5.7 Monitoring ATP transition to ADP during Phosphorylation of Casein

To monitor the phosphorylation of Casein catalysed by PKA the chamber was loaded with Casein in $MgCl_2$ solution initially, then a solution of PKA/cAMP/ATP in $MgCl_2$ was added. Solutions were mixed and loaded into 1 ml syringes with 30g needles attached to the chamber with Tygon tubing as described before. Table 3 displays the concentrations used.

Table 3 – Concentrations of reagents mixed with aq. $MgCl_2$ for the phosphorylation of Casein.

Reagent	mass, mg	volume, ml	concentration, mg/ml
Casein	0.01	1	0.01
PKA	0.01	1	0.01
cAMP	0.05	1	0.05
ATP	0.05	1	0.05

Initial Raman spectral was collected on each individual solution. At time, $t = 0$, the reactor is preloaded with the Casein $MgCl_2$ solution, and no ATP is present in the chamber. The instrument was set-up to collect a scan every second. The PKA/cAMP/ATP in $MgCl_2$ solution flow was initiated at the same time the first measurement was acquired. The PKA/cAMP/ATP in $MgCl_2$ solution was allowed to flow at a rate of 0.005 mg/min until the PO_x peaks between 1000-1600 cm^{-1} appeared in the spectra. At this point the fluid flow was stopped and the reaction was allowed to progress while Raman spectra was collected every second over the wavenumber range 1000 – 1600 cm^{-1} until the P_i peak heights appeared to stop changing. Figure 53 and 54 display the Raman spectra collected for two reactions that were performed this way.
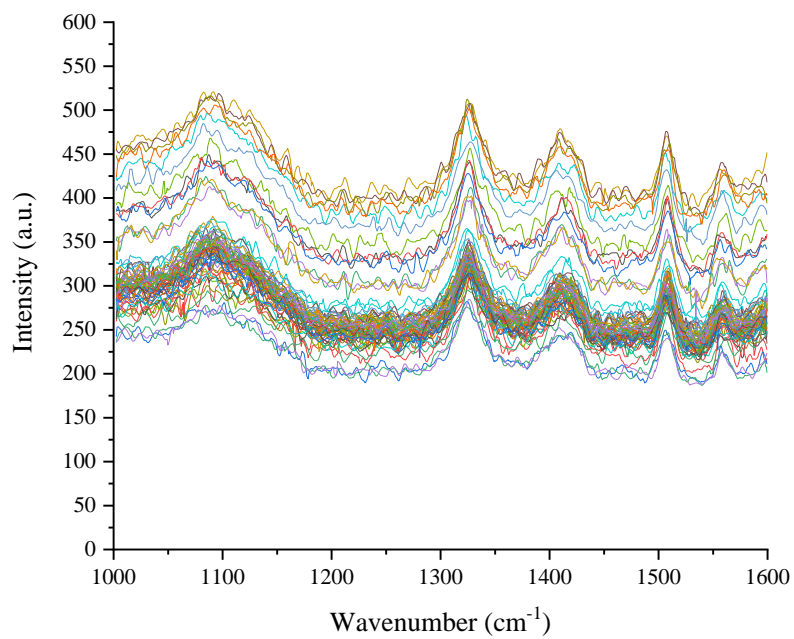
Figure 53 - Raman spectra of phosphorylation reaction (1) collected every second as the reaction progressed.
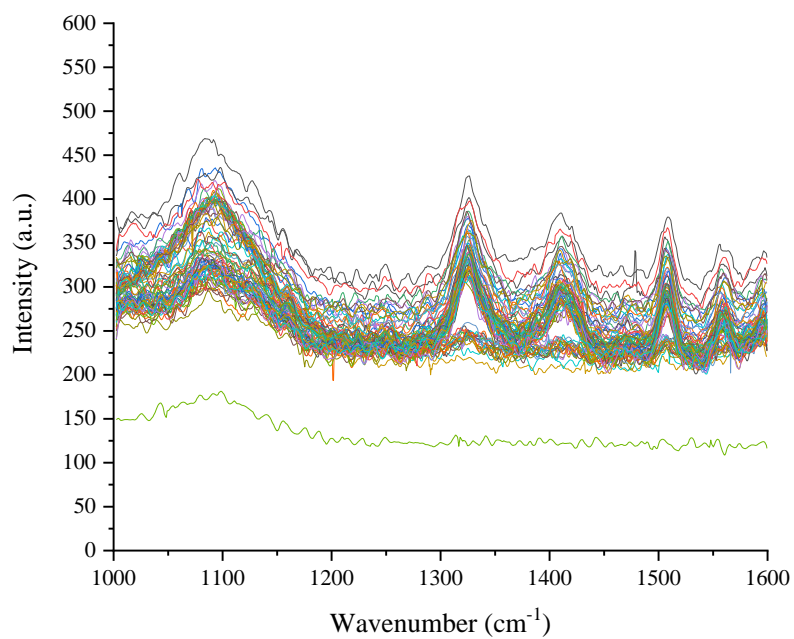
Figure 54 – Raman spectra of phosphorylation reaction (2) collected every second as the reaction progressed.

To interpret if the reaction occurred the heights of the phosphate bonds are plotted against time to see their relative changes. Figures 55 and 56 display the height changes of the P_i bonds for these two reactions. In both data sets, the height of the PO_x bonds are steady from 0-10s. This is the baseline of the Casein solution in $MgCl_2$ when no ATP is present. At 10s, the ATP reaches the chamber and the PO_x peaks are detectable, shown by the drastic increase in the graphs. The peaks then begin to decrease as the reaction progresses. The peaks at 1090 (for both) cm^{-1} and 1329 & 1326 cm^{-1} (reaction 1 & reaction 2) start close together and rise and fall similarly. The peak at 1090 cm^{-1} starts at 267 (a.u.) and falls to 329 (a.u.) in reaction 1 and starts at 250 (a.u.) and falls to 304 (a.u.) in reaction 2. The peak at 1329 cm^{-1} in reaction 1 starts at 264 (a.u.) and declines to 305 (a.u.), and the peak at 1326 cm^{-1} in reaction 2 starts at 246 (a.u.) and declines to 307 (a.u.). The same trend can be seen for the peaks at 1411 & 1412 cm^{-1} and 1506 & 1508 cm^{-1}. The peak at 1411 cm^{-1} in reaction 1 starts at 243 (a.u.) and declines to 283 (a.u.), and the peak at 1412 cm^{-1} in reaction 2 starts at 205 (a.u.) and declines to 276 (a.u.). The peak at 1506 cm^{-1} in reaction 1 starts at 239 (a.u.) and declines to 287 (a.u.), and the peak at 1412 cm^{-1} in reaction 2 starts at 205 (a.u.) and declines to 273 (a.u.). The peak at 1558 & 1554 cm^{-1} starts much lower that the others, rise the same order, but decreases at a faster rate during the reaction progression. The peak at 1558 cm^{-1} in reaction 1 starts at 224 (a.u.) and declines to 222 (a.u.), and the peak at 1412 cm^{-1} in reaction 2 starts at 176 (a.u.) and declines to 177 (a.u.). Taking into account the starting point of each peak and where each peak height ended, the peaks at 1558 & 1554 cm^{-1} for reaction 1 and 2 respectively are the only peaks that fall to their starting value. The other four peaks in each reaction decrease, but do not reach the same starting value. This aligns with the results seen in the mass transfer analysis. The peaks at 1558 & 1554 cm^{-1} for these two reactions are indicative that the ATP transition to ADP is occurring in the solution signifying the reaction is occurring.
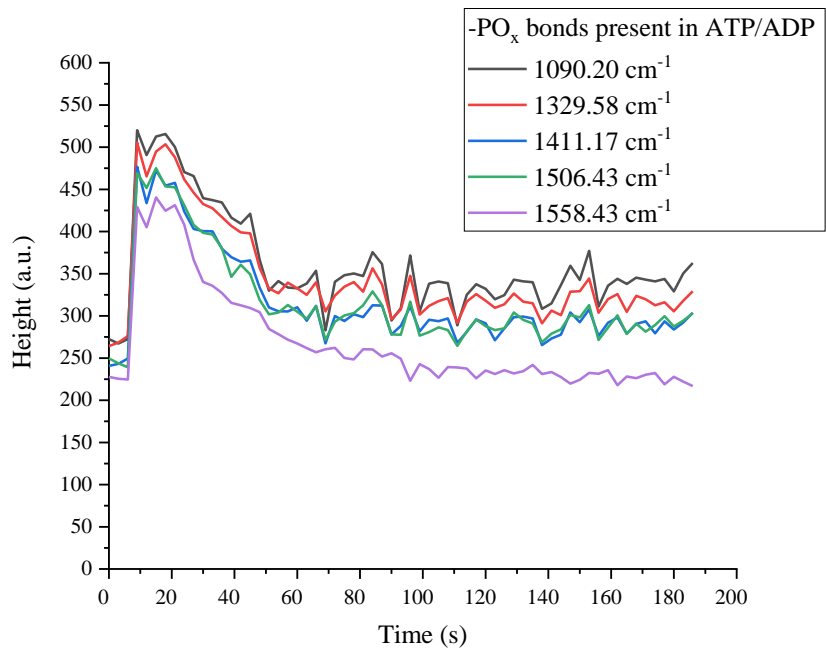
Figure 55 – Height of Pi bonds in ATP/ADP plotted against time of phosphorylation reaction (1) collected every second as the reaction progressed
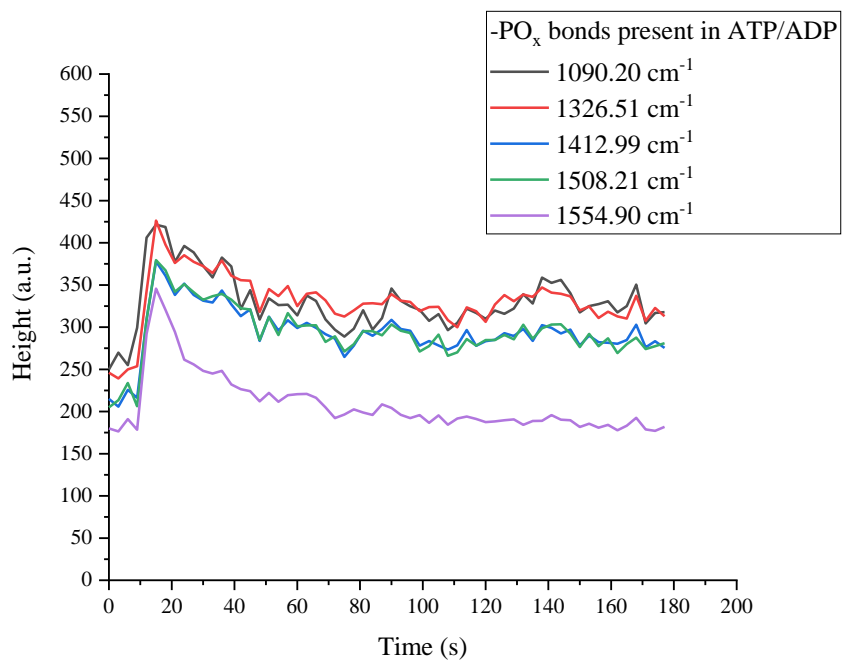
Figure 56 - Height of Pi bonds in ATP/ADP plotted against time of phosphorylation reaction (2) collected every second as the reaction progressed

5.8 Isoelectric Focusing Verification

To verify this result, isoelectric focusing (IEF) was performed on the reaction products retrieved from the chamber. IEF was performed using a BioRad CriterionTM Vertical Electrophoresis Cell with Criterion precast protein gels. The gels are 18 well comb, 30 μl, pH 3-10, 1.0 mm thick. Products from the microfluidic reactor were mixed with sample buffer and a tracking dye for verification of the isoelectric point. Figure 57 is an image of the IEF results. In lanes 1-4, unphosphorylated Casein in sample buffer were loaded. In lanes 9-11, phosphorylated Casein in sample buffer were loaded as a control sample. In lanes 15-18, phosphorylation reaction products in sample buffer were loaded. Reaction 1 products were loaded in lanes 15 and 16. Reaction 2 products were loaded in lanes 17 and 18. Lanes 5-7, and 12-14 were intentionally left empty. IEF was run for 30 min at 75 volts, 30 min at 150 volts, and 30 min at 75 volts. The isoelectric point of phosphorylated Casein, pI = 4.5 - 4.7, dephosphorylated Casein pI = 5.1, and PKA pI = 8.8 as reported from previous literature [7]. In figure 57, the dephosphorylated Casein samples stopped migrating around the 5.1 pI region, the phosphorylated control samples in lanes 9-11 stopped migrating near the 4.7 region. In lanes 15-18, the reaction products stopped migrating around 8.9 pI, indicating the PKA migrated to this point, and the phosphorylated products migrated to 4.5 pI region indicating the Casein phosphorylated during the reaction performed in the microfluidic reactor.
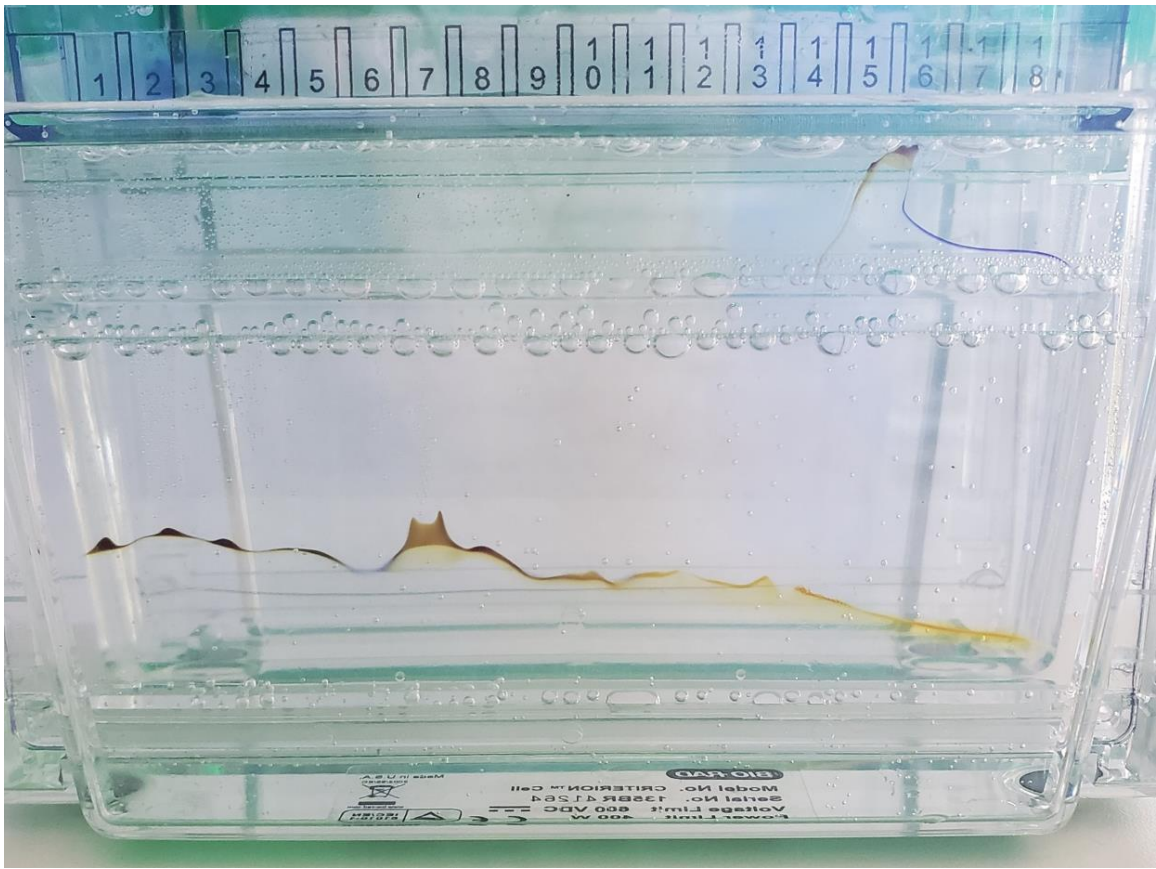
Figure 57 – Isoelectric focusing of control proteins and phosphorylation reaction products. The pH range of the gel is from 10 (top) to 3 (bottom).

Chapter 6 Conclusions

This study successfully monitored the phosphorylation of Casein through catalysis of PKA and phosphate donation from ATP. This reaction was monitored in real-time by detecting the intensity change of the PO_x vibrational mode at 1556 cm^{-1} that appears in ATP during the reaction progression. The intensity of this vibrational mode decreased to the base level where no ATP is present.

6.1 Adaptive Principal Component Analysis

The development of an adaptive PCA method in this study was crucial for the extraction of salient features of biomolecules that occurs during biochemical reactions. This algorithm was first applied to BCAAs with the intent of tuning the method to be capable of extracting features from very similar biomolecules. This method identified the vibrational modes that were under strain in three branched chain amino acids and four blended samples of these amino acids. The 2:1:1 blend experienced the greatest strain with $\delta(NCC)$ of L-isoleucine at 337.26 cm^{-1} under tension and $\delta_s(CH_3)$ of L-isoleucine at 1395. 92 cm^{-1} under compression. The greatest peak shift from all three appeared in L-isoleucine of the $\tau(CH)$ bond which also shows the lowest value for PC1. L-valine's PC1 valleys were less than that of the other two amino acids and correlates with the smaller peak shift ranges in the peak analyzation.

The application of this method to ATP and ADP samples demonstrated promise that monitoring the concentration changes during the protein phosphorylation is achievable. This method identified that the PO_x vibrational modes at 1090 cm^{-1}, 1329 cm^{-1}, 1411 cm^{-1}, 1506 cm^{-1} and 1558 cm^{-1} are present in both samples and result in the greatest variance between the two. These results indicated

the modes at 1090 cm^{-1} and 1558 cm^{-1} were significant in monitoring the transition of ATP to ADP during the protein phosphorylation reaction.

6.2 3D Printed Microfluidic Device Integration with Raman Spectroscopy

The second enabling technology developed in this study was the design and fabrication of a microfluidic reactor that was successfully integrated with a confocal Raman spectrometer. By developing this reactor this research is capable of utilizing key features of the Raman spectrometer to monitor the protein phosphorylation reaction. These features include:

- Non-destructive and non-contact

- Lack of interference from water

- 3D spatial resolution

- Spectral acquisition speed

This development also enables future research to be conducted on numerous other biochemical reactions utilizing the Raman spectrometer. Additionally, this design enables translating this research to analyze biochemical reactions intracellularly. The microfluidic reactor described in this work was assembled from a 3D printed device that is placed between a cover slip and a standard glass slide with microdrilled holes. The 3D printed side walls took less than an hour to print 12 identical slides, decreasing the fabrication time over traditional PDMS soft lithography significantly. This method for printing the 3D side walls enables future research to quickly design the channel pattern and print multiple designs at once. This would enable rapid prototyping allowing researchers to tailor a reactor for specific reactions and applications. The results performed on solutions in this reactor suggest that this will be a successful method for fabricating

a microfluidic device to monitor the molecular transition of ATP to ADP. Fluid flow results indicated that Raman spectral response was increased during fluid flow, but did not eliminate the reaction indicating vibrational modes. The increase in intensity during fluid flow is due to the energy imparted on the fluid during flow, increasing the spectral response.

6.3 Monitoring ATP transition to ADP

Based on the reaction mechanism described in chapter 2, the chemical transition of adenosine triphosphate (ATP) to adenosine diphosphate (ADP) will be the reaction indicating species. The adaptive PCA method enabled the identification of the PO_x vibrational modes that will be monitored during the reaction. The microfluidic device designed to monitor the transition of ATP to ADP was successful during the mass transfer experiment and the protein phosphorylation reaction. The vibrational modes at 1558 & 1554 cm^{-1} for reaction 1 and 2 respectively are the only peaks that fall to the initial value recorded. The isoelectric points were verified for the reaction products. The dephosphorylated Casein samples stopped migrating around the 5.1 pI region, the phosphorylated control samples stopped migrating near the 4.7 region and the reaction products stopped migrating around 8.9 pI, indicating the PKA migrated to this point, and the phosphorylated products migrated to 4.5 pI region indicating the Casein phosphorylated during the reaction performed in the microfluidic reactor.

Chapter 7 Future Work

The real-time monitoring of biochemical reactions in microfluidic devices will benefit from signal enhancement of the Raman spectra. This may be performed through surface-enhanced Raman scattering using nanoparticles or nanoantennas from agglomerations of nanoparticles. The adaptive principal component analysis algorithm may be further developed to identify variance in vibrational modes as a function on signal enhancement. By enhancing the signal, this research would be open to the application of numerous biochemical reactions, not limited to protein phosphorylation. Another way to enhance the Raman signal would be fixed substrate nano-features within the microfluidic reactor. Specifically, the addition of fabricated bowtie nanoantennas on the inner surface of the bottom glass slide of the microfluidic reactor developed in this research study. By choosing to utilize a fixed nanofeature we can eliminate any potential interaction from flowing nanoparticles with the biochemical reaction. With a fixed substrate nanofeature we can also ensure consistent enhancement of the Raman signal.

This work also implements a foundation for research towards intracellular biochemical reaction monitoring. This advances research towards the overarching goal of developing an instrument that may be used clinically to aid in patient diagnosis, prognosis and treatment efficacy. The ease of designing and 3D printing the channel side walls enables rapid prototyping for various applications. For intracellular applications, it is proposed that the 3D printed side walls be designed with features to capture the cells in a pocket, immobilizing them for Raman interrogation. Another enabling technology within the research is the 3D spatial resolution of the confocal Raman spectrometer, which allows future cellular work to focus on different areas of the cell. For example,

various receptor effects could be studied on the cell membrane or transduction mechanisms could be studied within the cell by changing the Raman collection window.

The adaptive PCA algorithm could be futher developed to automatically calculate the wavenumber shifts for peaks identified as having the greatest PC1 valleys of a data set. Furthermore, the calculation of the energy shifts associated with the wavenumber shift could relay stress/strain during conformational changes of a biomolecule. This algorithm could also be advanced to be implemented in real-time with the Raman spectrometry data to relay variance as the biochemical reaction progresses

References

[1] S. Petrakis and M. A. Andrade-Navarro, Protein Interaction Networks in Health and Disease, 2016.

[2] J.-i. Abe and B. C. Berk, "Reactive Oxygen Species as Mediators of Signal Transduction in Cardiovascular Disease," *Trends in Cardiovascular Medicine,* vol. 8, no. 2, pp. 59-64, 1998.

[3] R. Sever and J. S. Brugge, "Signal Transduction in Cancer," *Cold Spring Harbor Persepctives in Medicine,* vol. 5, pp. 1-12, 2015.

[4] S. Hoyer, "Glucose metabolism and insulin signal transduction in Alzheimer disease," *Journal of Pharmacology,* vol. 490, pp. 115-125, 2004.

[5] L. Wells, K. Vosseller and G. W. Hart, "Glycosylation of Nucleocytoplasmic Proteins: Signal Transduction and O-GlcNAc," *SCIENCE,* vol. 291, pp. 2376-2378, 2001.

[6] Price, M.D., Thomas E.; Schuchat M.D., Anne; Rothwell, MS, M.B.A., Charles J.;, "Health, United States, 2016," National Center for Health Statistics, Washington DC, 2017.

[7] M. P. Conn and A. R. Means, Principles of Molcular Regulation, Springer, 2011.

[8] K.-P. Huang, "The mechanism of protein kinase C activation," *Trends in Neurosciences,* vol. 12, no. 11, pp. 425-432, 1989.

[9] A. Giralt, A. Saavedra, O. Carreton, X. Xifro, J. Alberch and E. Perez-Navarro, "Increased PKA signaling disrupts recognition memory and spatial memory: rold in Huntington's disease," *Human Molecular Genetics,* vol. 20, no. 21, pp. 4232-4247, 2011.

[10] N. Myeku, C. L. Clelland, S. Emrani, N. V. Kukushkin, W. H. Yu, A. L. Goldberg and K. E. Duff, "Tau-drive 26S proteasome impairment and cognitive dysfunction cna be prevented early in disease by activating cAMP-PKA signaling," *Nature Medicine,* vol. 22, no. 1, pp. 46-56, 2016.

[11] R. K. Dagda, A. M. Gusdon, I. Pien, S. Strack, S. Green, C. Li, B. V. Houten, S. J. Cherra III and C. T. Chu, "Mitochondrially localized PKA reverses mitochondrial pathology and dysfunction in a cellular model of Parkinson's disease," *Cell Death and Differentiation,* vol. 18, pp. 1914-1923, 2011.

[12] K. Nightingale, M. Scott Soo, R. Nightingale and G. Trahey, "Acoustic Radiation Force Impulse Imaging: In vivo Demostration of Clinical Feasibility," *Ultrasound in Medicine and Biology,* vol. 28, no. 2, pp. 227-235, 2002.

[13] D. J. Brenner and E. J. Hall, "Computed Tomography - An Increasing Source of Radiation Exposure," *The New England Journal of Medicine,* pp. 2277-2284, 2007.

[14] F. A. Mettler, W. Huda, T. T. Yoshizumi and M. Mahesh, "Effective Doses in Radiology and Diagnostic Nuclear Medicine," *Radiology,* vol. 248, no. 1, pp. 254-263, 2008.

[15] B. Burk, "Whole-Body Computerized Tomography Screening should not be Performed," Health Physics Society, 2007.

[16] M. A. Brown, MRI: basic principles and applications, Hoboken, NJ: Wiley-Liss, 2003.

[17] A. P. Carlson, H. Yonas, Y.-F. Chang and E. Nemoto, "Failure of Cerebral Hemodynamic Selction in General or of Specific Positron Emission Tomography Methodology," *Stroke,* pp. 3637-3639, 2011.

[18] R. Roskoski Jr., "Enzyme Structure and Function," *Reference Module in Biomedical Sciences,* pp. 1-7, 2007.

[19] E. G. Krebs, A. B. Kent and E. H. Fischer, "The Muscle Phosphorylase b Kinase Reaction," *The Journal of Biological Chemistry,* pp. 73-83, 1958.

[20] E. G. Krebs, D. J. Graves and E. H. Fischer, "Factors Affecting the Activity of Muscle Phosphorylase b Kinase," *Journal of Biological Chemistry ,* vol. 234, no. 11, pp. 2867-2873, 1959.

[21] P. A. Levene and C. L. Alsberg, "The Cleavage Products of Vitellin," *Journal of Biological Chemistry,* vol. 2, pp. 127-133, 1906.

[22] F. A. Lipmann and P. A. Levene, "Serinephosphoric Acid Obtained on Hydrolysis of Vitellinc Acid," *Journal of Biological Chemistry,* pp. 109-114, 1932.

[23] A. A. Green and G. T. Cori, "Crystalline Muscle Phosphorylase I. Preparation, Properties and Molecular Weight," *Journal of Biological Chemistry,* pp. 21-29, 1943.

[24] G. T. Cori and A. A. Green, "Crystalline Muscle Phosphorylase II. Prosthetic Group," *Journal of Biological Chemistry,* pp. 31-38, 1943.

[25] C. F. Cori, G. T. Cori and A. A. Green, "Crystalline Muscle Phosphorylase III. Kinetics," *Journal of Biological Chemistry,* pp. 39-55, 1943.

[26] E. G. Krebs and E. H. Fischer, "Phosporylase Activty of Skeletal Muscle Extracts," *Journal of Biological Chemistry,* pp. 113-120, 1955.

[27] E. H. Fischer and E. G. Krebs, "Conversion of Phosphorylas b to Phosphorylase a in Muscle Extracts," *Journal of Biological Chemistry,* pp. 121-132, 1955.

[28] F. . EH, "Phosphorylase and the origin of reversible protein phosphorylation," *Biol Chem,* vol. 391, no. 2–3, p. 131–137, 2010.

[29] D. M. Neville and H. Glossman, "Molecular Weight Determination of Membrane Protein and Glycoprotein Subunits by Discontinuous Gel Electrophoresis in Dodecyl Sulfate," in *SDS Gel Electrophoresis, Characterization of Membranes and Components*, 1971, pp. 92-102.

[30] M. Douglas, D. Finkelstein and R. A. Butow, "Analysis of Products of Mitochondrial Protein Synthesis in Yeast: Genetic and Biochemical Aspects," in *Methods in Enzymology Vol 56*, New York, NY, 1976, pp. 58-66.

[31] J. Y. Henderson, A. J. G. Moir, L. A. Fothergill and J. E. Fothergill, "Sequences of Sixteen Phosphoserine Peptides from Ovalbumins of Eight Species," *European Journal of Biochemistry,* pp. 439-450, 1981.

[32] A. Aitken, T. Bilham, P. Cohen, D. Aswad and P. Greengard, "A specific Sunstrate from Rabbit Cerebellum for Guanosine-3':5'-monophosphate-dependent Protein Kinase".

[33] H. Towbin, T. Staehelin and J. Gordon, "Electrophoretic transfer of proteins from polyacrylamide gels to nitrocellulose sheets: Procedure and some applications," *Proc. Natl. Acad. Sci.,* vol. 76, no. 9, pp. 4350-4354, 1979.

[34] W. N. Burnette, ""Western Blotting": Electropheretic Transfer of Proteins from Sodium Dodecyl Sulfate - Polyacrylamide Gels to Unmodified Nitrocellulose and Radiographic Detection with Antibody and Redioiodinated Protein A," *Analytical Biochemistry,* vol. 112, pp. 195-203, 1981.

[35] S. Sullivan and T. W. Wong, "A Manual Sequencing Method for Identification of Phosphorylated Amino Acids in Phosphopeptides," *Analytical Biochemistry,* vol. 197, pp. 65-68, 1991.

[36] H. Schagger and G. von Jagow, "Tricine-Sodium Dodecly Sulfate-Polyacrylamide Gel Electrophoresis for the Separation of Proteins in the Range from 1 to 100 kDa," *Analytical Biochemistry,* vol. 166, pp. 368-379, 1987.

[37] H. Schagger, H. Aquila and G. VonJagow, "Coomassie Blue-Sodium Dodecyl Sulfate-Polyacrylamide Gel Electrophoresis for Direct Visualization of Polypeptides during Electrophoresis," *Analytical Chemistry,* vol. 173, pp. 201-205, 1988.

[38] R. Aebersold, J. D. Watts, H. D. Morrison and E. J. Bures, "Determination of the Site of Tyrosine Phosphorylation at the Low Picomole Level by Automated Solid-Phase Sequence Analysis," *Analytical Biochemistry,* vol. 199, pp. 51-60, 1991.

[39] R. E. H. WettenHall, R. H. Aebersold and L. E. Hood, "Solid-Phase Sequencing of 32P-Labeled Phosphopeptides at Picomole and Subpicomole Levels," in *Analysis of Protien Phosphorylation*, 1991, pp. 186-199.

[40] J. X. Yan, N. H. Packer, A. A. Gooley and K. L. Williams, "Protein Phosphorylation: Technologies for the identification of phosphoamino acids," *Journal of Chromatography A,* vol. 808, pp. 23-41, 1998.

[41] L. N. Amankwa, K. Harder, F. Jirik and R. Aebersold, "High-sensitive determination of tyrosine-phosphorylated peptides by on-line enzyme reactor and electrospray ionization mass spectrometry," *Protein Science,* vol. 4, pp. 113-125, 1995.

[42] M. Yamashita and J. B. Fenn, "Electrospray Ion Source. Another Variation on the Free-Jet Theme," *American Chemical Society,* p. 9, 1984.

[43] C. M. Whitehouse, R. N. Dreyer, M. Yamashita and J. B. Fenn, "Electrospray Interface for Liquid Chromatographs and Mass Spectrometers," *Analytical Chemistry,* pp. 675-679, 1985.

[44] M. Karas, D. Bachmann and F. Hillenkamp, "Influence of the Wavelenth in High-Irradiance Ultraviolet Laser Desorption Mass Spectrometry of Organic Molecules," *Analytical Chemisty,* p. 5, 1985.

[45] K. Tanaka, H. Waki, Y. Ido, S. Akita and Y. Yoshida, "Protein and Polymer Analyses up to m/z 100,000 by Laser Ionization Time-of-Flight Mass Spectrometry".

[46] M. Karas and U. Bahr, "Laser desorption ionization mass spectrometry of large biomolecules," *Trends in Analytical Chemistry,* p. 5, 1990.

[47] J. S. L. Philpot, "The use of Thin Layers in Electrophoretic Separation," *Trans. Faraday Soc.,* 1940.

[48] A. Manz, N. Graber and H. M. Widmer, "Miniatureized Total Chemical Analysis Systems: a Novel Concept for Chemical Sensing," *Sensors and Actuators,* vol. B1, pp. 244-248, 1990.

[49] K. S. Elvira, X. C. Solvas, R. C. Wootton and A. J. deMello, "The past, present, and potential for microfluidic reactor technology in chemical synthesis," *Nature Chemistry,* vol. 5, pp. 905-915, 2013.

[50] J. P. McMullen, M. T. Stone, S. L. Buchwald and F. K. Jensen, "An Integrated Microreactor System for Self-Optimization of a Heck Reaction: From Micro-to Mesoscale Flow Systems," *Microreactors Communications,* vol. 49, pp. 7076-7080, 2010.

[51] R. L. Hartman, J. P. McMullen and K. F. Jensen, "Deciding Whether to go with the Flow: Evaluating the Merits of Flow Reactors for Synthesis," *Reviews in Flow Chemistry,* vol. 50, pp. 7502-7519, 2011.

[52] C.-C. Lee, G. Sui, A. Elizarov, C. J. Shu, Y.-S. Shin, A. N. Dooley, J. Huang, A. Daridon, P. Wyatt, D. Stout, H. C. Kolb, O. N. Witte, N. Satyamurthy, J. R. Heath, M. E. Phelps, S. R. Quake and H.-R. Tseng, "Multistep Synthesis of a Radilabeled Imaging Probe Using Integrated Microfluidics," *Science mag,* vol. 310, pp. 1793-1796, 2005.

[53] D. Kralisch and G. Kreisel, "Assessment of the ecological potential of microreaction technology," *Chemical Engineering Science,* vol. 62, pp. 1094-1100, 2007.

[54] L. Saias, J. Autebert, L. Malaquin and J.-L. Viovy, "Design, modeling and characterization of microfluidic architectures for high flow rate, small footpring microfluidic systems," *Royal Society of Chemistry,* vol. 11, pp. 822-832, 2011.

[55] J. R. Goodell, P. J. McMullen, N. Zaborenko, J. R. Maloney, C.-X. Ho, K. F. Jensen, J. A. Porco Jr. and A. B. Beeler, "Development of an Automated Microfluidic Reaction Platform for Multidimensional Screening: Reaction Discovery Employing Bicyclo[3.2.1]octanoid Scaffolds," *J. Org. Chem,* vol. 74, pp. 6169-6180, 2009.

[56] T. Illg, V. Hessel, P. Lob and J. C. Schouten, "Continuous Synthesis or tert-Butyl Peroxypivalate using a Single-Channel Microreactor Equipped with Orifices as Emulsification Units," *ChemSusChem,* vol. 4, pp. 392-398, 2011.

[57] H. Pennemann, P. Watts, S. J. Haswell, V. Hessel and H. Lowe, "Benchmarking of Microreactor Applications," *Org. Proc. R&D,* vol. 8, pp. 422-439, 2004.

[58] Y. Bi, H. Zhou, H. Jia and P. Wei, "A flow-through enzymatic microreactor immobilizing lipase based on layer-by-layer method for biosynthetic process: Catalyzing the transesterification of soybean oil for fatty acid methyl ester production," *Process Biochemistry,* vol. 54, pp. 73-80, 2017.

[59] K. Geyer and P. H. Seeberger, "Optimization of Glycosylation Reactions in a Microreactor," *Helvetica Chimica Acta,* vol. 90, pp. 395-403, 2007.

[60] F. R. Carrel, K. Geyer, J. D. Codee and P. H. Seeberger, "Oligosaccharade Synthesis in Microreactors," *Organic Letters,* vol. 9, no. 12, pp. 2285-2288, 2007.

[61] J. W. Hong, V. Studer, G. Hang, W. F. Anderson and S. R. Quake, "A nanoliter-scale nucleic acid processor with parallel arcitecture," *Nature Biotechnology,* vol. 22, no. 4, pp. 435-439, 2004.

[62] M. Slovakova, N. Minc, Z. Bilkova, C. Smadja, W. Faigle, C. Futterer, M. Taverna and J.-L. Viovy, "Use of self assembled magnetic beads for on-chip protein digestion," *Lab on a Chip,* pp. 935-942, 2005.

[63] A. Schwarz, M. S. Thomsen and B. Nidetzky, "Enzymatic Synthesis of B-Glucosylglycerol Using a Continuous-Flow Microreactor Containing Thermostable B-Glycoside Hydrolase CelB Immobilized on Coated Microchannel Walls," *Biotechnology and Bioengineering,* vol. 103, no. 5, pp. 865-872, 2009.

[64] M. A. Schoffner, J. Cheng, G. E. Hvichia, L. J. Kricka and P. Wilding, "Chip PCR. I. Surface passivation of microfabricated silicon-glass chips for PCR," *Nucleic Acids Research,* vol. 24, no. 2, pp. 375-379, 1996.

[65] J. Cheng, M. A. Shoffner, G. E. Hvichia, L. J. Kricka and P. Wilding, "Chip PCR. II. Investigations of different PCR amplification systems in microfabricated silicon-glass chips," *Nucleic Acids Research,* vol. 24, no. 2, pp. 380-385, 1996.

[66] I. Moser, G. Jobst, P. Svasek, M. Varahram and G. Urban, "Rapid Liver enzyme assay with miniturized liquid handling system comprising thin film biosensor array," *Sensors and Actuators B,* vol. 44, pp. 377-380, 1997.

[67] A. G. Hadd, D. E. Raymond, J. W. Hallwell, S. C. Jacobson and J. M. Ramsey, "Microchip Device for Performing Enzyme Assays," *Analytical Chemistry,* vol. 69, no. 17, pp. 3407-3412, 1997.

[68] Z. Csapo, A. Gerstner, M. Sasvari-Szekely and A. Guttman, "Automated Ultra-Thi-Layer SDS Gel Electrophoresis of Proteins Using Noncovalent Fluorescent Labeling," *Anal. Chem,* vol. 72, pp. 2519-2525, 2000.

[69] L. Bousee, S. Mouradian, A. Minalla, H. Yee, K. Williams and R. Dubrow, "Protein Sizing on a Microchip," *Anal. Chem,* vol. 73, pp. 1207-1212, 2001.

[70] N. Xu, Y. Lin, S. A. Hofstadler, D. Matson, C. J. Call and R. D. Smith, "A Microfabricated Dialysis Device for Sample Cleanup in Electrospray Ionization Mass Spectrometry," *Anal. Chem,* vol. 70, pp. 3553-3556, 1998.

[71] Y. Jiang, P.-C. Wang, L. E. Locascio and C. S. Lee, "Integrated Plastic Microfluidic Devices with ESI-MS for Drug Screening and Residue Analysis," *Anal. Chem,* vol. 73, pp. 2048-2053, 2001.

[72] P. D. I. Fletcher, S. J. Haswell and X. Zhang, "Monitoring of chemical reactions within microreactors using an inverted Raman microscope spectrometer," *Electrophoresis,* vol. 24, pp. 3239-3245, 2003.

[73] S.-A. Leung, R. F. Winkle, R. C. R. Wootton and A. J. deMello, "A method for rapid reaction optimisation in continuous-flow microfluidic reactors using online Raman spectroscopic detection," *The Royal Society of Chemistry,* vol. 130, pp. 46-51, 2004.

[74] D. J. Beebe, G. A. Mensing and G. M. Walker, "Physics and Applications of Microfluidics in Biology," *Annual Rev. Biomed. Eng. ,* pp. 261-286, 2002.

[75] N. Bhattacharjee, A. Urrios, S. Kang and A. Folch, "The upcoming 3D-printing revolution in microfluidics," *Lab on a Chip,* vol. 16, pp. 1720-1742, 2016.

[76] F. Sarrazin, J.-B. Salmon, D. Talaga and L. Servant, "Chemical Reaction Imaging within Microlfuidic Devices Using Confocal Raman Spectroscopy: The Case of Water and Deuterium Oxide as a Model System," *Analytical Chemistry,* vol. 80, pp. 1689-1695, 2008.

[77] A. Au, N. Bhattacharjee, L. Horowitz, T. Chang and A. Folch, "3D-printed microfluidic automation," *Lab on a Chip,* vol. 15, pp. 1934-1941, 2015.

[78] R. J. Jackman, T. M. Floyd, R. Ghodssi, M. A. Schmidt and K. F. Jensen, "Microfluidic systems with on-line UV detection fabricated in photodefinable epoxy," *J. Micromech. Microeng,* vol. 11, pp. 263-269, 2001.

[79] J. S. Moore and K. J. Jensen, "Automated Multitrajectory Method for Reaction Optimization in a Microlfuidic System using Online IR Analysis," *ACS Organic Process Research and Development,* vol. 16, pp. 1409-1415, 2012.

[80] Y. Liu, Y. Xue, J. Ji, X. Chen, J. Kong, P. Yang, H. H. Girault and B. Liu, "Gold Nanoparticle Assembly Microlfuidic Reactor for Efficient On-line Protesolysis," *Molecular and Cellular Proteomics,* vol. 6, no. 8, pp. 1428-1436, 2007.

[81] K. Hayashi, Y. Iwasaki, R. Kurita, K. Sunagawa and O. Niwa, "On-line microfluidic sensor integrated with a micro array electrode and enzyme-modified pre-reactor for the real-time monitoring of blood catecholamine," *Electrochemistry Communications,* vol. 5, pp. 1037-1042, 2003.

[82] P. A. Walker, W. K. Kowalchyk and M. D. Morris, "On-line Raman Spectroscopy of Ribonucleotides Preconcentrated by Capillary Isotachophoresis," *Anal. Chem.,* vol. 67, pp. 4255-4260, 1995.

[83] A. F. Chrimes, K. Khoshmanesh, P. R. Stoddart, A. Mitchell and K. Kalantart-zadeh, "Microlfuidics and Raman microscopy: current applications and future challenges," *Chem. Soc. Rev,* vol. 42, pp. 5880-5906, 2103.

[84] A. Urakawa, F. Trachsel, P. Rudolf von Rohr and A. Baiker, "On-chip Raman analysis of heterogeneous catalytic reaction in supercritical CO2: phase behaviour monitoring and activity profiling," *Royal Society of Chemistry,* vol. 133, pp. 1352-1354, 2008.

[85] G. L. Nelson, S. E. Asmussen, A. M. Lines, A. J. Casella, D. R. Bottenus, S. B. Clark and S. A. Bryan, "Micro-Raman Technology to Interrogate Two-Phase Extraction on a Microfluidic Device," *Analytical Chemistry,* vol. 90, no. 14, pp. 8345-8353, 2018.

[86] A. H. M. Casey, N. E. Chusan, C. A. Campbell and G. E. Triplett, "Protein phosphorylation reagent concentration curves via Raman spectroscopy for real-time reaction monitoring in a microfluidic reactor," *Proc. SPIE Nanoscience and Engineering,* 2019.

[87] J. Gu, H. Liu, C. Ma, L. Li, C. Zhu, C. Glorieux and G. Chen, "Conformal Prediction Based on Raman Spectra for the Classification of Chinese Liquors," *Applied Spectroscopy,* vol. 73, no. 7, pp. 759-766, 2019.

[88] N. A. Marigheto, E. K. Kemsley, J. Potter, P. S. Belton and R. H. Wilson, "Effects of sample heating in FT-Raman spectra of biological materials," *Spectrochimica Acta Part A,* vol. 52, pp. 1571-1579, 1996.

[89] K. Heremans, "High Pressure Effects on Proteins and other Biomolecules," *Ann. Rev. Biophys. Bioeng,* vol. 11, pp. 1-21, 1982.

[90] G. E. Triplett, G. S. May and A. S. Brown, "Using Neural Networks for RHEED Modeling of Interfaces in AlGaSb-InAs HEMT Devices," 2002.

[91] T. Brown and a. et, "Modeling MBE RHEEN signals using PCA and neural networks," *Compound Semiconductors 1997 IEEE Internation Symposium ,* 1997.

[92] I. T. Jolliffe, Principal Component Analysis, 2002.

[93] T. Brown, K. Lee, G. Dagnall, R. Kromann, R. Bicknell-Tassius, A. Brown, J. Dorsey and G. May, "Modeling MBE RHEEN signals using PCA and neural networks," *Compound Semiconductors 1997 IEEE Internation Symposium,* vol. IEEE Symposium, pp. 33-36, 1998.

[94] I. T. Jolliffe, Principal Component Analysis, New York City: Springer, 2002.

[95] M. Mumtaz, A. Mahmood, S. D. Khan, M. A. Zia, M. Ahmed and I. Ahmad, "Investigation of Dielectric Properties of Polymers and their Discrimination using Terahertz Time-Domain Spectroscopy with Principal Component Analysis," *Applied Spectroscopy,* vol. 71, no. 3, pp. 456-462, 2017.

[96] Q. Wang, X. Wu, L. Chen, Z. Yang and Z. Fang, "Plastic Classification with X-ray Absorption Spectroscopy Based on Back Propagation Neural Network," *Applied Spectroscopy,* vol. 71, no. 11, pp. 2538-2548, 2017.

[97] G. Smith and F. Campbell, "A Critique of Some Ridge Regression Methods," *Journal of the American Statistical Association,* vol. 75, pp. 74-81, 1980.

[98] M. B. Sporn and E. D. Harris, "Proliferative Diseases," *The American Journal of Medicine,* vol. 70, no. 6, pp. 1231-1236, 1981.

[99] N. A. Hafid and J. Christodoulou, "Phenylketonuria: a review of current and future treatments," *Translational Pediatrics,* vol. 4, no. 4, pp. 304-317, 2015.

[100] A. V. Zea-Rey, H. Cruz-Camino, D. L. Vazquez-Cantu, V. Gutierrez-Garcia, J. Santos-Guzman and C. Cantu-Reyna, "The Incidence of Transient Neonatal Tyrosinemia Within a Mexican Population," *Journal of Inborn Errors of Metabolism,* vol. 5, pp. 1-4, 2017.

[101] C. Carducci, M. Birarelli and N. I. Antonozzi, "Automated high-performance liquid chromotographic method for the determination of homocysteine in plasma samples," *Journal of Chromotography A. ,* vol. 846, pp. 93-100, 1999.

[102] J. L. Van Hove, C. Coughlin II, M. Swanson and J. B. Hennermann, "Nonketotic Hyperglycinemia," *Gene Reviews,* pp. 1-27, 2002.

[103] F. Poderbrad, M. Heil, S. Reichert, A. C. Sewell and H. Bohles, "4,5-Dimethyl-3-hydroxl-2[5H]-furanone(sotolone) - The odour of maple syrup disease," *J. Inher. Metab. Dis.,* vol. 22, pp. 107-114, 1999.

[104] E. Aliu, S. Kanungo and G. L. Arnold, "Amino Acid Disorders," *Annals of Translational Medicine,* vol. 6, no. 24, pp. 1-10, 2018.

[105] A. Carotenuto, A. M. D'Ursi, B. Mulinacci, I. Paolini, F. Lolli, A. M. Papini, E. Novellino and P. Rovero, "Conformation-Activity Relationship of Designed Glycopeptides as Synthetic Probes for the Detection of Autoantibodies, Biomarkers of Multiple Sclerosis," *J. Med. Chem.,* vol. 49, pp. 5072-5079, 2006.

[106] R. E. Taylor, Y. Chen, A. Beatty, D. C. Myles and Y. Zhou, "Conformation-Activity Relationships in Polyketide Natural Products: A New Perspective on the Rational Design of Epothilone Analogues," *J. American Chemical Society,* vol. 125, pp. 26-27, 2003.

[107] P. F. Filho, P. T. C. Freire, K. C. V. Lima, J. M. Filho, F. E. A. Melo and P. S. Pizani, "High Temperature Raman spectra of L-leucine crystals," *Braz. J. Physics,* vol. 38, no. 1, pp. 131-137, 2008.

[108] J. A. d. A. Lima, P. T. C. Freire, R. J. C. Lima, A. . Moreno, J. M. Filho and F. E. A. Melo, "Raman scattering of L-valine crystals," *Journal of Raman Spectroscopy,* vol. 36, no. 11, pp. 1076-1081, 2005.

[109] F. M. Almeida, P. T. C. Freire, R. J. C. Lima, C. M. R. Remédios, J. M. Filho and F. E. A. Melo, "Raman spectra of L-isoleucine crystals," *Journal of Raman Spectroscopy,* vol. 37, no. 11, pp. 1296-1301, 2006.

[110] O. Svensson, M. Josefson and F. W. Langkilde, "Reaction monitoring using Raman spectroscopy and chemometrics," *Chemometrics and Intelligent Laboratory Systems,* pp. 49-66, 1999.

[111] D. A. Bradbury, T. D. Simmons, K. J. Slater and S. P. Crouch, "Measurement of the ADP:ATP ratio in human leukaemic cell lines can be used as an indicator for cell viability, necrosis and apoptosis," *Journal of Immunological Methods,* vol. 240, pp. 79-92, 2000.

[112] T. T. Chen, C. S. Kuo, Y. C. Chou and N. T. Liang, "Surface-Enhanced Raman Scattering of Adenosine Triphosphate Molecules," *Journal of Surfaces and Colloids,* vol. 5, no. 4, pp. 887-891, 19889.

[113] P. Graveson, J. Branebjerg and O. S. Jensen, "Microfluidics - a review," *Journal of Micromechanics and Microengineering,* vol. 3, pp. 168-182, 1993.

[114] Y. Nishimura, K. Yano, M. Itoh and M. Ito, "Photolithography," in *Flat Panel Display Manufacturing*, Hoboken, NJ, John Wiley and Sons Ltd, 2018, pp. 287-310.

[115] P. Wilding, M. A. Shoffner and L. J. Kricka, "PCR in a silicon microstructure," *Clinical Chemistry,* vol. 40, no. 9, pp. 1815-1818, 1994.

[116] M. Schena, D. Shalon, R. W. Davis and P. O. Brown, "Quantitative Monitoring of Gene Expression Patterns with a Complementary DNA Microarray," *Science,* vol. 270, no. 5235, pp. 467-470, 1995.

[117] D. C. Duffy, J. C. McDonald, O. J. Schueller and G. M. Whitesides, "Rapid Prototyping of Microfluidic Systems in Poly(dimethysiloxane)," *Anal. Chem,* vol. 70, pp. 49-74-4984, 1998.

[118] G. M. Whitesides, E. Ostuni, S. Takayama, X. Jiang and D. E. Ingber, "Soft Lithography in Biology and Biochemistry," *Annual Review of Biomedical Engineering,* vol. 3, pp. 335-373, 2001.

[119] C. S. Effenhauser, G. J. Bruin and A. Paulus, "Integrated chip-based capillary electrophoresis," *Electrophoresis,* vol. 18, pp. 2203-2213, 1997.

[120] B. H. Weigl, J. Kriebel, K. J. Mayes, T. Bui and P. Yager, "Whole Blood Diagnostics in Standard Gravity and Microgravity by Use of Microfluidic Structures (T-Sensors)," *Microchimica Acta,* vol. 131, pp. 75-83, 1999.

[121] C. Chen, M. Mrksich, S. Huang, G. M. Whitesides and D. E. Ingber, "Micropatterned Surfaces for Control of Cell Shape, Position and Function," *Biotechnology Progress,* vol. 14, no. 3, pp. 356-363`, 1998.

[122] A. K. Au, W. Huynh, L. F. Horowitz and A. Folch, "3D-Printed Microfluidics," *Angew Chem Int Ed,* vol. 55, pp. 3862-3881, 2016.

[123] T. C. Chang, A. M. Mikheev, W. Huynh, R. J. Monnat, Jr, R. C. Rostomily and A. Folch, "Parallel microfluidics chemosensitivity testing on individual slice cultures," *Lab on a Chip,* vol. 14, pp. 4540-4551, 2014.

[124] N. S. G. K. Devaraju and M. A. Unger, "Pressure driven digital logic in PDMS based microfluidic devices fabricated by multilayer soft lithography," *Lab on a Chip,* vol. 12, pp. 4809-4815, 2012.

[125] A. J. Capel, S. Edmonson, S. D. R. Christie, R. D. Goodridge, R. J. Bibb and M. Thurstans, "Design and additive manufacture for flow chemistry," *Lab on a Chip,* vol. 13, pp. 4583-4590, 2013.

[126] [Online]. Available: http://www.stratasys.com/3d-printers/production-series/fortus-.

[127] D.-G. Ahn, J.-Y. Lee and D.-Y. Yang, "Rapid Prototyping and Reverse Engineering Application for Orthopedic Surgery Planning," *Journal of Mechanical Science and Technology,* vol. 20, no. 1, pp. 19-28, 2006.

[128] B. O. Erbano, A. C. Opolski, M. Olandoski, J. A. Foggaiatto, L. F. Kubrusly, U. A. Dietz, C. Zini, M. Marino, A. G. Leal and R. Ramina, "Rapid Prototyping of three-dimensional biomodels as an adjuvant in the surgical planning for intreacranial aneurysms," *Acta Cirúrgica Brasileira,* vol. 28, no. 11, pp. 756-761, 2013.

[129] Y. L. Cheng and S. J. Chen, Progress on Advanced Manufacture for Micro/Nano Technology, Pt 1&2, 2005.

[130] S. Begolo, D. Zhukov, D. A. Selck, L. Li and R. F. Ismagilov, "The pumping lid: investigating multip-material 3D printing for equipment-free, programmable generation of positive and negative pressures for microfluidic applications," *Lab on a Chip,* vol. 14, pp. 4616-4628, 2014.

[131] D. E. Atkinson and G. M. Walton, "Adenosine Triphosphate Conservation in Metabolic Regulation," *Journal of Biological Chemistry,* vol. 242, no. 13, pp. 3239-3241, 1967.

[132] M. Tamassia, F. Nuttinck, P. May-Panloup, P. Reynier, Y. Heyman, G. Charpigny, M. Stojkovic, S. Hiendleder, J. P. Renard and S. Chastant-Maillard, "In Vitro Embryo Production Efficiency in Cattle and Its Association with Oocyte Adenosine Triphosphate Content, Quantity of Mitochondrial DNA, and Mitochondrial DNA Haplogroup," *Biology of Reproduction,* vol. 71, pp. 697-704, 2004.

[133] F. Cole and P. R. Schimmel, "On the Rate Law and Mechanism of the Adenosine Triphospahte-Pyrophophate Isotope Exchange Reaction of AMino Acyl Transfer Ribonucleic Acid Synthetases," *Biochemistry,* vol. 9, no. 3, pp. 480-489, 1970.

[134] R. L. Post, C. Hegyvary and S. Kume, "Activation by Adenosine Triphosphate in the Phosphorylation Kinetics of Sodium and Potassium Ion Transport Adenosine Triphosphatase," *Journal of Biological Chemistry,* vol. 247, no. 20, pp. 6530-6540, 1972.

[135] M. Li, J. Zhang, S. Suri, L. J. Sooter, D. Ma and N. Wu, "Detection of Adenosine Triphosphate with an Aptamer Biosensor Based on Surface-Enhanced Raman Scattering," *Analytical Chemistry,* vol. 84, pp. 2837-2842, 2012.

[136] L. Xu, Q. Xu, X. Guo, Y. Ying, Y. Wu, Y. Wen and H. Yang, "Facile synthesis of Au/Al2O3 nanocomposites for improving the detection sensitivity of adenosine triphosphate".

[137] X.-H. Pham, E. Hahm, T. H. Kim, H.-M. Kim, S. H. Lee, Y.-S. Lee, D. H. Jeong and B.-H. Jun, "Adenosine Triphosphate-Encapsulated Liposomes with Plasmonic Nanoparticles for Surface Enhanced Raman Scattering-Based Immunoassays," *Sensors,* vol. 17, no. 1480, pp. 1-11, 2017.